THE UNIVERSITY OF CHICAGO

RHOA MEDIATES ADAPTIVE JUNCTION MECHANICS AND CONTRACTILE ASYMMETRY

A DISSERTATION SUBMITTED TO
THE FACULTY OF THE DIVISION OF THE BIOLOGICAL SCIENCES
AND THE PRITZKER SCHOOL OF MEDICINE
IN CANDIDACY FOR THE DEGREE OF
DOCTOR OF PHILOSOPHY

COMMITTEE ON DEVELOPMENT, REGENERATION, AND STEM CELL BIOLOGY

BY
KATE ELIZABETH CAVANAUGH

CHICAGO, ILLINOIS
MARCH 2021

TABLE OF CONTENTS

LIST OF FIGURES

LIST OF TABLES

LIST OF ABBREVIATIONS

ABP	Actin binding protein
AJ	Adherens junctions
AP	Anterior-Posterior
Clc	Clathrin light chain
CME	Clathrin-mediated endocytosis
CE	Convergent Extension
CIV	Cortical immovable vesicle
DV	Dorsal-Ventral
EC	Ectodomain
GAP	GTPase activating protein
GBE	Germband Extension
GDI	Guanine nucleotide dissociation inhibitors
GEF	Guanine nucleotide exchange factor
GPCR	G-Protein Coupled Receptor
LRR	Leucine Rich Repeat
MPA	Micropipette Aspiration
NMII	Non-muscle Myosin II
ROCK	Rho-associated protein kinase
TULIP	Tunable light-interacting protein tags
ZA	Zonula adherens

ACKNOWLEDGMENTS

My success as a scientist was made possible by the inspirational people with whom I surrounded myself. These mentors, colleagues, friends, and family members guided and supported me in critical periods of my life. I am eternally grateful for them. I am who I am because of these people.

This project would not have been possible without Margaret Gardel's unwavering support throughout my PhD. She believed in me even as a young graduate student and entrusted me with an ambitious project to establish this optogenetic system. Through every frustration and pitfall, she was there to support and encourage me not to give up. She gave me incredible freedom with this project and working with her has been an inspiration. I am the scientist I am today because of Margaret's guidance and mentorship.

My incredible experience in the Gardel lab was also shaped by fantastic mentors in each of the Gardel lab members. I want to thank every one in the lab for their help at every step of my project, from listening to frustrations and successes to troubleshooting and optimizing. I want to give a special thank you to Bob and Yvonne, who were both crucial in helping me get up and running in the beginning of my PhD. I also want to thank Tracy for helping me with much of the data analysis.

I am deeply grateful to my thesis committee, Vicky Prince, Ed Munro, and Sally Horne-Badovinac. They have provided me with invaluable guidance and technical support with every committee meeting. I enjoyed every single one of our meetings together and valued these incredible scientists' input at every stage of my career at UChicago. Seeing their enthusiasm for science permeated into my science, as well. So I am thankful for the inspiration. I also want to give a special thanks to Ed, who was willing to meet with me consistently to excitedly go over new data and its interpretations.

I would like to thank everyone in the DRSB, faculty and students alike, for creating a welcoming and intellectually challenging environment that made me thrive. The DRSB journal clubs were days I looked forward to, and I will miss the environment dearly. UChicago

proved to be a profound educational experience for which I am extremely grateful. Thanks goes to the administrators for all of the behind-the-scenes work to make my graduate school career run smoothly. I additionally thank the MCB training grant that supported me and provided me a platform to present my work throughout the years.

Specifically, I would like to thank the friends at UChicago I made along the way who made life full and bright. To the Affiliates - many thanks for all the memories made. I am so lucky to have had such amazing friends and experiences. I will never forget the times we had and will forever cherish these memories. I hope we can all look back on these days fondly when we are all leaders in our fields.

I want to thank my incredible family for supporting me through these years. My mother and my grandmother are strong women who inspired me to follow my dream of completing graduate school. To them, this is the dream they had when they immigrated to America - that their children could succeed and thrive. I consistently strive to make them proud. My path to my PhD was winding, yet they supported me through every decision and step. They were also there to cheer me on at every stage of my career in this PhD.

I am lucky to have found love in graduate school. Thank you also to Jimmy, my husband, for eternal motivation and support throughout this process. He motivates me to be better, to be curious, in science and in life. I could not have finished this PhD without his humor, patience, and love.

ABSTRACT

Epithelia undergo morphogenetic remodeling events to generate the embryo's final form. Morphogenetic episodes may arise from relatively small, discrete changes in cellular behaviors, namely cell migration, constriction, intercalation, division, and extrusion events. These highly conserved behaviors arise from the spatial and temporal integration of cytoskeletal-based contractile forces at adhesion complexes, the tuning of which can either maintain tissue homeostasis or allow for dynamical tissue processes. This mechanochemical signaling therefore underlies mechanical force transmission and transduction necessary for proper cell and tissue mechanics. Failure in the strict regulation of this mechanochemical circuitry can result in aberrant cellular and tissue behaviors, producing various birth defects and cancers. As embryogenesis is highly complex in nature, reductionist approaches have become increasingly appealing and tractable to shed light on conserved morphogenetic mechanisms. The work described here takes a bottom-up approach to elucidate the complex behaviors described in development. Specifically, to examine cell shape maintenance and cell-cell junction length regulation via the cytoskeletal regulator and small GTPase, RhoA. RhoA is highly dynamic during morphogenesis and exhibits complex behaviors that are thought to generate asymmetric, ratcheted junction length changes. However, little is known about RhoA regulation in determining junction length and contractile phenotypes. Here, I use optogenetic probes and various pharmacological compounds to exogenously regulate RhoA at cell-cell junctions, elucidating what is necessary and sufficient to drive cell shape changes in model epithelia. I couple this work with a collaboration in mathematical modeling to further elucidate the mechanisms by which RhoA confers junction length. Together, we find that junction deformation contains a strain threshold to dictate junction length and that the duration, strength, and temporal sequence of RhoA-mediated contractility confers length. Junction stabilization at shorter lengths requires endocytosis to remove junctional and membrane material for progressive shortening. I additionally find that, during contraction, junction shortening occurs asymmetrically with one motile vertex and one less-motile vertex.

This vertex motion is dependent on the feedback between RhoA and E-Cadherin, which produces an opposing frictional force to limit junctional contractions. The work described here begins to uncover the biophysical and cellular basis of RhoA regulation in junction mechanics, providing exciting new hypotheses to test how RhoA-mediated mechanical forces drive junction length changes.

CHAPTER 1

INTRODUCTION

1.1 Preface

Morphogenesis is defined as the suite of underlying biological processes orchestrating the dynamic formation of macroscopic shapes in biological matter. Macroscopic tissue movements ultimately arise from the mesoscopic properties of cell-cell junctions, coordinated in both space and time [1]. Such developmental mechanisms often occur simultaneously or in sequence, involving the interplay of geometric and mechanical forces, as well as genetic and molecular cues. The result is a cascade of interrelated events spanning the molecular, cellular, and tissue scales, all of which combine to ultimately generate organismal shape. Accordingly, a holistic view of embryogenesis necessitates the unification of both junction mechanics and molecular genetics. Developmental biology is therefore an increasingly interdisciplinary science, applying both biology and physics to investigate the contribution of mechanical forces and their underlying mechanochemical regulation at cell-cell interfaces.

Modern views on cell mechanics were shaped, in part, by pioneering work from D'arcy Wentworth Thompson [2]. In his seminal book, On Growth and Form, he postulated as to the physical and mathematical rules governing the generation of biological size and shape [3]. His work introduced a profound idea of a diagram of forces, in which biological form can be viewed and studied as an impression of the generative forces imposed and maintained upon the organism. He argued further that, much like soap bubbles, the distribution of interfacial tensions at cell vertices within multicellular tissues determines constituent cell shapes. This concept has been instrumental for developing modern mathematical models, such as the Vertex Model, which postulates that cellular geometry arises from the mechanical forces acting at cell-cell junctions [4]. As such, Thompson has influenced the application of mathematical concepts and formulas to how cells shape themselves.

The first part of the twentieth century, with D'arcy Thompson, saw the birth of contem-

porary approaches to morphogenesis, in that mathematical theory and physical laws were used to describe biological form. The second half of the century was instead dominated by the advent of genetics, shifting the research focus away from the physical and towards the molecular basis of morphogenesis [5]. However, recent technological advancements have revived the ideologies described in On Growth and Form, guiding modern developmental biologists to examine once again the physical forces driving morphogenesis [2]. Now, much of developmental biology hinges upon how mechanics determines tissue form, fate, and function [1]. Cell mechanics is therefore increasingly becoming merged with molecular biology, as we begin to understand the feedback between mechanics and its influence on gene and protein behavior in regulating cell shape.

This introductory chapter provides a short summary of the role of cell mechanics in morphogenesis, drawing much inspiration from Thompson's On Growth and Form. We first describe the molecular basis of force production and transduction, followed by a description in how forces mediate morphogenetic processes in the embryo. We then describe the physical basis of cell shape using the Vertex Model and describe recent technological advances to test Vertex model predictions. Part of this Introduction, specifically pieces in sections 1.4 on junction viscoelasticity, is published in Current Opinions in Genetics and Development.

1.2 Molecular basis of force production and transduction

1.2.1 Molecular origins of contractile forces

The Rho family of GTPases are critical regulators of diverse cellular functions, including cell dynamics, cell-cycle progression, membrane trafficking, gene transcription, and apoptosis [6]. RhoA GTPase largely coordinates cellular shape by regulating both intracellular cytoskeletal dynamics and cortical contractility [7]. Post-translationally modified RhoA associates into the plasma membrane, where it behaves as a molecular switch [8]. Once activated, GTP-bound Rho binds to its downstream effectors Formin and Rho Kinase (ROCK) to trigger local actin

polymerization and myosin contractility, respectively [9]. Its GDP-GTP cycle regulation comes in three main forms. GDP dissociation occurs slowly, so the loading of GTP and subsequent Rho activation is accelerated by guanine nucleotide exchange factors (GEFs). GTP hydrolysis by GTPase activating proteins (GAPs) converts RhoA back to its inactive GDP-bound conformation (Fig. 1.1). RhoA activity can also be sequestered by guanine nucleotide-dissociation inhibitors (GDIs) that inhibit its membrane localization. Cycling between Rho inactive and active states creates highly dynamic contractile arrays that assemble rapidly in response to intracellular biochemical signals and/or physical cues from neighboring cells [10].

One type of mechanical support in eukaryotic cells comes from filamentous actin (F-actin) structures and their associated actin binding proteins (ABPs) [11]. Actin filaments are linear polymers of globular actin (G-actin) subunits that form a long-pitched double helix [12]. ABPs can organize F-actin networks into a wide range of higher order cytoskeletal structures like linear bundles, two-dimensional branched networks, and three-dimensional arrays that contribute to a broad range of cellular processes. Perhaps the best characterized ABPs that regulate actin architectures are Arp2/3 and formins. The Arp2/3 complex produces branched actin networks while formins nucleate long straight filaments [13]. Rapid turnover of these actin architectures, coordinated by severing proteins, creates a dynamic cytoskeleton that, while structurally rigid, is incredibly plastic in nature [11]. These characteristics are thought to give the cell elastic- and viscous-like properties to enable cells to resist shape deformations during homeostasis while allowing them to dynamically change their cytoskeleton during morphogenesis [14].

Actin filaments in contractile assemblies are interdigitated with bipolar filaments of non-muscle myosin II (NMII) [15]. NMII is composed of a head, neck, and tail region. The head region binds F-actin and the alpha helical coiled-coil tail allows interactions with other myosin subunits [16]. The neck region houses two light chains, the essential and the regulatory light chain, that are regulatory sites for its inherent ATPase activity [17]. Rho-activated ROCK

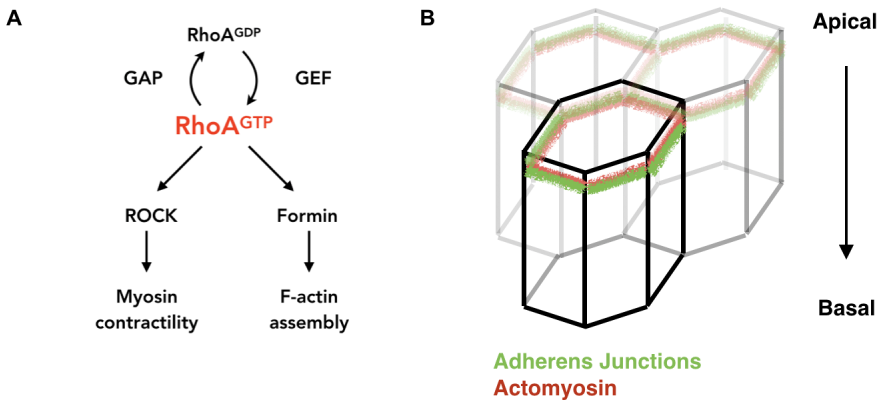

Figure 1.1: The Rho pathway and epithelia. A) Schematic showing the RhoA signaling pathway B) Schematic showing the structure of an epithelium. Adherens junctions are in green and Actomyosin is in red.

phosphorylates the myosin regulatory light chain to increase NMII ATPase activity. In this way, NMII converts chemical energy in the form of ATP to mechanical energy to generate a mechanochemical cycle of binding, hydrolysis, and release of ATP [17]. This cycle is intimately linked to actin filament binding, conformational change, and force production. Contractility therefore arises when several bundled and active myosins, which are asynchronously active on actin filaments, induce the net shortening of actin fibers [18].

1.2.2 Contractile forces at adhesive structures in epithelia

An epithelium is composed of a single uniform layer of cells adhered to one another at the apical zonula adherens (ZA) through adherens junctions (AJs), tight junctions, and desmosome-based adhesions (Fig. 1.1). For simplicity, we focus here on cytoskeletal coupling to AJ components, since it is a main determinant in cell shape regulation [7]. AJs are comprised, in part, of E-cadherin-based adhesions that are transmembrane proteins housing five distinct, sequential ectodomains (EC1-EC5) (Fig.1.2)[19]. Intercellular E-cadherins (E-Cad) bind homotypically in *trans* through EC1 and then cluster in *cis* through EC2 binding [20]. Linker proteins such as alpha, beta, and p120 catenins tether cadherin-based adhesions at their cytoplasmic face to a circumferential junctional belt of contractile actomyosin filaments

(Fig. 1.2) [20]. This structure is known as the cadherin-catenin complex. Specifically, beta-catenin binds E-cadherin at its distal C-terminus. Alpha-catenin binds both beta-catenin and actin structures, thereby coupling adhesion with the cytoskeleton. P120-catenin binds to the juxta-membrane domain in the proximal C-terminus of E-cadherin to regulate its turnover. Together these proteins provide essential functions in integrating mechanosensation and mechanoresponse for tissue homeostasis and morphogenesis [21].

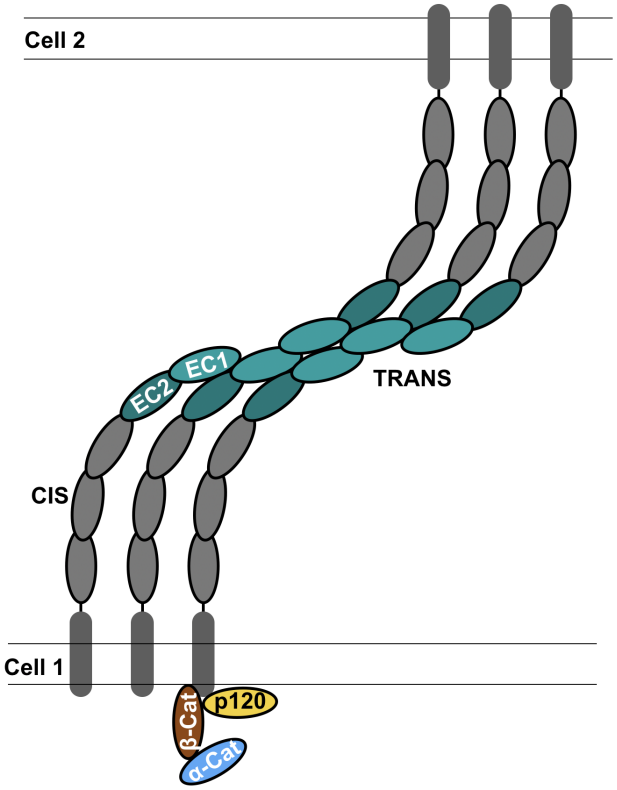

Figure 1.2: The cadherin-catenin complex. Schematic showing the structure of E-cadherin and associated catenin complexes attached at the cytoplasmic face.

Increased mechanical loading at cell-cell junctions causes force-induced alterations in the conformation of cadherin linker proteins, enabling transduction and conversion of mechanical stimuli into biochemically active signals [21]. This feature of cadherin biology is known as "outside-in" signaling or mechanotransduction. Adhesive engagement of the cadherin-catenin complex elicits the action of many regulatory pathways, perhaps the most extensively studied being that of alpha-catenin-mediated signaling. Tension sensitive alpha catenin

has many diverse binding partners such as p115RhoGEF and Ect2, both of which promote RhoA signaling [22, 23]. These mechanical signals, in turn, act at adhesive complexes to tune junction tension and junction length, giving rise to "inside-out" signaling [21]. The "inside-out" response includes action by ABPs Arp2/3 and formin; both contribute to the generation of the perijunctional actomyosin belt and resulting junctional tension [24, 25].

Individual cell shape and overall tissue topology depend on the balance of contractile and adhesive forces at the zonula adherens. While adhesion maximizes cell-cell contacts, contractility works to reduce cell contacts and junction perimeter lengths. At homeostasis, the cell is contracting equally around its periphery to yield a hexagonally packed epithelium. This state represents an energy minimum where all cells have a homogenous distribution of adhesion and contractility at their junctions. Sufficient asymmetry to this system (i.e. Rho-mediated force production) is believed to drive major cell shape and junction length changes associated with morphogenesis. Understanding the mechanism by which cells tune their adhesive and contractile properties will therefore greatly enhance our understanding of tissue mechanics and morphogenesis.

1.2.3 The junctional RhoA zone and its regulation at cell-cell junctions

Tissue homeostasis and proper cell-cell adhesion is dependent on the local modulation of a junctional RhoA zone [22, 26–28]. At homeostasis, the junctional RhoA zone is thought to be sculpted by the spatiotemporal coordination of patterned Rho activation, transport, and termination [29]. The net activity of GEFs, GAPs, and GDIs may therefore tune junctional contractility to confer cell shape. For instance, the precise localization of both GEF Ect2 and GAP p190B-RhoGAP regulates RhoA activity; depletion of these Rho regulators showed aberrant junctional morphologies [22]. AJ complexes were similarly destabilized upon depletion of P190ARhoGAP [30]. Together these data suggest that proper RhoA levels, tuned by its GDP-GTP cycle, influence junction morphology. While much work has been done in the way of elucidating these molecular components in driving a stable Rho zone, the

mechanisms by which they act are incompletely understood.

The current model for RhoA regulation at the AJ assumes that the net activity of GEF/GAP/GDI shapes the Rho zone and subsequent junction morphologies [29]. However, an additional mechanism exists to tune the kinetics of RhoA at the ZA. In mature epithelia, the perijunctional actomyosin belt maintaining a mature AJ is scaffolded by Anillin, knockdown of which shows severe disruptions to AJs and aberrant junctional RhoA "flares" [31, 32]. These data suggest that Anillin may spatially confine RhoA activity for a proper RhoA zone. Indeed, Anillin reduces junctional RhoA dissociation and increases cortical dwell time by promoting its entry into a stable complex with the lipid phosphoatidylinositol 4,5-biphosphate (PIP_2) [33]. In this way, Anillin promotes RhoA localization by stabilizing its membrane binding and promoting cyclic engagement with PIP_2 for signal transduction. Together these data implicate the scaffolding protein Anillin as a major regulator of junctional RhoA activity, independent of the canonical GEF/GAP/GDI regulation.

The above mechanism implicates a coincidence detection scheme, where upstream regulators are spatiotemporally coordinated for robust Rho signaling. This is in line with work documenting various scaffolding proteins in the regulation of RhoA signaling at the AJ. For instance, both alpha-catenin and p120-catenin can bind to RhoA, suggesting multiple intramolecular interactions contribute to the RhoA zone [23]. Alpha-catenin was also shown to stabilize RhoGEF Ect2 at the ZA to promote RhoA signaling [22]. Additionally, the scaffolding protein Cingulin binds to p114RhoGEF, ROCK, and NMII to confine RhoA signaling at the apical junctions [34]. GEFs, themselves, may even act as scaffolds. It was reported that GEFs in the human Dbl homology family contain putative C-terminal PDZ binding motifs [35]. That PDZ binding motifs are present in the GEF structure suggests that they can interact with cell-cell junctions, which are rich in PDZ domain-containing proteins [7]. Multiple intramolecular interactions and higher-order GEF protein complexes may therefore be necessary to provide for a robust RhoA zone at the ZA. However, our understanding of how RhoA regulation mediatess junction length is still unclear.

1.3 Cellular shape changes in development

1.3.1 Tissue extension via cell-cell junction length changes

A major outstanding question in development is how cells coordinate their shapes to create stereotypical morphogenetic movements. One such canonical morphogenetic movement in embryogenesis is that of tissue extension. Often termed convergent extension (CE), this movement involves the intercalation and neighbor exchange of distinct cell populations [36]. The result is a narrowing of the tissue width and elongation of the tissue in the long axis. CE is responsible for numerous developmental events seen across taxa, including Xenopus Gastrulation, Drosophila Germband Extension, and Vertebrate Neurulation [37–39]. A wide range of congenital birth defects are associated with CE failure, including neural tube, kidney tubule, and cochlear malformations [40–42].

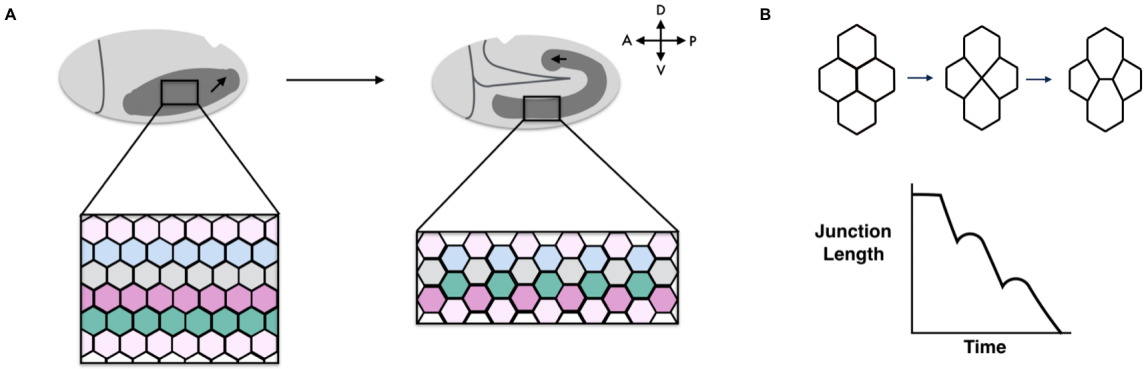

Figure 1.3: Germband extension and the T1 transition. A) Schematic showing the Drosophila embryo undergoing Germband Extension (top) and cell intercalation (bottom) B) Schematic showing the T1 transition and associated junction lengths over time

Drosophila Germband Extension (GBE) is perhaps the most extensively studied CE event (Fig. 1.4A) [43]. Spatial cues, at both the tissue and cellular scale, break symmetry to guide intercalations in distinct Germband compartments [44]. Morphogen gradients across the tissue induce transcriptional cascades that culminate in positional identities [43]. Positional identities influence mechanical behaviors, as blocks of cells generate parasegment boundaries

that block cell mixing via long planar polarized NMII cables along DV interfaces [44, 45]. Constituent cells within these parasegment boundaries undergo stereotypical intercalations as a result of smaller NMII cables, whose collective contractility drives a near two-fold elongation of the embryo [46–48]. Some of these topological changes are characterized by the so-called "T1 transition" that can be divided into three consecutive stages of 1) dorsal-ventral (DV, i.e. vertical) junction contraction, 2) four-cell vertex formation, and 3) nascent junction elongation in the anterior-posterior (AP) axis for neighbor exchange (Fig. 1.4B) [49].

Signaling downstream of G-Protein Coupled Receptors (GPCRs) promotes the localized accumulation of RhoGEFs, Rho GTPase, and its effectors [51, 57, 58]. Spatial patterning of these components establishes two pools of Rho-mediated actomyosin contractility at the medioapical cortex and junctional adhesion belt; these zones will be referred to as the medial and junctional zones (Fig. 1.4) [58–60]. Here, G proteins $G\alpha_{12/13}$ and Gβ13F/G_γ1 regulate GEFs RhoGEF2 and Dp114RhoGEF, respectively. These two RhoGEFs serve as independent, yet complementary, Rho regulatory modules [58]. Specifically, Dp114RhoGEF was discovered as a novel junctional Rho activator in tissue extension that coordinates with medial/junctional RhoGEF2. Interestingly, neither Gβ13F/G_γ1 nor Dp114RhoGEF are planar polarized at shrinking vertical junctions [58]. This suggests another mechanism exists to confer spatial Rho asymmetry at DV interfaces, possibly through polarized GEF-activation at vertical junctions or GAP-inactivation of Rho at the horizontal junctions. It is also speculated that

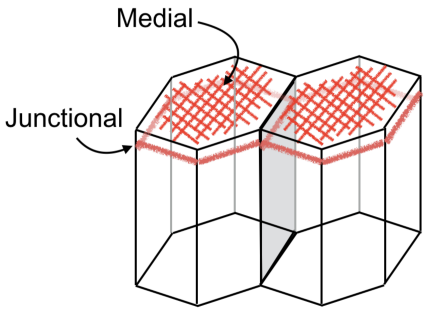

Figure 1.4: The medial and junctional Rho zones. Schematic showing the two zones of Rho activity at the medioapical and junctional areas of epithelial cells.

Rho dwell time could be increased by Anillin scaffolding, although this hypothesis has not been tested.

The medial and junctional Rho zones have complementary functions during morphogenesis. The junctional zone is thought to be responsible for changes in cell junction lengths for vertex formation while the medial zone changes the apical cell area for vertex resolution [61–63]. Medial Rho and NMII also oscillate and flow toward DV junctional zones, and this molecular oscillation is coincident with junction shortening [59, 64]. Coordinated Rho pulses therefore drive multiple rounds of actomyosin network formation, contraction, and dissipation necessary for these junction length changes. The result of these oscillatory behaviors is an asymmetric, cyclical junctional ratchet that is characterized by incrementally stabilized junction contractions, followed by brief junction expansion before the next round of contractions (Figure 1.3B) [65, 66]. The function of this junctional ratchet, and specifically of pulsatile RhoA, remains unknown.

Myosin is preferentially enriched at shrinking DV interfaces and is required for cell intercalations [46]. Fluorescence recovery after photobleaching experiments have shown that NMII is recruited to and stabilized at regions of high tension, suggesting a positive feedback loop maintains stable junction contractions within the ratchet [67]. Additionally, NMII phosphorylation states, controlled by by ROCK, ensure stable cell shape changes and progressive interface shortening [68, 69]. These data have led to the prevailing model that spatiotemporal, incremental increases in mechanical tension mediate stable junction deformations [67]. However, this mechanism has been difficult to dissect experimentally.

T1 transitions occur in regions with high variance in tension between neighboring junctions [70]. It is thought that these local, junctional force imbalances ensure progressive interface contraction into a four-cell vertex [62, 71]. Force imbalances arise from the asymmetries in the contractile and adhesive apparatus, generating low levels of E-cadherin and high levels of actomyosin at vertical junctions for efficient deformations (Fig. 1.5, top). Decoupling these two modules can be difficult, as E-cadherin asymmetries orient medioapical actomyosin flows

and exhibit oscillatory patterns synchronized to pulsatile actomyosin at shrinking vertical junctions [72]. Nonetheless, asymmetries can be generated by the polarized stabilization and endocytic turnover of adhesion complexes. Specifically, this asymmetry arises from the coordinated action of Abelson tyrosine kinase-mediated Beta-catenin phosphorylation, ROCK-dependent exclusion of junction-stabilizing proteins Bazooka/Par-3, and asymmetric Clathrin-mediated endocytosis [73–75]. Genetic or pharmacological inhibition of any of these facets reduces E-cadherin asymmetries, destabilizing junctional deformations and subsequent tissue elongation (Fig. 1.5, bottom). However, further work is required to dissect the mechanisms underlying E-cadherin stabilization and turnover.

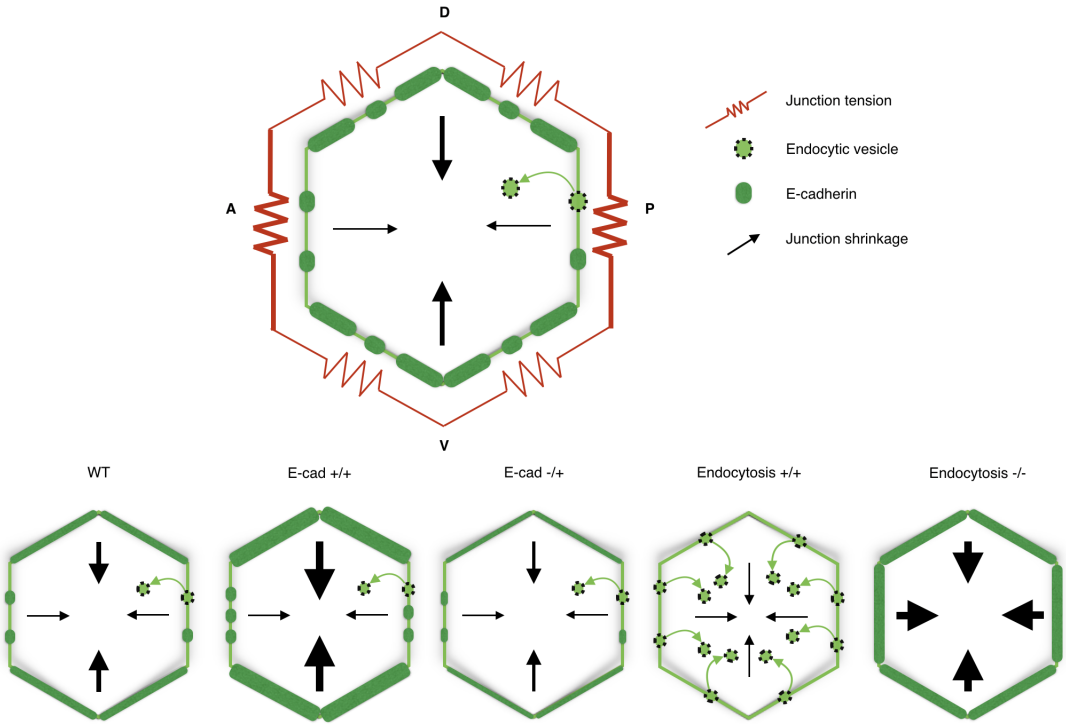

Figure 1.5: Junction asymmetries. (top) A schematic showing polarized junctional tension (actomyosin) and adhesion. (bottom) A schematic showing the phenotypes of E-cadherin distributions and endoctyosis patterns of different mutants. Figure adapted from [72]

The contribution of localized force production along a single junction is still unclear. The canonical view of the zonula adherens illustrates a circumferential actomyosin belt attached to a corresponding ring of E-cadherin adhesions, the coupling of which drives cell shape changes

[71, 76]. While this assumes functional symmetry between all portions of the junctions, recent work has suggested that bicellular borders act as independent contractile units [77]. These data suggest that bicellular interfaces and tricellular vertices act as two distinct and almost opposing functional units [77, 78]. Force production along these junctions is not uniform, as bicellular interfaces and tricellular contacts experience different medioapical actomyosin flows [64, 78]. Here, medioapical flows to bicellular junctions is correlated with their deformations [59, 64]. Elevated contractility at vertices stimulates E-cadherin recruitment, thereby restricting vertex deformations to stabilize the junctional ratchet [78]. Together these data suggest that vertices and bicellular interfaces, and their associated actomyosin flows, contribute differentially to junction deformations and ratchet stabilization. However, further work isolating actomyosin flows to these contractile units will only aid our understanding of junctional mechanics.

1.3.2 Endocytosis and cell shape changes

While the role of force generating events in driving T1 topological transitions is well established, little is known about the role of membrane trafficking in guiding such morphogenetic events. Membrane trafficking in the form of endocytosis is the process by which vesicular packets of material from the plasma membrane are internalized. While endocytosis is necessary for a variety of cellular processes, only recently has it been explored in cell shape stabilization [79]. Endocytic turnover of E-cadherin has been shown to stabilize junctional remodeling and ratcheting during neighbor exchange [66, 75]. Inhibition of the endocytic machinery through genetic means (Shibire/Dynamin alleles) or pharmacological inhibitors (chlorpromazine, PitStop-2) prevents this vertex formation and resolution so that the junctions remain at their original lengths [75, 78, 80]

GBE shows direct endocytic uptake of dextran through specialized, asymmetrically localized long endocytic tubules termed cortical immovable vesicle (CIV) structures. CIV formation and scission is facilitated by ABPs, Arp2/3 and formin Dia, at distinct points in

the endocytic process. Dia functions early in the endocytic process to cluster E-cadherin, concentrating E-cadherin clusters for vesicle initiation and their subsequent internalization. Plasma membrane localization of the Arp2/3 complex activator, Scar, enhances dextran uptake and functions at vesicle scission. This led to the model whereby the Drosophila RhoGEF2 activates its downstream effectors to locally cluster E-cadherin molecules for eventual internalization.

More recent work has highlighted the essential function of the upstream endocytic Rab regulators in mediating progressive interface contraction within GBE. This large family of small GTPases controls membrane identity and vesicle transport within and between cell organelles [81]. Of 31 Drosophila Rab proteins, only Rab35 was identified that exhibited planar polarized, oscillatory behaviors coincident with pulsatile actomyosin in the Germband [66]. These behaviors lend to Rab35's function to stabilize junctional ratchets upon their contractile phases, absence of which show contractile steps that are rapidly reversed. Interestingly, inhibition of CME components or actomyosin gave rise to long, extended Rab35 tubules that failed to terminate. Such a result demonstrates how Rab35 acts as a common membrane shaping mechanism to ensure unidirectional junctional movement within T1 transitions. Altogether these data show how membrane removal and junctional remodeling stabilize cell shapes upon ratcheted actomyosin network force generation.

While there is an intimate relationship between RhoA-mediated contractility, junction tension, and the endocytic machinery, the nature of the feedback has been controversial. Within GBE, Rho and its downstream effectors, NMII and Dia, colocalize with the junctional CME components, AP2 and Clc [75]. The Rho and CME pathway seem to have an intricate feedback system, as constitutively active Dia was shown to increase junctional Clc recruitment while NMII inhibition decreased junctional Clc levels [75]. These data point to the idea that adherens junction remodeling is tension sensitive [82–84]. Indeed, E-cadherin has been shown to be mechanosensitive in its turnover, with *increased* junctional tension driving increased turnover rates [83–85]. Here, mechanical stress releases p120-catenin from the

cadherin-catenin complex, allowing for heightened E-cadherin turnover [83]. Conflicting data documents how *decreased* junction tension dictates the rate of junction removal, with slackened junctions being sites of increased junctional remodeling [86]. What can reconcile these two competing hypotheses is a mechanism by which junction compression via RhoA-mediated contraction leads to local regions of reduced junctional tension whose sites act as endocytic hubs. However, this mechanism has not been tested and the feedback mechanism between RhoA and the endocytic machinery still remains unclear.

1.4 Cell-cell junction mechanics

1.4.1 Canonical Vertex Models of epithelial tissues

Computational modeling offers a complementary tool to many experimental techniques in the study of mechanics. Mathematical modeling can be used to develop abstract representations of biological systems from which valuable information can be gleaned about the underlying assumptions and resulting emergent behavior. These models help to clarify experimental data and observations by building mechanistic explanations founded on underlying physical principles. Quantitative physical descriptions of tissue morphodynamics through Vertex Models have given much interpretation to the generation of mechanical forces that drive embryogenesis. The Vertex model originates from the study of inorganic structures such as soap bubbles or foams, where surface tension and pressure drive packing configurations and their dynamics [87, 88]. The striking resemblance between foams and the 2D surface of epithelia led to the model's adaptation to study epithelial packing and morphogenesis [4]. These Vertex models have successfully simulated cell shapes in Drosophila, Xenopus, Hydra, mouse, zebrafish, Arabidopsis, and more recently in cultured tissues [89–95].

In canonical vertex models of epithelial tissues, each cell is defined by a polygon with cell-cell junctions represented by straight edges and vertices connecting the tricellular junctions as nodes (Fig. 1.6A, B). Each cell harbors the following: an edge tension arising from cortical

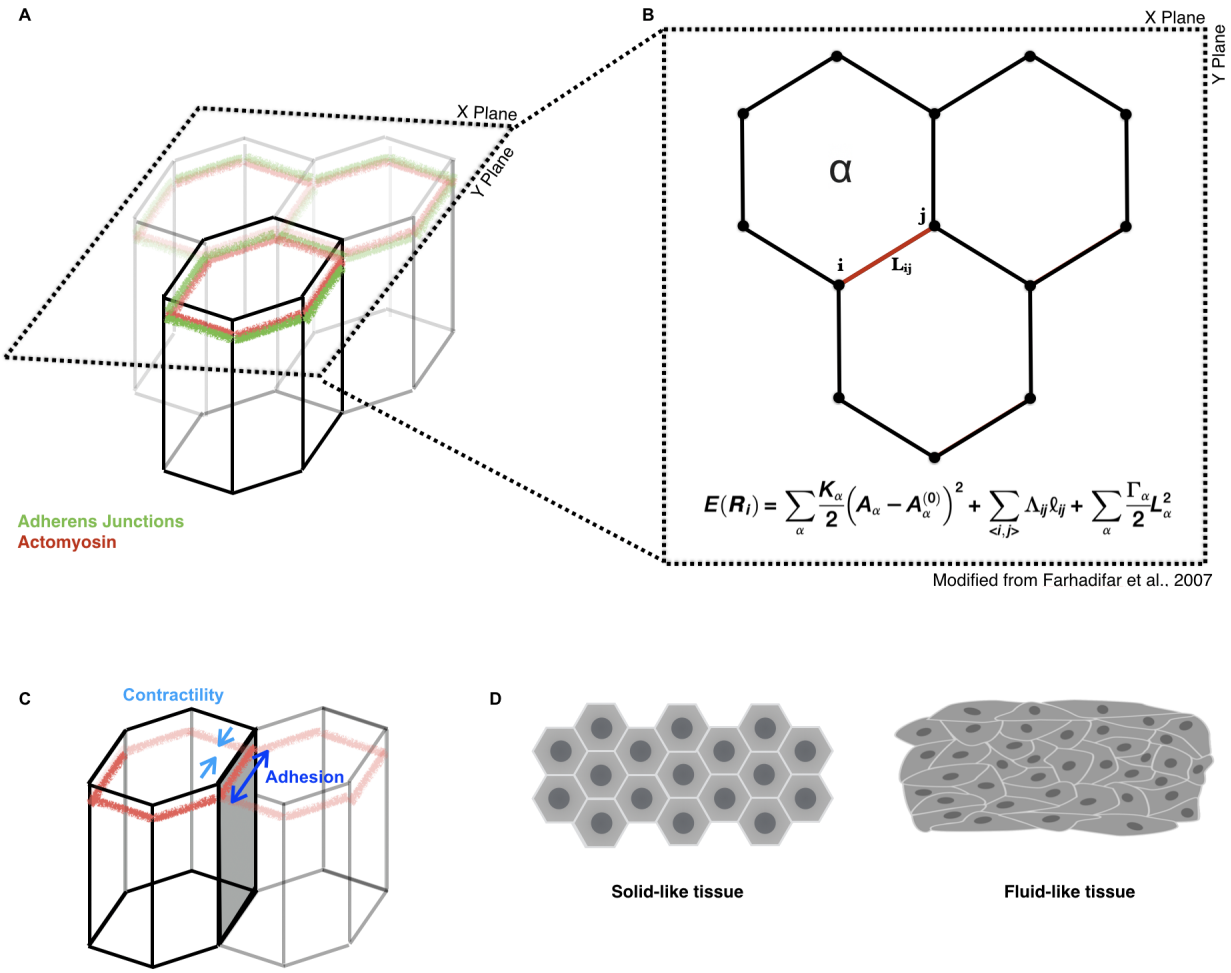

Figure 1.6: The Vertex Model. A) Schematic of a 3D layer of cells with adherens junctions in green and actomyosin in red. B) Schematic of a 2D representation of epithelia with the force balance as a local energy minima equation below. The first term details the area elasticity with elastic coefficient $\kappa\alpha$. α is the area of cell α and A_α^0 is the preferred area. The preferred area is determined by cell height and cell volume. Line tensions L_{ij} denotes the length of the cell-cell interface linking vertices i and j and the sum over $<ij>$ is over all bonds. The third term details the contractility at the cell perimeter L_α by a coefficient Γ_α C) A diagram showing the forces that contribute to epithelial cell shape. Contractility is in light blue and Adhesion is in dark blue. D) Schematic representation of a solid- and fluid-like tissue.

actomyosin coupled to adhesive structures along a cell-cell interface, a bulk tension that arises from the medial contractile actomyosin meshwork, and an area elasticity that counteracts changes in cell apices (Fig. 1.6A,B) [96]. The balance and opposition of tension and elasticity gives rise to varying geometries, specified by the variables describing both the edge and bulk tension, and also the area elastic modulus (Fig. 1.6B,C) [90]. Vertices can then move in response to forces due to growth, interfacial tension, and pressure within each cell [4]. The positions of these vertices, the connections between them, and the resulting forces between vertices provide complete information about the shape and mechanics of the epithelial sheet [97].

The vertex model can give rise to tissue properties with elastic or fluid-like behaviors depending on the relative magnitudes of interfacial tension (Λ) and contractility ([90, 98]. Increasing Λ leads to a solid-like tissue, charactereized by non-zero shear modulus, isotropic cell shapes, and persistent cell motion; tissues in a fluid-like state have vanishing shear modulus, anisotropic cell shapes, and randomized cell motions with frequent neighbor exchanges (Fig. 1.6D) [98, 99]. In solid-state tissues, vertex models predict a purely elastic response of cell-cell junctions upon stress, also known as applied tension, Λ_a. That is, once stress is applied the junction will deform and once applied stress is removed the junction will recoil back to its original length. For a fluid tissue, the junctions will exhibit no recoil and the tissue will remain permanently deformed (Fig. 1.7) [94]. While standard implementations of the vertex model are widely used, little has been done in the way of experimentally testing these junctional responses to mechanical force.

1.4.2 Passive modes of junction viscoelasticity

Direct measurement of junction rheology will allow for the mechanistic dissection of mechanical deformations and their underlying molecular contributions [100]. However, the physical basis of junction viscoelasticity has only recently become experimentally tractable in the biological sphere [101]. An ideal method to test cellular rheology must provide sufficient

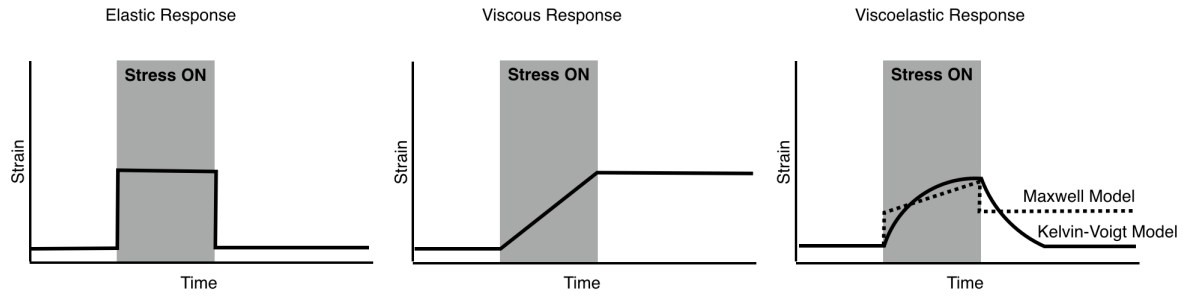

Figure 1.7: Viscoelastic behaviors of materials. Left) In elastic materials, strain is proportional to stress. During Λ_a, the material maintains a constant strain. After Λ_a is removed, the material returns to its original shape. Middle) In viscous materials, strain rate is proportional to stress. The material remains at rest after stress is removed and remains permanently deformed. Right) Viscoelastic materials display both elastic and viscous properties. A Kelvin-Voigt material (solid line) behaves like a viscously at short times but elastically at long, returning to its original shape after stress. A Maxwell material (dashed line) behaves elastically at short times and viscously at long, remaining permanently deformed after stress.

mechanical strain so as to deform the junctions. This technique should give three periods to be evaluated: a baseline steady state, the experimental manipulation administering mechanical force, and the recovery period following force application. These three periods will allow for examining how force production alters the system to generate viscoelastic behaviors and resulting cell shapes. Indeed, a wide variety of approaches, with varying invasiveness, have been employed to discern the nature of mechanical forces on viscoelastic behaviors and their underlying mechanochemical regulation [21]. These studies have revealed a more passive type of viscoelastic stress dissipation at cell-cell junctions, in that there is no feedback between strain and tension [83, 102, 103].

Cell-cell adhesion dynamics are implicated in epithelial stress dissipation. Kinematic descriptions of tissue deformation in the Drosophila wing disc revealed much about the state of junctional viscoelasticity. Here, there is an eight-hour delay between changes in endogenous stress and junction elongation, indicating a viscoelastic behavior [83]. A Kelvin-Voight material, a material that is viscous at short timescales but elastic at long timescales, was used to model the observed relationship between tissue stress and junction elongation (Fig. 1.7). It was found that mechanical stress-induced E-cadherin turnover sets tissue viscoelasticity,

suggesting membrane and junctional remodeling tune cellular material properties. When E-cadherin turnover is high, the junctions deform more rapidly under stress and show a shorter delay between stress and cell elongation [83]. This is in line with recent work documenting how endocytosis regulates junction remodeling and elasticity [66].

Local mechanical measurements of junctions have also revealed viscoelasticity resulting from actomyosin turnover. Using optical tweezers to locally manipulate junctions revealed important timescales in the mechanics of junction deformability in the Drosophila Germband [104]. Here, transient morphogenetic forces generated stable junction length changes if they lasted longer than a minute [102]. Depending on the timescale of tweezing, junctions behavied like a Maxwell material: elastic at short timescales and fluid at longer timescales. These behaviors were dependent on actomyosin to control dissipative mechanics, as embryo treatment with Cytochalasin D, which slows actomyosin turnover rates, resulted in an increased disspiation timescale. Viscoelasticity seems to be a conserved feature of junctions, as optical tweezers in the Chick embryo also shows similar viscoelastic deformations of cell-cell junctions dependent on NMII activity [103]. Together these data suggest that turnover of actomyosin and adhesive structures tune stress dissipation necessary for junctional viscoelasticity, although they suggest a more passive viscoelastic model of cell-cell junctions.

1.4.3 Active viscoelasticity of cell-cell junctions

Exciting new findings have uncovered a new model for junctional viscoelasticity, termed *active* viscoelasticity, in which cells and tissues respond to strain by changing their contractile tension [94, 105, 106]. Certain feedback mechanisms therefore modulate the junction's active tension and passive viscoelastic properties to confer junction length. What arose from these data were new and interesting junctional phenotypes dependent upon the nature of the feedback in the system. As it became clearer that active viscoelasticity relied on the feedback between strain and tension, new methods and models have emerged to carefully dissect junction mechanics using quantitative and computational tools.

Recently, the Active Tension Network model was proposed, which assumes that junctional tension dominates tissue dynamics. Within this model lies the concept of active tension remodeling, where elongated junctions increase NMII recruitment, and contracted junctions decrease NMII recruitment, thereby regulating tensional homeostasis [106]. The Active Tension Network is consistent with recent work examining junction length changes within Drosophila Dorsal Closure [86]. Here, junction length is an active process, maintained by the coordinated action of mechanosensitive actomyosin localization and a straightness-dependent junctional removal system. Consistent with the Active Tension Network's predictions, squeezing embryos to stretch cell-cell junctions relocalized NMII from the medioapical pool to the cell-cell interfaces to drive subsequent remodeling. Junction NMII levels were proportional to the amount to which the cell perimeters were stretched. Together these data suggest that NMII can sense junction length, further indicating feedbacks between junction strain and tension.

Rheological studies on suspended epithelia have illustrated a similar active junctional viscoelasticity. In these experiments, the monolayer experienced a period of strain before a period of relaxation. Stress dissipated in the cells within the monolayer, with the length of the tissue permanently elongating and buckling once strain was removed. Stepwise applications of stress showed that single cells and monolayers switched from a fluid-like behavior at second timescales to a solid-like behavior at the minute timescale. That both monolayer and single cell rheology displayed similar features suggested a mechanism by which adheesive structures allowed the monolayer to behave like a single cell, with its rheology controlled by actomyosin turnover [105]. The resulting junctional relaxation period was succesfully captured using a viscoelastic model, but in which the timescale for relaxation was strain dependent, as larger strains slowed remodeling rates. One interpretation is that as junctions were stretched further, cell area increased and thus actin concentrations in thee cell decreased, reducing the rate of remodeling. Similar tissue experiments using the Drosophila wing disc showed rapid, mechanosensitive changes to tissue stiffness and elasticity that were also

dependent on actin turnover [107]. Together these data describe a new phenomenon emerging in the data describing feedbacks between strain and tension, giving rise to the concept of adaptive mechanics of epithelial cell junctions. While this concept of adaptive mechanics is appealing, we have historically lacked suitable techniques capable of systematically modulating intercellular stresses in both space and time. As such, new techniques are necessary to test these simple hypotheses derived from mathematical models. Much empirical work is therefore needed to confirm and enhance these canonical models.

1.5 Format of Thesis

The work described here takes a microscopic view of junction deformation resulting from heightened RhoA activity. Key questions remain regarding RhoA's role in regulating junction length, mainly, how a junction responds and adapts to the duration, amplitude, and frequency of the RhoA signal. The molecular basis of RhoA-mediated junction contraction and subsequent stabilization has yet to be explored, as well. Additionally, physically characterizing how a junction deforms to local stress has not been previously examined. Using model human colorectal adenocarcinoma cells (Caco-2 cells) expressing the TULIP optogenetic system, I can ask how RhoA is necessary and sufficient to induce junction contractility and characterize resulting junction deformations along the junction's length. With various pharmacological activators and inhibitors of RhoA activity, I can further examine RhoA's function in junction length determination even at the tissue scale. I couple this work with mathematical modeling to enhance the Vertex Model to recapitulate our experimental data. The content of each chapter is briefly described below.

Chapter 2: Optogenetic control of RhoA to probe sub-cellular mechanochemical circuitry

This chapter gives a detailed account on the use of the TULIP optogenetic system to manipulate RhoA signaling. I compare this probe to other available optogenetic systems and outline the engineering logic for the chosen recruitable RhoGEFs. I provide

an overview of the history behind TULIPs and document the recent technological advancements involving light-dependent protein recruitment. I also describe how to generate the cell line, spatially control illumination, confirm optogenetic control of RhoA, and mechanically induce cell-cell junction deformation in cultured tissues. Taken altogether, this chapter provides the detailed protocols used in this dissertation work.(Published)

Chapter 3: RhoA mediates epithelial cell shape changes via mechanosensitive endocytosis

This work documents how RhoA governs transient changes in cell-cell junction length, and how these changes are rectified to produce irreversible junction deformation. Here, I use optogenetics to characterize responses to pulsatile RhoA in model Caco-2 cells in culture. I find that RhoA activation along the junction length leads to a rapid contraction. For short activation times, this shortening is reversible such that junctions return to their original lengths after removal of the exogenous RhoA. However, as the activation time is increased, the extent of permanent junctional shortening is limited for a single activation pulse and saturates over long periods of time. To capture these data, I collaborated with theoretical physicists and together we introduce modifications to the existing vertex-based models for epithelial tissues to include strain-dependent remodeling of junction tension and rest length. To account for our experimental data, our model must include junctional tension remodeling that occurs only above a critical strain. I further show that temporally structuring the exogenous RhoA activity into distinct pulses overcomes the limited shortening, highlighting an essential role for pulsatile activation of RhoA. Finally, live cell imaging reveals that membrane remodeling and vesicular internalization occur during this RhoA-dependent junction contraction, whose stabilization at shorter lengths requires dynamin and formin activities. Altogether, these data provide new insights into the molecular and biophysical feedback mechanisms between RhoA activity and membrane remodeling that underlie junctional length changes in epithelia. (Published)

Chapter 4: Feedback between RhoA and E-cadherin elicit an asymmetric junctional mechanoresponse

During RhoA-mediated ratcheted contractions, vertices exhibit sliding behavior. Here, a motile vertex contracts into a more non-motile vertex to facilitate junction shortening. While this phenomenon is well characterized in development, the molecular, cellular, and mechanical origins of this contractile asymmetry remain largely unknown. In this study, I use the same optogenetic system, this time selectively labeling E-cadherin molecules to provide for fiduciary marks to track within kymographs. Kymograph analysis shows that junction contraction is uniform along the junction length, but culminates in an asymmetric junction contraction. Using pharmacological activators of RhoA to exogenously increase junction tension, I show that RhoA flares appear along the junction length and persist over the course of junction shortening. These RhoA flares are skewed towards the less-motile vertex and correspond to the center of junction contractions in my optogenetic system. These data indicate that the location of RhoA is critical in designating vertex motion, as proximal RhoA correlates with the less-motile vertex. Collaborating with theoretical physicists, together we find that canonical Vertex Models are insufficient to explain vertex asymmetry, as simulations failed to recapitulate experimental data. Instead, we find that Vertex models recapitulate data when there is feedback between RhoA and E-Cadherin, causing a pooling of E-Cadherin at tricellular contacts to increase vertex friction. By modulating frictional drag using pharmacological compounds against E-Cadherin, I further find that this either induces vertex symmetry or reduces asymmetry to decrease junction contractions. Together, these data point to a new, exciting view on vertex motion that describes a feedback mechanism of opposing RhoA-mediated tension increases and E-Cadherin-mediated frictional drag. (In Preparation).

CHAPTER 2

METHODS: OPTOGENETIC CONTROL OF RHOA TO PROBE SUB-CELLULAR MECHANOCHEMICAL CIRCUITRY

2.1 Overview, aims, and contributions

The work described here gives the detailed protocols and workflow that were used in Chapters 3-4. In this Chapter, I first describe the history of the TULIP system. I then compare this probe to other available optogenetic systems and outline the engineering logic for the chosen recruitable RhoGEFs. I also describe how to generate the cell line, spatially control illumination, confirm optogenetic control of RhoA, and mechanically induce cell-cell junction deformation in cultured tissues. Together these basic protocols will detail how to probe mechanochemical circuitry that is downstream of RhoA signaling. This work was published in Current Procotols for Cell Biology.

The aims include the following:

- To detail the history of TULIPs and highlight its recent innovations
- To list and compare various two-component optogenetic tools
- To describe the engineering logic behind the optogenetic constructs
- To describe how to design and implement an optogenetic experiment
- To provide troubleshooting tips and critical information

The contributions are as follows:
Kate Elizabeth Cavanaugh: Manuscript preparation, review and editing of the manuscript.
Patrick Oakes: Review and editing of the manuscript.
Margaret Gardel: Review and editing of the manuscript, supervision of work.

2.2 Introduction

Spatiotemporal localization of protein function is essential for physiological processes from sub-cellular to tissue scales. Genetic and pharmacological approaches have played instrumental roles in isolating molecular components necessary for sub-cellular machinery. However, these approaches have limited capabilities to reveal the nature of spatiotemporal regulation of sub-cellular machineries like those of cytoskeletal organelles. With the recent advancement of optogenetic probes, the field now has a powerful tool to localize cytoskeletal stimuli in both space and time. Here, we detail the use of the tunable light-controlled interacting protein tags (TULIPs) to manipulate RhoA signaling in vivo. This is an optogenetic dimerization system that rapidly, reversibly, and efficiently directs a cytoplasmic RhoGEF to the plasma membrane for activation of RhoA using light.

To gain a better understanding of how signaling achieves spatiotemporally structured sub-cellular protein complexes and cytoskeletal organelles, we must be able to exert experimental control over these signaling pathways. The use of light-sensitive moieties, in combination with structured illumination, provide a promising route. In the past, the availability of photo-responsive elements that allow for switching, binding or uncaging have been limited. Recent advances in optogenetics have allowed for the molecular dissection of spatiotemporal signaling modules. Optogenetics utilizes photosensitive proteins that change conformation upon exposure to specific wavelengths, resulting in altered protein-protein interactions and modulation of downstream signals. This technique is appealing, as it can be used to study the effects of the location, intensity, periodicity, and duration of light pulses and subsequent signaling activity.

2.2.1 History of the TULIP system

Nearly a decade ago, a seminal paper by Strickland et al was published describing how light-sensitive protein domains could be repurposed as optogenetic dimerization tools [108].

This initial study introduced the light-oxygen-voltage sensing (LOV) domain of Avena sativa phototropin 1 (AsLOV2). LOV domains' conformations are light-sensitive, making them ideal for optogenetic use. This system was named TULIPs, as they are tunable, light-controlled interacting protein tags. In their original paper reporting the use of the TULIP system, Strickland et al successfully documented the activation of two cellular signaling modules in yeast. Specifically, they dissected the yeast mating pathway induced by a canonical GPCR pathway. This pathway is responsible for a MAPK cascade associated with both growth arrest and polarized secretion. First, they documented light-dependent recruitment of a truncated Ste5 and full-length Ste11 to activate the MAPK pathway for subsequent cellular growth arrest. They then demonstrated that this system could successfully be used for the control of GTPase signaling. Here, they used light-directed recruitment of Cdc42 to induce mating projections, or shmoos, in a polarized fashion. Together these data showed the effectiveness of the TULIP system in regulating the activity of nucleotide-exchange factors, scaffold proteins, and kinases.

RhoA signaling is an ideal signaling pathway for optogenetic control. Rho-dependent signaling, regulated in space and time, drives a myriad of biological processes (e.g. development, homeostasis, and disease) [1]. RhoA is a small, membrane bound, GTPase that largely controls the cellular basis of contractility through activation of its downstream effectors, actin and myosin [109]. RhoA activation is achieved by nucleotide exchange mediated by Guanine Nucleotide Exchange factors, or GEFs. The optogenetic strategy here is elegant: drive the localization of a RhoA-specific GEF to the plasma membrane for centralized activation of RhoA and its subsequent downstream effectors (Fig. 2.1). Recent optogenetic tools have subcellularly localized RhoA GEFs for RhoA activation in dividing, non-adherent, and adherent cells in culture, and more recently in tissue both in culture and in vivo [94, 110–116]. These studies have successfully probed the complex nature of RhoA-mediated contractility on cell-cell and cell-matrix forces, in addition to deciphering mechanosensitive signaling pathways that regulate cellular morphology and tissue-scale morphogenesis.

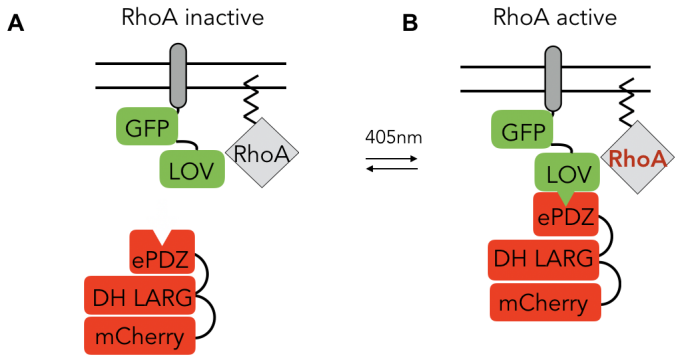

Figure 2.1: A) Schematic of the TULIP system in the dark state. Stargazin-GFP-LOVpep sits in the closed confirmation at the plasma membrane next to inactive RhoA. The 2x-PDZ-mCherry-LARG sits diffusely in the cytoplasm. B) Schematic of the TULIP system in the activated state. 405nm light causes a conformational change of the Stargazin-GFP-LOVpep that increases the binding affinity to the 2X-PDZ-mCherry LARG, recruiting it to the membrane where it activates RhoA.

Specifically, the TULIP system has proven to be a versatile tool in this analysis of mechanochemical signaling in driving the formation of sub-cellular cytoskeletal organelles. RhoA activation drives spatiotemporally structured sub-cellular organelles like those of the cytokinetic ring, actin stress fibers, or the contractile actin belt anchored at adherens junctions, to name a few. Using the TULIP system, Wagner and Glotzer exogenously activated RhoA to find that it was sufficient to induce cytokinetic furrow formation in single anaphase cells [110]. In Oakes et al 2017, the system was used to probe the molecular basis of actin stress fiber elasticity in single cells, showing a zyxin-dependent mechanism [113]. Altogether, these studies show the diverse applications of the TULIP system. We believe that with the right engineering, optogenetic RhoA can be used for any application. Further studies using optogenetically activated RhoA will only continue to advance our understanding of cell and tissue mechanics.

2.2.2 The LOV domain

LOV domains are comprised of a flavin-based, light-sensitive chromophore. In microbes and plants, these LOV domains regulate light-mediated biological phenomenon [117]. Specifically, the AsLOV2 protein houses a core per-arnt-sim (PAS) fold with flanking alpha helicies on both the N- and C-termini [118]. With blue light exposure and absorption, the AsLOV2 core binds to the flavin cofactor via a conserved cysteine residue. This binding causes conformational changes that propagate along the PAS fold, leading to the uncaging of a ∼20 amino acid amphipathic C-terminal alpha helix [119]. This C-terminal α-helix is known as the Jα helix. The beauty of this system lies in its reversibility; in the dark-state the Jα is left intact but light stimulation can expose linear motifs in its amino acid sequence. Therefore, reversible caging of the Jα can lead to masking or unmasking of signaling protein activity with light.

The nature of Jα is such that it can block certain peptide epitopes in the AsLOV2 core. Upon photoexcitation, the Jα can undock and expose this specific epitope. This feature of the AsLOV2 protein is useful because it can be used to design a binding partner to create a dimerizable protein complex. For the AsLOV2's binding partner, the original Strickland paper used the high-affinity, high-specificity engineered variant of the Erbin PDZ domain, ePDZ-b1 [120]. This domain is small at about 194 amino acids. The ePDZ domain's affinity and lifetime in the photoexcited state are tunable by various mutations, effectively tuning downstream signaling events [108]. Recently, this system has been improved upon by substituting the ePDZ-b1 domain with a tandem PDZ tag that is functional in more diverse protein fusions [110].

2.3 Strategic Planning

2.3.1 Choosing the Optogenetic System

A number of dimerization systems have been developed, each with diverse properties for different biological applications. The choice of optogenetic system will depend on factors

such as wavelength compatibility, dynamic range, and requirements for activation speed, reversibility, and depth of tissue to be imaged. We recommend choosing the optogenetic system with the desired reversibility kinetics, as this is important for achieving local, spatially resolved subcellular control of signaling processes. Fast dimerization kinetics can be on the order of seconds, while slower kinetics are on the order of minutes to hours. Systems with slow reversal kinetics may be particularly useful if a more permanent phenotype is desired, or more persistent signaling is needed. However, since physiological signaling occurs within milliseconds to seconds, we recommend using faster dimerization kinetics to mimic in vivo signaling kinetics. The current optogenetic dimerization systems are listed in Table 2.1.

Many systems have already been published for subcellular control of RhoA. If fast kinetics are desired, we recommend using the iLID/SspB or TULIP system, as these provide high temporal resolution of RhoA activation. The RhoGEF in TULIPs associate within less than 10 seconds and dissociate within 30-60 seconds [110, 113]; the iLID/SspB system shows similar association and dissociation kinetics [111, 112]. Slower kinetic systems have been seen with the CRY2/CIBN light-gated dimerization system. This CRY2/CIBN system was used to manipulate RhoGEF association within minute timescales but RhoGEF dissociation was on the order of 20 minutes [115]. In this case, actin accumulated and dissipated with similar kinetics as the RhoGEF. As such, the CRY2/CIBN system provides for a more permanent phenotype associated with RhoA contractility. This slower system, while not typically physiological, can provide for persistent actomyosin recruitment and RhoA signaling that can be used to study the effects of traction forces on substrates, for example. With fast or slow recruitment kinetics, the major strength of using an optogenetic approach is the ability to image a baseline state prior to activation, the response during activation, and a recovery period following activation. These three periods give key insights into the behavior and response of junctions and/or effector proteins with respect to the activation of RhoA.

System	Association λ	Dissociation λ	Tag Sizes (aa)	Lifetime	Reference
PhyB/PIF6	660nm	740nm	908/100	Inducible	[80]
Cry2-CIBN	450nm	Dark	498/170	5-10 min	[121]
iLID/SspB	450nm	Dark	144/110	<50sec	[122, 123]
TULIPs	450nm	Dark	153/194	<50sec	[108]
nMag/pMag	450nm	Dark	150/150	Tunable	[124]
FKF1/GI	450nm	Dark	619/1173	Hours	[125]
LOVTRAP	Dark	450nm	143/59	Tunable	[126]
PixD/PixE	Dark	450nm	150/380	Sec-min	[127]
BphP1/PpsR2	740nm	650nm	732/465	Inducible	[128]
UVR8/COP1	280nm	N/A	440/340	Permanent	[129]

Table 2.3.1: Optogenetic Dimerization Probes

2.3.2 Engineering the Optogenetic Constructs

When engineering the photosensitive protein, it is necessary to consider the desired subcellular location for recruitment. Most studies to date have anchored the photosensitive protein to the plasma membrane where RhoA sits inactive. Here, we describe the use of the TULIP system that utilizes the photosensitive LOVpep domain attached to a transmembrane protein, Stargazin [108] (Fig. 2.1). Recent papers have also probed membrane recruitable RhoGEFs using various photosensitive proteins attached to a CAAX motif, which triggers posttranslational modifications necessary to drive the protein's plasma membrane association and insertion [111, 112, 115]. It is also conceivable to drive RhoGEF localization to other more specific areas within the cell, under the logic of sequestering the RhoGEF away from the plasma membrane. For instance, one study drove RhoGEF activity specifically to the outer mitochondrial membrane by fusion to the mitochondrial matrix targeting sequence from subunit VIII of cytochrome c oxidase [115]. Other targetable proteins may be apicojunctional proteins like E-cadherin, ZO-1, or members of the PAR polarity family, although nearly any

protein can be conceivably targeted with the right design.

RhoA is activated when the recruitable GEF binds to the photosensitive protein at the plasma membrane upon light activation (Fig. 2.1). GEFs are multidomain proteins capable of catalyzing nucleotide exchange within Rho GTPases [130]. The full sequence RhoGEF houses the catalytic DH domain and additional protein and/or lipid interaction motifs, suggesting that these domains act as protein scaffolding complexes and/or localization signals [9]. In nearly all isoforms, the catalytic DH domain is found adjacent to a PH domain that commonly binds to phosphoinositide ligands [8] and may even aid in nucleotide exchange [10]. Other common functional domains include the SH3 and PDZ protein binding domains and the RGS autoinhibitory domain, to name a few [10]. It is therefore vital to consider which type of GEF is used as a dimerizer because different GEFs can result in diverse subcellular behaviors depending on the sequence motifs used [8]. As such, designing this optogenetic piece will depend on the nature of the experiment and desired subcellular behaviors.

With TULIPS, the LOVpep's cognate binding partner is an engineered tandem PDZ domain attached to the catalytic DH domain of the RhoGEF LARG (Fig. 2.1) [110]. The DH domain of LARG is a potent RhoA-specific activator and exhibits the highest catalytic activity reported for its GEF family [131]. Other groups have used the DHPH domain of the Drosophila-specific RhoGEF2 [116], the DHPH domain of LARG [111, 112], or the DHPH domain of ARHGEF11 [115]. While others have included the PH domain in their recruitable GEF complex, we recommend engineering dimerization constructs that only utilize the GEF's catalytic DH domain to reduce basal GEF activity. Isolating the DH domain removes functional domain compositions and domain organizations that link GEF activity to specific downstream signaling modules. For example, the PH domain of PDZ-RhoGEF has been shown to bind to activated RhoA to drive a potential feedback loop that either attenuates or enhances RhoA function [132]. This effect may not be desirable in an optogenetic system, as activation of a feedback loop may result in unwanted phenotypes resulting from altered RhoA function. Additionally, in some GEF proteins, the PH or the RGS domain may act

upon the DH domain in an autoinhibitory fashion, preventing RhoA activation despite any GEF photorecruitment [10, 133].

Visualization and confirmation of these optogenetic proteins depends on their fluorescent tags. Tagging the anchored LOV domain to GFP aids in confirming the uptake of the probe in screening and sorting the cells. Additionally, we recommend tagging the desired RhoGEF with mCherry or another red protein variant to confirm its localization and recruitment. It is also possible to tag the 2XPDZ-LARG with a far-red protein or Halo tag conjugated with the Janelia Fluor far-red protein. There is also a commercially available YFP-2XPDZ-LARG that frees up the red channel. However, confirming the presence of this probe in cells is more difficult and relies on the visualization of either downstream effectors and relocation from the cytosol to the membrane to confirm the presence of the recruitable GEF.

When cloning, be conscious of the linkers between the LOVpep or PDZ domains and their respective proteins of interest. Linkers, or lack thereof, can affect the desired protein's conformation. This is especially important if tagging a protein that houses specific signaling functions, such apicojunctional proteins or RhoGEFs that localize the cytoskeletal machinery. The design of a suitable linker to join protein domains can often be complicated. Careful attention needs to be paid when designing a linker with the right length, hydrophobicity, amino acid residue, and secondary structure. Flexible linkers have preferable amino acid residues that are composed of small, non-polar (e.g. Gly) or polar (e.g. Ser or Thr) amino acids [134]. The most commonly used flexible linkers have stretches of Gly and Ser residues, the length and copy number of which can be optimized to separate the functional domains. For the LOVpep, we have successfully used the flexible linker GGSGGSGGSPR, while for the tandem PDZ we have used QSTVPRARDPPVAT [110, 113]. Other linkers for optogenetic tags include GSGGSGSGGT [126] or GSTSGSGKPGSGEGSTKG [135]. These published linkers are sufficiently long and flexible so as to not affect the binding of the protein to its downstream effectors. For the anchor protein, when using a CAAX motif or another targeting sequence to a specific subcellular location, linkers are optional.

2.4 Protocols

2.4.1 Generation of a stable line expressing TULIP constructs

The nature of the experiment necessitates different protein expression systems. To probe the effects of RhoA localization on cell-cell junctions within a tissue in culture, for example, we recommend generating a stable cell line constitutively expressing both dimerization constructs. This is because the likelihood of both optogenetic probes being present in two adjacent cells is very low. Transient transfections of both optogenetic probes may be sufficient for the analysis of RhoA activation in single cells, although generation of a stable cell line will greatly ease experimentation. This protocol will necessitate the cloning of optogenetic constructs into a lentiviral vector (e.g. pWPT), or other vector depending on the cell type (e.g. retroviral, adenoviral), for the generation of stable lines. We recommend using a viral vector with a selectable marker such as Puromycin resistance for cell selection.

This protocol will use the Fugene 6 transfection reagent to produce lentiviral DNA, which will then be used to create a stable cell line constitutively expressing both TULIP constructs. This protocol is designed to generate lentivirus of one optogenetic construct for infection of cells in culture. This experiment will have to be done twice in order to obtain lentivirus of the second optogenetic construct. Following successful expression and sorting of one construct, the cells can be transfected and sorted again with the second construct. Alternatively, you could infect WT cells simultaneously with both viruses and perform dual-channel FACS.

<u>Materials List:</u>

Lentiviral DNA vector containing desired constructs at concentrations 1ug/ul

293T cells (ATCC CRL-3216)

Opti-MEM (Gibco)

Polybrene (EMD Millipore)

FuGENE 6 Transfection Reagent (Promega)

0.45μm Millex syringe-driven filter unit (Millipore)

30mL Luer Lock tip Disposable syringe (ExellINT)

15mL conical tubes (Corning)

Centrifuge at room temperature

8-well chambers (Ibidi)

VSV-G pseudo typing plasmid at concentration 1ug/ul (Addgene #8454)

pHR1-8.2-delta-R packaging plasmid at concentration 1ug/ul (Addgene #12263)

Protocol Steps:

Day 0: Preparation of the cells for infection

1. Plate 293T cells at 80% confluence

Day 1: Transfection of 293T cells.

1. Assemble reaction as follows and let sit for 10 minutes:

   7.5μl Lentiviral vector, 5μl dR8.2, 1.25μl VSVG, 685μl Optimem, 33.75μl FUGENE

2. Add complexes to 10ml of fresh media to the plate of 293T cells
3. Place cells into the incubator and let sit for 3 days

Day 3: Isolating the virus for infection

1. Collect supernatant.

   At this time, all reagents touching lentivirus should be bleached and put into a biohazard bag. Wear double gloves and a lab coat to protect the skin

2. Spin down virus-infused media to remove any remaining cells
3. Carefully collect the supernatant
4. Filter sterilize the supernatant with the 0.45μm Filter and 30mL syringe

This step will remove any debris

5. Add 2ml of the lentivirus, 4μg/ml Polybrene, to 6ml of fresh media to desired cell line.

   We recommend snap freezing the rest of the virus for later use in case the infection did not work. Place in the -80 freezer.

6. Place cells in the incubator and let sit for a day

Day 4: Cleaning the optogenetic cells

1. Remove media from the dish. Bleach the waste, as the virus is still a hazard
2. Wash the dish with PBS. Bleach the waste, as the virus is still a hazard
3. Replace with fresh media on the optogenetic cells
4. Place the optogenetic cells in incubator

Day 6+: Isolating the optogenetic cell line

5. Allow the optogenetic cells to grow for a few days
6. Once the cells have been expanded, sort cells for the desired fluorescence via FACS.

   We find that relatively low levels of Stargazin-GFP-LOVpep are tolerated quite well. However, a high expression of mCherry-2xPDZ-LARG is needed to produce a marked cellular response. We recommend sorting the cells for highest 50% expression of the Stargazin-GFP and top 5-10% highest expressing mCherry-2xPDZ-LARG.

7. Screen the cell clones for optimal expression of optogenetic constructs.

   Split each of the clonal populations in media, one portion of the cells into a cell culture dish and one portion into one respective well in the 8 well Ibidi chamber. Make sure to keep a record of which clonal population is which. The density of plating can be varied depending on the experiment. To confirm expression of

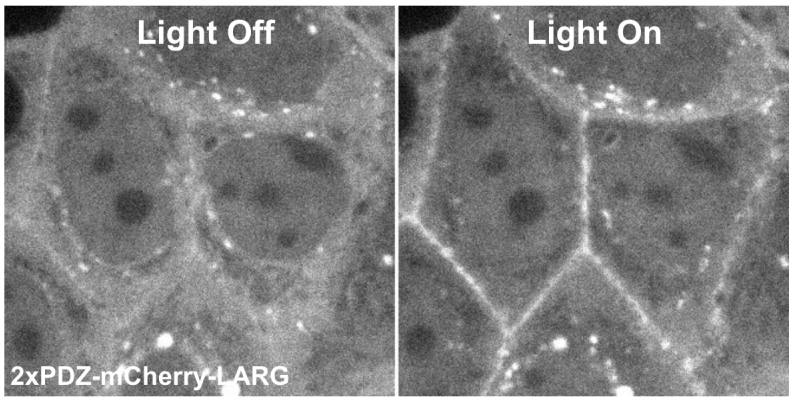

Figure 2.2: Representative images of a stable optogenetic cell line before and after light recruitment visualized by 2xPDZ-mCherry-LARG expression. Left: Image of the cells with the light off showing diffuse cytoplasmic localization of the 2xPDZ-mCherry-LARG. Right: Image of the cells with the light on showing junctional recruitment of the 2xPDZ-mCherry-LARG.

both of the constructs, first take an image in the mCherry channel, followed by an image in the GFP channel, and then again in the mCherry channel. If the cytoplasmic RhoGEF shifts localization to the junctions, this clone is primed for optogenetic activation (similar to Fig. 2.2).

8. Expand the selected clonal population for use in the next Protocols

2.4.2 Preparation of collagen substrates for imaging

The extracellular matrix (ECM) composition can have drastic effects on cellular behavior and morphology. We also find that the substrate greatly affects the cell junctions' response to exogenous RhoA. Here, we describe how to plate the cells on polymerized collagen gels that allow tissues to be grown on a soft (<2 kPa) fibrillar network, which we have found optimal to construct polarized epithelial monolayers. Alternative substrates, such as those generated using other ECM proteins like Laminin or Fibronectin, Matrigel, or ECM-coated polyacrylamide gels required for applications like traction force microscopy, can also be used. The substrate composition will depend on the specific experiment. Yet for experiments examining cell-cell interactions using monolayers, we recommend making the substrate as soft as possible. Experiments examining interactions between cell-

matrix adhesions may require different substrates. Successful completion of this protocol should result in a 2mg/ml collagen gel that is less than 300μm thick atop a glass chamber.

Materials List:

Culture media - DMEM (Sigma-Aldrich)

1.5ml Eppendorf tubes

Rat tail collagen 1 (Corning)

1M Hepes (Mediatech, Inc.)

7.5% $NaHCO_3$ (Thermofisher scientific)

Four-well chambers (Ibidi)

Chilled pipette tips

Cells (see Protocol 1)

Ice

Protocol Steps:

1. Place the collagen and an Eppendorf tube on ice to chill.
2. Add 198μl media to the Eppendorf tube and let chill.
3. Add 10μl HEPES to the Eppendorf tube and let chill.
4. Add 11.9μl$NaHCO_3$ to the Eppendorf tube and let chill.
5. Pipette 280.1μl collagen slowly into the mixture using chilled pipette tips.

a. Let the tip equilibrate to the temperature, keeping the Eppendorf tube in the ice.

6. Pipette up and down while stirring the tip in the Eppendorf tube.
7. Let the collagen mixture polymerize off the ice.

   Collagen will start polymerizing the instant it is off the ice. For a more meshy collagen, plate immediately onto the chambers. For more bundled collagen, let sit as a liquid for longer than 5 minutes.

8. Paint 80-100μl of the collagen mixture onto the glass chamber with the pipette tip

Make sure to go into all the corners and avoid bubbles. The volume used will alter the collagen gel thickness and, if using a different chamber, this will need to be changed. The collagen gel thickness should be confirmed at the time of cell imaging. This can be done using fluorescently labeled collagen and imaging a z-stack of the collagen proper.

9. Put the chambers in the incubator for at least 5 minutes to allow the gels to solidify.
10. To avoid the collagen drying, put about 150μl of DMEM on top of the gel.
11. In the dark cell culture hood, plate the cells in DMEM

2.4.3 Transient transfection for visualization of downstream effectors

It is critical to confirm the localization of RhoA and any downstream effectors upon RhoA activation. Downstream effector analysis is accomplished by using reporters of RhoA activity typically through transient transfection. These reporters can include RhoA's direct downstream effectors, Actin and Myosin. RhoA activity can also be confirmed by using the RhoA biosensor, which houses the RhoA binding domain within the C-terminal portion of Anillin [136]. With Myosin and the RhoA biosensor, these constructs can be transiently transfected into the cells for confirmation of RhoA. For visualization of actin structures, there is a commercially available cell permeable far-red SiR-actin, yet we do not detail the use of this probe in this protocol. It is also possible to use non-fluorescent outputs such as traction force microscopy to confirm that RhoA activation is occurring [113].

When performing multi-channel imaging, it is important to take into account the spectral overlap between optogenetic photoexcitation and fluorescence imaging. The broad blue-light sensitivity of the LOV domains prevents imaging in the GFP channel, since the LOVpep can be activated by blue light. Unfortunately, this limits the number of channels for imaging. If possible, the use of far-red fluorescent proteins and probes such as SiR-actin will allow for multispectral imaging. Since the number of far-red proteins is also limited, we commonly

use proteins fused with Halo tags and conjugate them with Janelia fluor far-red proteins for visualization.

In our system, we have found that Caco-2 cells are extremely sensitive to electroporation and often result in low transfection efficiencies (<20%), yet this may be dependent on cell type. For monolayers, we do not recommend using electroporation transfection methods, as it also results in marked cell death (>30-40%) that can hinder the growth of a confluent and polarized monolayer. Instead, we recommend forming the monolayer ahead of transfection using Protocol 2 and then using cationic liposome-based reagents like Lipofectamine 3000. For single cells, this is less of an issue and any transfection method can be utilized though efficiency will still vary. Here we describe a protocol that will use Lipofectamine 3000 to produce an epithelial tissue with transient expression of downstream effectors like the RhoA biosensor or myosin. However, this protocol can generally be used to transfect any protein of interest for analysis of the effects of junctional RhoA localization.

Materials List:

Lipofectamine 3000 Reagent (Thermo Fisher Scientific)

P3000 Reagent (2μL/μg DNA) (Thermo Fisher Scientific)

Opti-MEM (Gibco)

Reporter DNA at concentration of 1-5μg/μl

DPBS (Corning)

Culture media - DMEM (Sigma-Aldrich)

Cells in Ibidi chambers (see Protocols 1 and 2)

Vortex

Protocol Steps:

1. Plate cells in the 4-well Ibidi chambersin DMEM

Can plate either at 100% confluency, or let cells grow into a confluent monolayer

2. In the dark, gently wash the optogenetic cells with 1ml prewarmed DPBS
3. Replace media with 250μl opti-MEM 30min-1h before transfection
4. Place optogenetic cells in the incubator until the transfection reagents are ready
5. Warm all reagents to room temperature
6. Make two 125 aliquots of opti-MEM (A and B)
7. To tube A: add 6ul lipofectamine 3000
8. To tube B: add 2.5-5μg DNA, then 5μl of P3000 and mix gently
9. Add all the contents of Tube B to Tube A. Mix gently.
10. Incubate for 10-15 minutes at room temperature
11. In the dark cell culture hood, gently add mixture as small drops to one Ibidi well
12. In the dark, change the opti-MEM for DMEM 12h after transfection
13. Analyze transfected cells 24-48 hours after transfection

2.4.4 Calibration of spatial illumination

Here, we describe our particular microscope set up and calibration protocol for optogenetic activation using MetaMorph software. While each microscope setup will be different, the most important piece of equipment is the digital micromirror device (DMD) coupled to a light source. The DMD is an intricate array of hundreds of thousands of hinge-mounted, adjustable mirrors that are controlled via microscope acquisition software (e.g. MetaMorph). Mirrors that fall within the regions of interest drawn on the computer are rotated into the light path to reflect light from the source onto the sample. This setup has the advantage of illuminating all pixels in the region of interest simultaneously. To ensure accuracy, the system should be calibrated before each experiment and for each objective used. Calibration is typically performed by clicking on a series of markers displayed in sequence by the DMD. This process registers the DMD to the camera pixels. DMD chips are typically smaller than the FOV of the camera, and thus it is often useful to save a region of the fully illuminated chip as a reference for choosing regions during the actual experiment. Successful completion

of this protocol will calibrate the DMD system for use in the next protocol.

Please note: Any change in the optical setup (e.g. objectives, filters, etc...) will require recalibration of the DMD. It is a good habit to simply perform the calibration before each experiment to ensure proper alignment and thus targeting of the activation.

Materials List: Nikon Ti-E inverted microscope (Nikon)

Yokogawa CSU-X confocal scanning head (Yokogawa Electric)

Zyla 4.2 sCMOS Camera (Andor)

60x 1.49 NA ApoTIRF oil immersion objective (Nikon)

MetaMorph Automation and Image Analysis Software (Molecular Devices)

Mirror slide

Mosaic digital micromirror device coupled to a 405nm laser (Andor)

Laser merge model with 491, 561, and 642nm laser lines (Spectral Applied Research)

Protocol Steps:

1. Turn on the microscope, Mosaic DMD, and light source
2. Turn on the calibration flashlight perpendicular to the Mosaic light path
3. Insert the 100% mirror in front of the flashlight, make sure the light path is clear
4. Add immersion media to your objective
5. Put the mirror slide in the slide holder with the mirrored surface closest to the objective
6. Using transmitted light, focus on scratches in the mirror surface until they are crisp
7. Rotate the Mosaic filter cube into position below the objective
8. Under the "Devices" menu, select "Mosaic Targeted Illumination"

   This will open up the control panel (Fig. 2.3A)

9. Set the Illumination setting (during pulse) to Mosaic
10. Set the coordinate system setting to the desired objective (Fig. 2.3A)

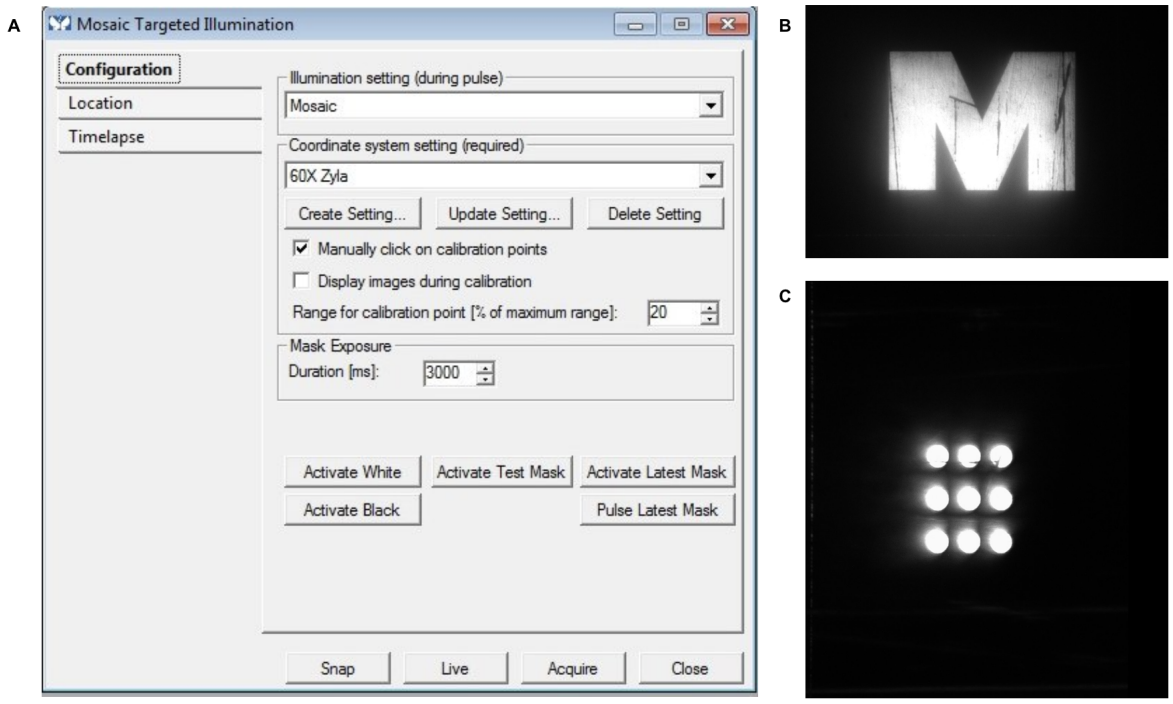

Figure 2.3: The Mosaic Targeted Illumination control box. A) Image of the Configuration toolbox within the Mosaic Targeted Illumination device box showing the Illumination setting to the Mosaic. Coordinate setting system is to 60x Zyla. Mask exposure is set to 3 seconds. Activate Test Mask button is shown before the Mask Exposure setting. B) Image showing the activated test mask "M". C) Image showing the completed, manually clicked calibration points for device calibration.

Make sure the objective magnification (Mag setting) in Metamorph matches the coordinate system setting

11. Click "Activate Test Mask" (Fig. 2.3A)
12. In the Acquire Box, click Live to show the Test Mask (Fig. 2.3B)

At this point you should see the M on the live screen. Focus so the M becomes crisp and clear

13. Stop live imaging and click Update setting
14. Click on the center of each white dot as it is displayed

When all 9 dots have been clicked, the system will be calibrated (Fig. 2.3C)

15. Confirm that that the system is calibrated

    Draw an arbitrary region on the image and test the illumination

16. Remove the 100% mirror from in front of the calibration flashlight
17. Turn off the calibration flashlight and turn on the illumination light source

    Turn on the illumination light source to the desired intensity by clicking Low and High within the Laser Controller (Fig. 2.4)

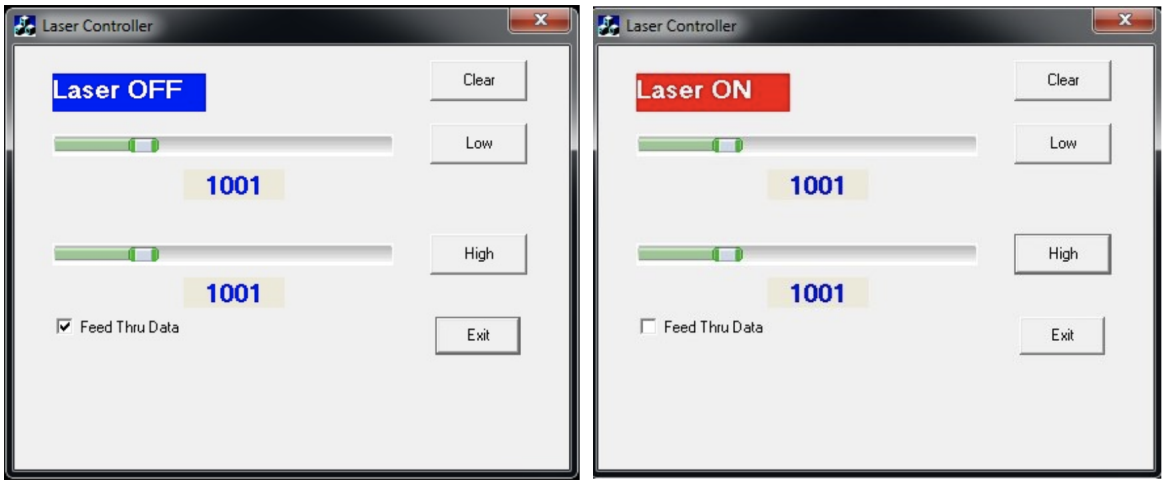

Figure 2.4: The Laser Diode Controller. Left) Image of the laser controller with the laser in the OFF state. Right) Image of the laser controller in the ON state set to 1000AU.

2.4.5 Optogenetic activation of a region of interest

In this protocol, we describe how to use the mosaic micromirror device to induce RhoA activation by light localization within a region of interest (ROI). We generally recommend imaging three periods: a baseline state prior to activation, the response during activation, and the recovery period following activation. For example, we have imaged the junction's steady state for 10 minutes before a 5-minute activation and then documented junction recovery for 15 minutes post-activation (Fig. 1.6). This scheme allowed us to evaluate any cellular or protein response to exogenous RhoA activation. However, this protocol necessitates

optimization. Within the activation period, there may be variations in pulse duration, pulse frequency, and interval spacing of RhoA activation that is dependent on the nature of the experiment. We recommend taking some time to establish optimal activation schemes as necessary for each experiment. Successful completion of this protocol will produce timelapse images of cell junctions undergoing deformations resulting from exogenous RhoA.

Please note: While we detail here the use of the mosaic micromirror with the Targeted Illuminated system using MetaMorph, other acquisition software and hardware setups exist. Acquisition can be streamlined journals which are beyond the scope of this protocol.

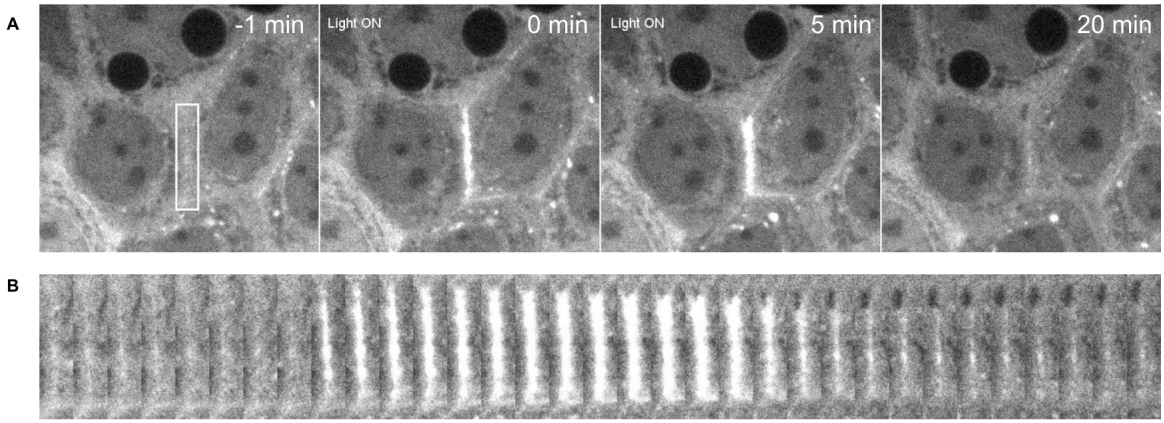

Figure 2.5: Targeted junction activation. A) Representative images of a stable optogenetic cell line expressing 2xPDZ-mCherry-LARG before, during, and after targeted junctional optogenetic activation. Image shows ROI of activation (White box) inducing junctional localization of the GEF and shortening of the targeted junction over a 5 minute activation, with a 15 minute relaxation period showing reversal of any junction contraction. B) Representative kymograph showing expression of the 2xPDZ-mCherry-LARG before, during, and after targeted junctional activation.

Protocol Steps:

1. Make sure the mosaic light source to the sample is free of any obstruction
2. Turn on the mosaic laser using the Laser Diode Control (Fig. 2.4)

   The laser power here needs to be determined empirically so that the optogenetic cells can be activated. This will be determined in part by the optics of the

individual microscope. Due to its high sensitivity, only a very small amount of light is actually needed to activate the protein. We, and the lab of Tobin Sosnick, also found that too much light hinders the activation of the LOV protein. We have had success generating contractile responses at junctions using light intensities between 6.7uW and 10.5uW (750-1000AU), with a minimal junctional response at 4.3uW (500AU).

3. Place sample in the stage incubator in the dark, allow it to equilibrate

   The stage incubator will maintain the cells at 37C, whereas humidified 5% CO_2 will be maintained at 50C at its source to prevent condensation within its tubing.

4. Scan the cells for optimal expression of 2xPDZ-mCherry-LARG

   To confirm expression of both of the constructs, first take an image in the mCherry channel, followed by an image in the GFP channel, and then again in the mCherry channel. If the cytoplasmic RhoGEF shifts to the junctions, this cell is primed for optogenetic activation (similar to Fig. 2.2). Wait >5 min until all the 2xPDZ-mCherry-LARG has dissociated from the junctions and has returned to the cytoplasm. You can confirm this by taking another image in the mCherry channel to visualize cytoplasmic RhoGEF.

5. Draw an ROI to be targeted on the previously acquired image
6. In the Mosaic Targeted Illumination box, click Location (Fig. 2.6A)

   Make sure the coordinate system setting matches with the Mag setting

7. Select the image ROI and click the Active Region button in the Target Location box

   This will specify the drawn ROI as the mask. It is also possible to click All regions if multiple ROI's are drawn.

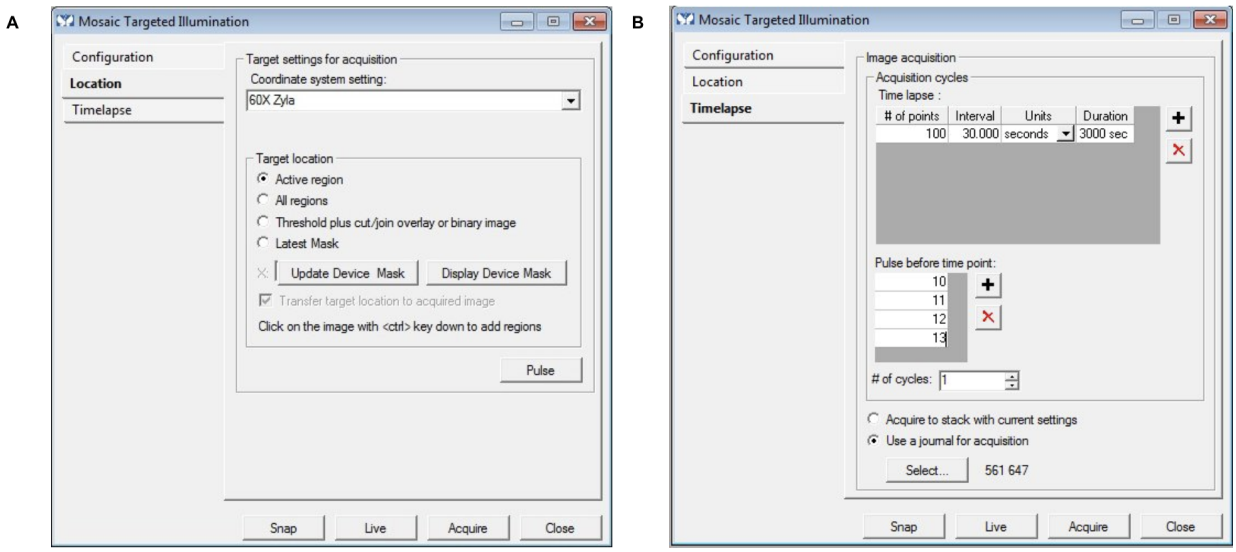

Figure 2.6: Mosaic Targeted Illumination settings. A) Image of the Location toolbox within the Mosaic Targeted Illumination device setting. Coordinate system setting is to 60x Zyla, with target location set to the Active Region. B) Time-lapse toolbox within the Mosaic Targeted Illumination device setting showing the number of timepoints set to 100 at 30 second intervals with pulses before timepoints 10-13. A journal is used to image the 561 and 647 channels during each of these timepoints.

8. In the Mosaic Targeted Illumination box, click Configuration (Fig. 2.3A)
9. Specify Mask Exposure Duration in milliseconds

   We use 1000ms but this can be subject to change depending on the nature of the experiment

10. In the mosaic targeted illumination box, click Timelapse (Fig. 2.6B)
11. Specify the acquisition cycles

    This step should be determined by the nature of the experiment, since different activation schemes require pulses at different timepoints. Typically during a period of activation we illuminate the ROI of interest with blue light prior to each timepoint. In Figure 2.6B, we have 100 timepoints at intervals of 30 seconds, with blue light pulsing before time point 10-13. Here, you can also use a journal for acquisition like using different color channels for acquisition. In our example

in Figure 2.6B we have a journal specifying images in both 561 and 647 to image the recruitable GEF and any far-red effector protein or far-red membrane stain.

12. Click Acquire in the mosaic targeted illumination box
13. Save Images under desired name
14. Save ROI for use in image analysis

2.5 Commentary

2.5.1 Troubleshooting

The RhoGEF is not recruiting: The RhoGEF should be visibly recruited to the membrane upon photoactivation (Similar to Fig. 2.2). If this is not the case, there may be a problem with the expression levels of the optogenetic probes. It is possible that the ratio of Stargazin-GFP-LOVpep and 2xPDZ-mCherry-LARG is not optimal. We then recommend choosing cells that have higher expression of either protein.

The cells are constitutively activating: It is a possibility that the light from bright computer monitors or ambient room light can activate the cells. This is because of the presence of blue light. This can be easily solved by keeping a far distance between the monitors and the sample or turning the computer away from the microscope. Keep the cells in the dark whenever possible.

Activation is occurring outside the targeted ROI: Make sure that the "active region" button is toggled in the Targeted Illumination control panel, and that the correct region is chosen.

The cells are blebbing or dying: We find it a common occurrence that the cells may bleb in other regions of the cell upon photorecruitment of the GEF. If this is the case, or if the cells are dying, it is wise to ease off the 405nm laser intensity. Too much laser power may result in an excess amount of RhoA activation that weakens the opposite membranes to cause cell blebbing or bursting.

The RhoGEF is aggregating: We see that the RhoGEF often aggregates, showing up as clumps in fluorescence. This is natural and a feature of the 2xPDZ-mCherry-LARG.

The junctions are not contracting: While we expect robust junction contraction upon RhoA activation, it is possible that the junctions may simply not contract. This can arise for a few reasons. First, it is possible that the light intensity levels are not high enough to produce a marked cellular response. Light intensities would then need to be increased. Second, it is possible that the RhoGEF expression levels are not optimal for RhoA activation. Here, we suggest choosing cells with higher RhoGEF expression. Third, we have also found clones of cells may express a variant of the recruitable RhoGEF that renders it unrecruitable, although this is rare. It is possible this is due to spontaneously occurring mutations in the DNA encoding the photosensitive dimerization domains, which are present in the DNA stock used to generate the stable cell line. We recommend sequencing the DNA used to make sure there are no mutations, otherwise use another isolated cell clone.

Perfect focus is not working: Painting 80-100μl of collagen should be sufficient to produce an even layer of polymerized gel. This is advantageous because this gel thickness is conducive to using Perfect Focus on many microscopes. If Perfect Focus is not working, it is possible that the gel is too thick. If so, consider using less collagen for a thinner gel. It is also possible to coat the chamber with 80-100μl and then aspirate the excess collagen to produce a very thin layer of a collagen gel.

The stable cell line is losing expression: A common problem that we have is dilution of the optogenetic constructs over time. This can be for a few reasons, although we believe that the cells expressing the optogenetic proteins are more prone to cellular extrusion because they are hypercontractile. To alleviate this, we recommend using cells at a low passage number. If the cells are still losing expression, we recommend fluorescently sorting the cells again to achieve better protein expression.

2.5.2 Anticipated Results

Cells with good expression of both optogenetic constructs can be photoactivated such that there is a marked increase in junctional RhoGEF compared to cytoplasmic RhoGEF, the latter which should reduce in fluorescence (Fig. 2.2). The photoactivated junction will be visually distinguishable when compared to other cells that have not been activated with 405nm light. The unactivated cells should have diffuse cytoplasmic localization of the RhoGEF. Upon RhoGEF recruitment, the activated junction will undergo contraction and noticeably shorten (Fig. 2.5), although the extent of this shortening may be dependent on the cell type used and light intensity. With this approach, junction lengths can be analyzed under WT and various inhibitor conditions. Additionally, the use of far-red protein labeling can allow for the visualization of the membrane, junctional components, or effector proteins as a result of RhoA localization and subsequent junction contraction.

2.5.3 Time Considerations

The largest time investment comes from obtaining the stable cell line. This may take a few weeks from infection to isolation and expansion of a clonal cell line. Careful attention needs to be paid when sorting and screening the cells for optimal fluorescence intensities, and multiple clones may need to be isolated to obtain the recruitable cell line with optimal expression levels of the optogenetic constructs. Time is also spent on optimizing the microscopy, including determining the light intensity and pulse duration. This may take a few optogenetic experiments to determine optimal microscopy parameters. Imaging can take anywhere from minutes to hours, depending on the desired activation scheme driving the wanted cellular behavior. A typical experiment, from plating the cells to the onset of imaging, should only take a few days. This is limited by how fast the cultured cells can grow into a confluent monolayer if testing cell mechanics at the tissue scale. At the cellular scale, cells can be plated the night before to ensure proper attachment to the desired substrate.

CHAPTER 3

RHOA MEDIATES EPITHELIAL CELL SHAPE CHANGES VIA MECHANOSENSITIVE ENDOCYTOSIS

3.1 Overview, aims, and contributions

The work described here takes a bottom-up approach to studying complex developmental mechanisms. Specifically, we use optogenetics to direct RhoA to cell-cell junctions to examine what is sufficient to drive cell-cell junction length changes.

The aims include the following:

- To determine the timescales at which RhoA directs reversible or irreversible junction length changes
- To examine physically how a junction contracts upon force application
- To derive an enhanced, mathematical Vertex model to account for experimental data
- To determine the role of pulsatile RhoA in driving junction length changes
- To determine the cellular and molecular basis of junction remodeling

The manuscript was published in Developmental Cell. The contributions are as follows:

Kate Cavanaugh: Manuscript preparation, experimental data collection and data analysis.

Michael Staddon: Simulations of the vertex-based model and theoretical analysis.

Ed Munro: Review and editing the manuscript, theoretical analysis of the vertex-based model.

Shila Banerjee: Review and editing the manuscript, theoretical analysis of the vertex-based model.

Margaret Gardel: Review and editing the manuscript, supervision of work.

3.2 Abstract

Epithelial remodeling involves ratcheting behavior whereby periodic contractility produces transient changes in cell-cell contact lengths, which stabilize to produce lasting morphogenetic changes. Pulsatile RhoA activity is thought to underlie morphogenetic ratchets, but how RhoA governs transient changes in junction length, and how these changes are rectified to produce irreversible deformation, remains poorly understood. Here, we use optogenetics to characterize responses to pulsatile RhoA in model epithelium. Short RhoA pulses drive reversible junction contractions, while longer pulses produce irreversible junction length changes that saturate with prolonged pulse durations. Using an enhanced vertex model, we show this is explained by two effects: thresholded tension remodeling and continuous strain relaxation. Our model predicts that structuring RhoA into multiple pulses overcomes the saturation of contractility and confirm this experimentally. Junction remodeling also requires formin-mediated E-cadherin clustering and dynamin-dependent endocytosis. Thus, irreversible junction deformations are regulated by RhoA-mediated contractility, membrane trafficking, and adhesion receptor remodeling.

3.3 Introduction

Epithelial cell sheets dynamically remodel themselves to sculpt higher order assemblies of tissues and organs [1, 137, 138]. Individual cells execute complex shape changes to alter cell-cell junction lengths, cell surface area, and overall cell shape that, when coordinated, drive tissue morphogenesis [139, 140]. Underlying cell and tissue mechanics is the dynamic interplay of cell force generation and adhesion [1, 77, 141]. Such mechanics underlies the capability of epithelial sheets to variably maintain or dramatically change shapes during morphogenesis. To enable such varied and adaptive mechanical behaviors, the actin cytoskeleton harnesses mechanochemical feedbacks [77, 140]. The structures of these mechanochemical systems, and how they regulate cell physiological processes, remains largely unknown.

A primary regulator of cell shape changes in epithelia is the small GTPase RhoA, which acts through downstream effectors to control actomyosin assembly and contractility [109, 142]. Morphogenetic processes often involve highly dynamic RhoA activity, with pulses of active RhoA preceding the shortening of cell-cell junctions [64, 74, 143]. Transient junction contractions are incrementally stabilized to direct irreversible morphogenetic change [67, 69]. This process of transient contraction and relaxation plus incremental stabilization is commonly referred to as an oscillatory ratchet [64, 65, 144, 145]. By spatiotemporally coordinating these pulsatile contractions within and between cells, incremental changes in individual cell shapes can collectively drive large scale tissue deformations required for invagination [143, 146] or convergent extension [46, 74]. While pulsatile RhoA activity is observed in diverse contexts [57, 59, 147–149], the significance of this temporal structure and what role it may have in junctional shortening is unknown.

Adherens junction remodeling at cell-cell contacts is essential for the maintenance of cell shapes in a variety of developmental contexts [79, 141, 150]. In both the Drosophila ectoderm and amnioserosa, the Rab membrane trafficking pathway is essential in the maintenance of adherens junctions and their trafficking during morphogenesis [150]. During dorsal closure in Drosophila, tension-dependent membrane removal helps to maintain a constant junctional straightness, documenting feedbacks between junctional tension and these Rab regulators [86]. Similarly, during germband extension in Drosophila, the dynamic interplay of actomyosin contractility and Rab-dependent membrane internalization contributes to the incremental stabilization of junction contractions that underlies the oscillatory ratchet [66]. In this context, membrane tubules emanating from adherens junctions require actomyosin forces to complete vesiculation and enforce progressive junctional shortening [66]. Shear forces have also been shown to regulate junctional E-cadherin levels, whose clustering and subsequent internalization is also facilitated by formin and myosin activity during germband extension [75, 82]. These data highlight the importance of coupling between actomyosin contractility, junction tension, and membrane remodeling during junctional shortening, but the underlying

mechanisms remain unknown.

Here, we study the response to dynamic changes in junctional tension induced by optogenetic activation of RhoA in a model epithelium. We find that RhoA activation along the junction length leads to a rapid contraction that occurs primarily through the shortening of a few distinct micro-domains. For short activation times, this shortening is reversible such that junctions return to their original lengths after removal of the exogenous RhoA. However, as the activation time is increased, the extent of permanent junctional shortening is limited for a single activation pulse. To capture these data, we introduce modifications to the existing vertex-based models for epithelial tissues to include strain-dependent remodeling of junction tension and rest length. To account for our experimental data, our model must include junctional tension remodeling that occurs only above a critical junctional deformation, or strain. We show that temporally structuring the exogenous RhoA activity into distinct pulses overcomes the limited shortening, highlighting an essential role for pulsatile activation of RhoA. Finally, live cell imaging reveals that membrane remodeling and vesicular internalization occur during this RhoA-dependent junction contraction, whose stabilization at shorter lengths requires dynamin and formin activities. Altogether, these data provide new insights into the molecular and biophysical feedback mechanisms between RhoA activity and membrane remodeling that underlie junctional length changes in epithelia.

3.4 Results

3.4.1 Optogenetic activation of RhoA induces cell-cell junction shortening

To spatiotemporally control RhoA activity in model epithelia, we generated a stable Caco-2 cell line expressing the TULIP optogenetic system [108, 110, 113]. TULIPs utilize the photosensitive LOVpep domain attached to a GFP-tagged transmembrane protein, Stargazin. The LOVpep's binding partner is the prGEF complex that contains three components: a photorecruitable engineered tandem PDZ domain, the catalytic DH domain of the RhoA-

specific guanine nucleotide exchange factor (GEF) LARG, and an mCherry fluorescent tag (Fig 3.1A). Blue light increases the binding affinity of the two protein complexes, recruiting the prGEF to the membrane where it locally activates RhoA (Fig. 3.1A, B) [110, 113].

Cell morphologies and junction lengths in Caco-2 monolayers are incredibly stable; over 1 hour, the junction lengths change less than 3%. The remarkably static nature of the monolayer makes it particularly well suited to study junctional responses to acute optogenetic stimulation. Targeting light to a desired cell-cell junction (Fig. 3.1C; Cellmask, black) induces rapid prGEF (magenta) association (20 sec) and dissociation (30-50 sec) when the light is turned on and off, respectively (Fig. 3.1B,C). Consistent with previous studies, prGEF recruitment is tightly localized to the targeted region [110, 113]. The targeted junction rapidly contracts upon continuous light activation over a period of 5 min, shortening from 13.1μm to 10.3μm, and then returning to its original length once light is removed (Fig. 3.1D, E pink line).

To quantify junction contraction over time, we measured the fractional junction length $L(\mathrm{t})/L_0$, where $L(\mathrm{t})$ is junction length over time t, and $L_0 = L(\mathrm{t}{=}0)$ is the length at the activation onset at t=0. The contraction rate is measured by $(L_0\text{-}L(\mathrm{t}))/L_0$. Strikingly, we find that the rate and extent of junction shortening is remarkably consistent across junctions with varying initial lengths and geometries. During a five-minute activation, junctions consistently contract to 75-80% of their initial length at an average contraction rate of $0.047 min^{-1}$(Fig 3.1E). The fractional junction length at 5 minutes after the activation onset (L_5/L_0), or contracted length, was largely independent of initial length L_0 (Fig 3.1F). Treating monolayers with the Rho-kinase inhibitor Y-27632 completely abolished light-induced junction shortening (Fig. 3.1G), confirming that light-induced junction contraction is mediated by a downstream response to local activation of RhoA.

Junction shortening could involve uniform contraction of the entire junction or heterogeneous contraction of individual sub-junctional segments. To distinguish between these possibilities, we used variations in membrane fluorescence intensity as fiduciary markers to

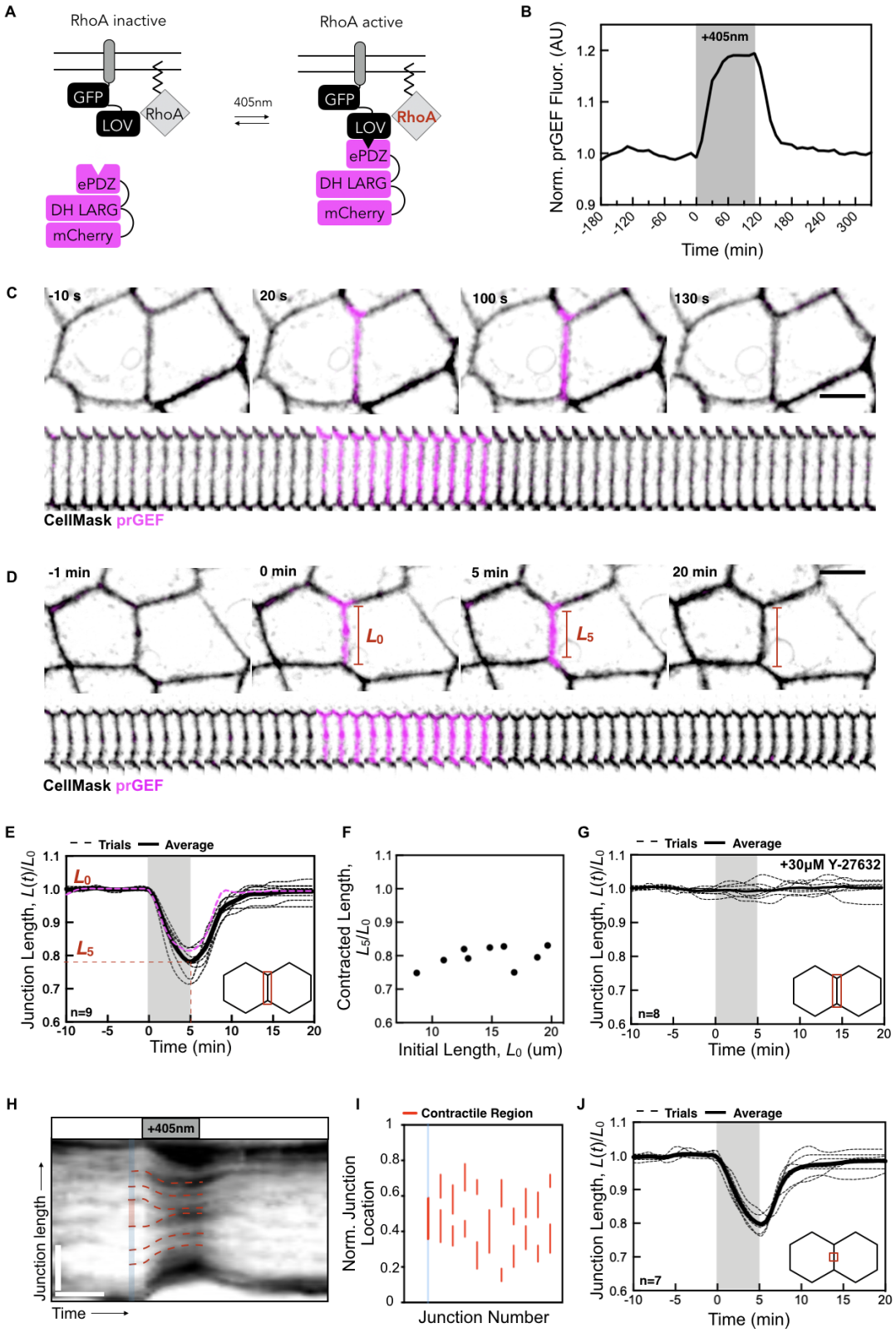

Figure 3.1: RhoA-mediated tension determines junction length at short timescales

Figure 3.1: RhoA-mediated tension determines junction length at short timescales. (Continued) A) Schematic of TULIP system. B) Intensity increase mCherry-prGEF shown in C (magenta). C) Representative images of cells undergoing junctional prGEF (magenta) recruitment. Scale bar is 10μm. D) Images of a junction undergoing a 5-min activation. Scale bar is 10μm. E) Normalized junction length over time with a 5-min activation. The magenta line represents data shown in D. F) Plot of the fractional contracted length after a 5-minute activation as a function of the initial junction length. G) Normalized junction length over time of cells treated with Y-27632. H) Representative kymograph of a junction (visualized by Cell Mask) prior to, during and after a 5-min activation. Red dashed lines denote fiduciary marks within junction. Blue region denotes the junction length; red portion indicates a region that contracts. Horizontal scale bar is 6 min, vertical scale bar is 5μm. I) The location of the contractile regions for 11 distinct junctions, indicated by a unique junction number. The junction length is normalized such that the top vertex is denoted by 1, with the bottom vertex denoted by 0. The junction in 3.1H is depicted by the blue line. J) Normalized junction length over time of junctions in a 5-min activation with light targeted only to the junction center.

examine local variations in deformation along individual junctions. Kymographs made from line scans along individual junctions, observed over time, reveal how different segments along a junction move prior to, during, and after light-mediated shortening (Fig. 3.1H). For a contraction that occurs uniformly along the junction length, we expect the speed of fiduciary marks to vary linearly from one end of the junction to the other. Strikingly, the kymograph data indicate that junctions do not contract uniformly in response to uniform activation of RhoA. Rather, we observed distinct regions that contract, indicated by converging fiduciary marks (Fig. 3.1H), red region between red dashed lines), separated by non-contractile regions, indicated by neighboring fiduciary marks that remain parallel (Fig. 3.1H, blue region).

To quantify and compare the location, size, and deformation of contracting segments in different activated junctions, we located fiduciary marks that define the endpoints of each contracting region (bottom vertex = 0, top vertex = 1) just before the onset of activation (Fig. 3.1H, red line). We then measured the initial locations and normalized lengths, divided by junction length, of contracting regions (Fig. 3.1I). We found that junctions typically contain 1-2 contracting regions with an average length of several micrometers. The average fraction of the junction that contracts in response to stimulation is 26%, and these regions contract 76% of their original length, accounting for 83% of the observed junction contraction. Plotting a

histogram of these contracting regions' lengths and localization with respect to normalized junction position reveals that contracting regions typically lie within the central portion of the junction with average normalized junctional position at 0.45 (Fig. 3.1I). Interestingly, illuminating only the central third of junctions induced contraction rates similar to those produced by full-length activation (Fig. 3.1J). These data indicate that junction contraction is largely accomplished by a few distinct contractile units that are concentrated near the centers of junctions and that are somehow predisposed to undergo rapid and complete shortening in response to uniform activation of RhoA.

3.4.2 Extent of junction contraction saturates for a single Rho activation

We exploited optogenetic control to study systematically how junction deformation depends on the duration, intensity, and location of exogenous activation. To determine how junction shortening depends on the duration of prGEF junctional localization, we varied the duration of the activation pulse from 2.5 to 40 minutes, and measured the final junction length L_f, defined to be the junction the length measured 15 minutes after the end of the pulse. For all activation periods less than 5 minutes, junction shortening is reversible with the ratio of the final length, L_f, to initial length, L_0, being equal to 1 (Fig. 3.2E). However, when we increase the activation time to 10 minutes, we observe a striking biphasic response (Fig. 3.2A). A fast-initial contraction lasting for approximately five minutes is followed by a slower contraction phase over which junction length decreases to $\sim$65% of its original length. After light removal, the junction does not return to its original length. Instead, the final junction length is $\sim$20% shorter than its initial length. We observed similar kinetics for 20-minute activations (Fig. 3.2B, C) with the slow phase showing clear saturation with a 40-minute activation time (Fig. 3.2D).

To explore how the activation time controls the extent of junction length remodeling, we measured L_f/L_0 as a function of activation time (Fig. 3.2E) and found that a rapid transition to permanent junction shortening occurs for activation times longer than 5 min.

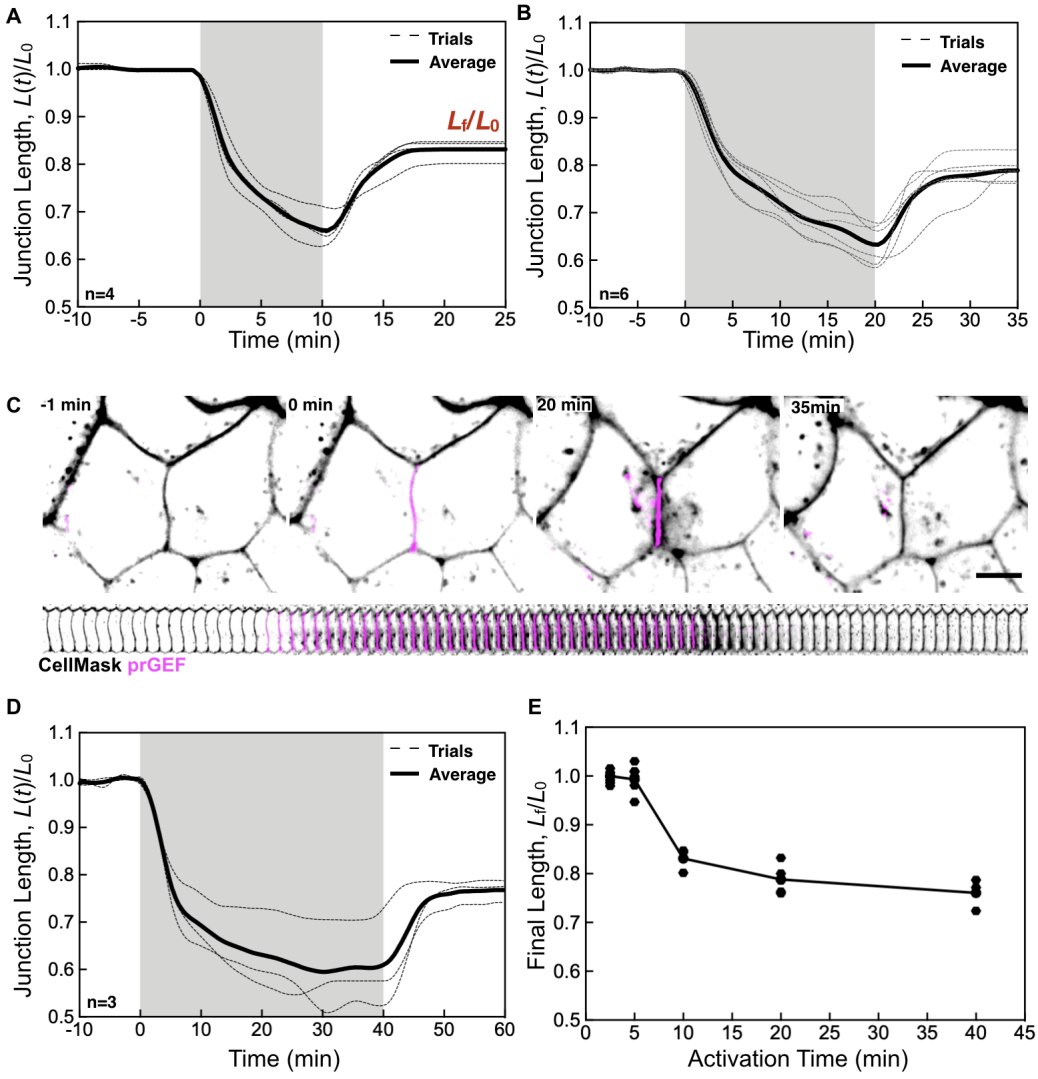

Figure 3.2: Contractility saturates at longer timescales to limit junction length changes. A) Normalized junction length over time for a 10-minute activation. B) Normalized junction length over time for a 20-minute activation. C) Representative image of a junction in a 20-minute activation. Red lines denote positions and lengths between the two junction vertices. Scale bar is 10 μm. D) Normalized junction length over time for a 40-minute activation. E) The fractional final junction length, L_f/L_0 as a function of the activation time. Data for individual junctions are shown, with line as a guide for the eye.

Furthermore, the junction shortening saturates to a 20% length reduction, even for activation times up to 40 min (Fig. 3.2E). We believe that this limited remodeling behavior is restricted to the activated junctions, as analysis of the deformations of adjacent junctions show a wide distribution of strains, including positive, negative, and no strain (Fig. 3.3). This suggests that the strain on adjacent junctions does not limit the target junctional response; instead, the contractile limit appears to arise within the activated junction. These data are consistent with only ∼26% of the junction fully contracting (Figure 3.1H, I) and raises the possibility that only a portion of the junction is remodeling upon sustained activation. Collectively these data reveal two distinct regimes of junction response to RhoA activation: reversible shortening on short timescales and irreversible shortening on longer timescales. However, the maximum extent of shortening in response to sustained activation appears to be limited.

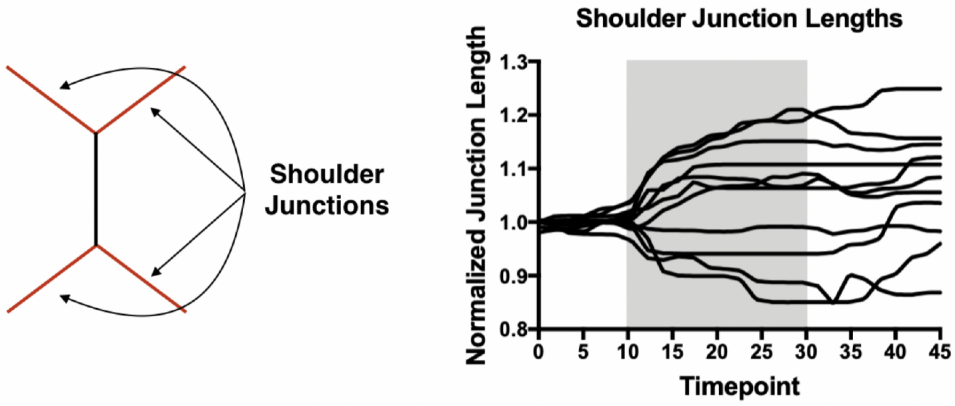

Figure 3.3: Shoulder junctions show variable strains. (left) Schematic indicating the "shoulder" junctions to the optogenetically activated central junction. (right) Measurement of Normalized junction length as a function of time during activation of the central junction. The shoulder junctions adjacent to the activated junctions show a range of length changes, including shortening, quiescence and lengthening.

3.4.3 Strain-dependent tension remodeling captures adaptive junctional length changes

To better understand the mechanistic basis for junctional length regulation in response to induced contractions, we turned to physical models of epithelial monolayers. Traditional vertex-based models represent an epithelial monolayer as a network of vertices, connected by straight junctions to form cells [90]. These models assume that junction lengths, L, are determined by the balance of two forces: junction contractility quantified by a tension Λ and elastic resistance to changes in cell area, set by an area compressibility modulus, κ (Fig. 3.5A). To model an optogenetic pulse of RhoA activation, we apply a transient step increase in junctional tension, $\Delta\Lambda$. The simple vertex model can reproduce the reversible junction shortening response that we observe for short-duration optogenetic pulses (Fig. 3.5B, solid gray). However, regardless of input pulse duration, the vertex model fails to capture the biphasic response and irreversible shortening observed for longer activations (Fig. 3.4), as do other existing variants of the vertex model [4], and other mechanical models of cell junction rheology [102, 106, 151, 152]. Thus, our experimental data are inconsistent with existing mechanical models of epithelial tissues.

In a companion theoretical study [153], we used a computational approach to explore what additional ingredients might allow vertex-based models to explain our experimental observations. In particular, we considered junctions as elastic materials that can undergo remodeling over time. For a strand of elastic material, the natural measure of deformation is the strain ϵ, defined as $\epsilon = (L\text{-}L_m)/L_m$, where L_m is the "rest length" of the material in the absence of force. In a simple elastic material, the rest length is fixed and the strain can only change through changes in material length. However, for a junction whose components (e.g. F-actin) undergo turnover, replacing strained material with new unstrained material, rest length L_m will tend to approach the current length, and the strain will tend to approach 0, a mechanism we term strain relaxation, and has been previously implemented [105]. We model strain relaxation by proposing that the junction rest length remodels at a rate proportional

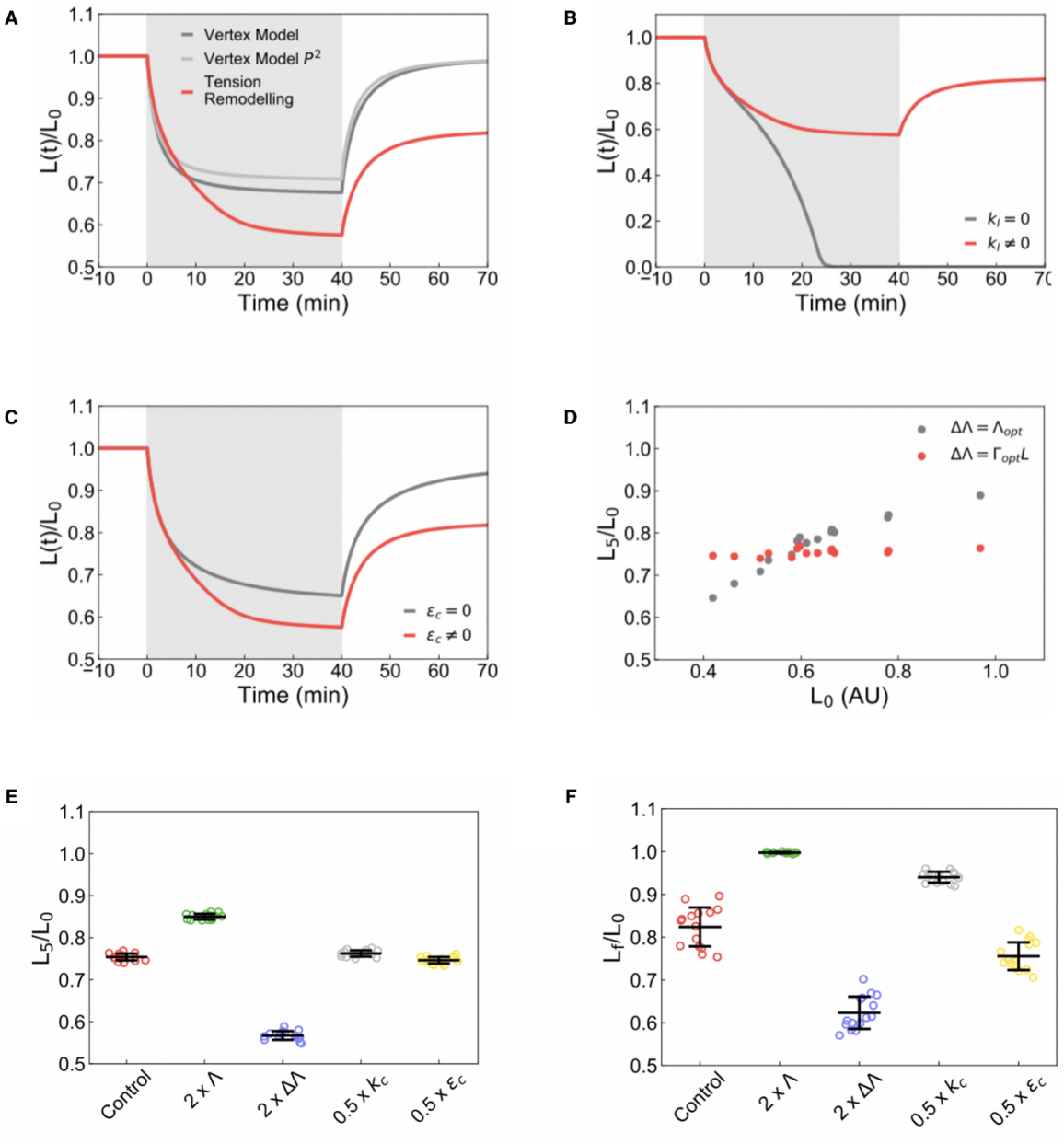

Figure 3.4: Parameters for the vertex model. A) Normalized junction length over time for a 40-minute activation using the vertex model with no tension remodeling (dark gray), vertex model including a square perimeter term in the energy (light gray), and vertex model with tension remodeling (red). B) Normalized junction length over time for a 40-minute activation with (red) and without (gray) rest length remodeling. C) Normalized junction length over time for a 40-minute activation with (red) and without (gray) a critical strain. D) Normalized junction length after a 5-min activation versus the initial junction length using a constant applied tension (gray) and an applied tension proportional to the junction length (red). E) Initial junction contraction is modulated by changes to base junctional tension or applied tension, while being robust to changes in other mechanical parameters. F) Final normalized length as a function of different parameter perturbations.

to the junction strain (Fig. 3.5C, black solid line). Second, we introduced the concept of strain-dependent tension remodeling, where junction tension undergoes a permanent change only when strain crosses a critical magnitude, ϵ_c, at a rate proportional to the strain (Fig 3.5C, green dashed line). We refer to vertex model incorporating strain relaxation and strain-dependent tension remodeling as an enhanced vertex model.

Strikingly, we found that using a single set of model parameters (Fig. 3.5A,B; Fig. 3.4), the enhanced vertex model reproduces experimental data for the junction length as a function of time, over a wide range of activation periods (2.5-40 min), including the changes in the final junction lengths as a function of activation time (Fig. 3.5B,E). The underlying mechanism can be understood as follows: For a short optogenetic pulse, the critical strain threshold is not reached, junctional tension remains constant, and the junction length recovers to its original value. However, for longer pulses, and for sufficiently strong $\Delta\Lambda$, junctional strain crosses the critical threshold, and tension remodeling results in a permanent increase in junctional tension and a permanent shortening of junction length (Fig. 3.5B red and black lines, D; see [153] for further details).

A key assumption of the enhanced vertex model is that deformation beyond a critical strain is necessary to initiate junctional tension remodeling to enable irreversible shortening. To test this assumption, we reduced the initial contraction amount by reducing the prGEF recruitment, controlled by the light intensity (Fig. 3.5F). When the light intensity is 1000AU, the average junction shortens by 20-25% of its original length after 5 minutes, with an average contracted length, L_5/L_0, equal to 0.77 (Fig. 3.5F). Reducing the activation light intensity by 25% (750 AU) and 50% (500AU), reduced the amount of initial contracted length, increasing L_5/L_0 to 0.81 and 0.89, respectively (Fig. 3.5F). When $L_5/L_0 < 0.8$, we find that the final length, L_f/L_0, is proportional to the amount of initial contraction (Fig. 3.5H). However, when the initial contraction is less than 20% ($L_5/L_0 > 0.8$), we find that no junctional shortening occurs ($L_f/L_0 \approx 1$) (Fig 3.5G,H). These experimental results agree remarkably well with those predicted by the model when $\Delta\Lambda$ is varied to modify the initial

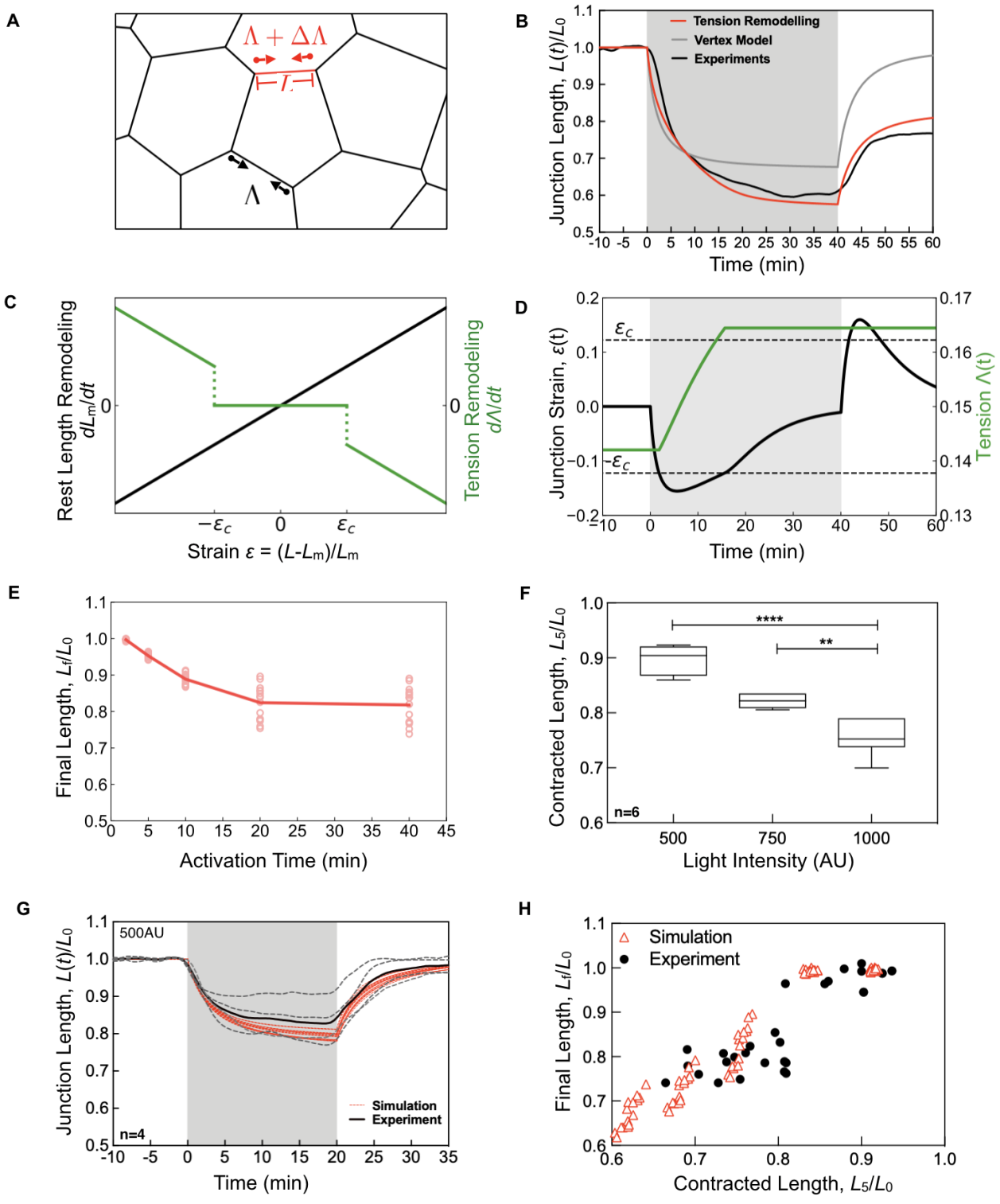

Figure 3.5: Enhanced Vertex Model for mechanosensitive junction remodeling

Figure 3.5: Enhanced Vertex Model for mechanosensitive junction remodeling. (Continued) A) Schematic of the vertex model. Cell edges (black lines) are characterized by a length, L, and contractile tension, Λ. During an optogenetic activation, the red edge has an increased line tension, characterized by a $\Delta\Lambda$. B) Normalized junction length over time for a 40-minute activation, using the vertex model without (gray) and with (red) tension remodeling, as compared to experimental data (black). C) Rest length remodeling rate (left, black) and tension remodeling rate (right, green) as a function of junctional deformation, or strain. D) The junction strain and tension over time during 40-minute activation corresponding to B. E) Final normalized junction length as a function activation time determined from simulations. F) The fractional contracted junction length for a 5-minute activation for varying light intensity determined experimentally for n=6 junctions. Boxes indicate S.D.; whiskers are min/max; **=p<0.05; ****=p>0.0001. G) Normalized junction length over time for reduced light intensity (500 AU) (black dashed lights). Simulation results obtained with $\Delta\Lambda$ reduced two-fold (red lines). H) Final normalized junction length as a function of the contracted length after 5-minutes of activation, L_5/L_0. Experimental data (black circles) is pooled from experiments of varying light intensity and duration; Simulation data (open red triangles) is pooled from simulations with varying duration and magnitude of $\Delta\Lambda$.

contraction (Fig. 3.5G,H). Together these findings demonstrate that a mechanosensitive junctional remodeling pathway, involving strain-dependent tension remodeling, stabilizes junction lengths in response to a temporal pulse of RhoA activity.

3.4.4 A Pulsatile Pattern of RhoA Activation Allows Multiple Rounds of Junctional Ratcheting

Our experimental and modeling data show that junction shortening in response to a single prolonged pulse of RhoA activity saturates at a ∼20% reduction, even for longer activation times (Fig. 3.5E). In the enhanced vertex model, this saturation arises because strain relaxation opposes the effects of tension remodeling to stabilize junction length (Fig. 3.5C). For a step increase in applied tension $\Delta\Lambda$ that drives the junction strain below the threshold -ϵ_c (Fig. 3.5C), the junction tension remodels until strain relaxation causes junctional strain again to rise above -ϵ_c (Fig. 3.5D). Thus, for a single activation, junctional shortening is limited by the amount of tension remodeling that occurs during the initial phase of rapid contraction. Moreover, following termination of a single pulse, the rapid increase in junction length induces a rapid increase in positive strain that subsequently relaxes over time (Fig

3.5D), defining an interval in which the junction is refractory to further input.

These simulation results suggest that temporally separated activation pulses can overcome the limit on irreversible junction shortening observed in response to a single pulse, provided the time between pulses is sufficiently long to relax the residual positive strain. To explore this possibility, we perform simulations with two activation pulses, with identical strength $\Delta\Lambda$ and durations $\frac{1}{2}t_{act}$ separated by varying amounts of "rest" time t_{rest} (Fig. 3.6A). During this rest period, the tension removal results in junction length extension (Fig. 4A) and increased strain that relaxes over time (Fig. 3.6B). Consequently, the second exogeneous tension pulse results in a sufficient contractile strain to drive a second period of tension remodeling (Fig. 3.6B). The extent of tension remodeling that occurs in the second pulse depends on the residual strain ϵ_r that remains at the end of the relaxation time (Fig. 3.6C). Consequently, the amount of additional length contraction that occurs between the second and first pulse (Fig. 3.6A) is proportional to ϵ_r (Fig. 3.6C).

We then examined how the junction shortening varies when the total activation time, tact, is temporally sculpted into two shorter pulses, of duration $\frac{1}{2}t_{act}$, separated by a rest time, t_{rest}, (Fig. 3.6A). When the rest time is short, the final junction length is limited to 80% of the initial value for all activation times longer than 15 minutes and rest time ranging from 0 to 10-15 minutes (Fig. 3.6D). However, for longer rest times, temporally structuring the contraction into two distinct pulses enables further junction shortening for the same activation time (Fig. 3.7). For instance, for a constant tact of 25 minutes, increasing the rest time from 15 minutes to 40 minutes decreases the final normalized length from 0.80 to 0.60 (Fig. 3.6D). Thus, our model for mechanosensitive kinetics of junction remodeling predicts that frequency modulation of Rho GTPase activity will have a significant impact on junction shortening.

To test these predictions, we modify the temporal pattern of exogenous RhoA activation and compared the total length change induced by a single 40-minute light activation to that of two 20-minute pulses separated by either 10 minutes or 20 minutes rest. As described

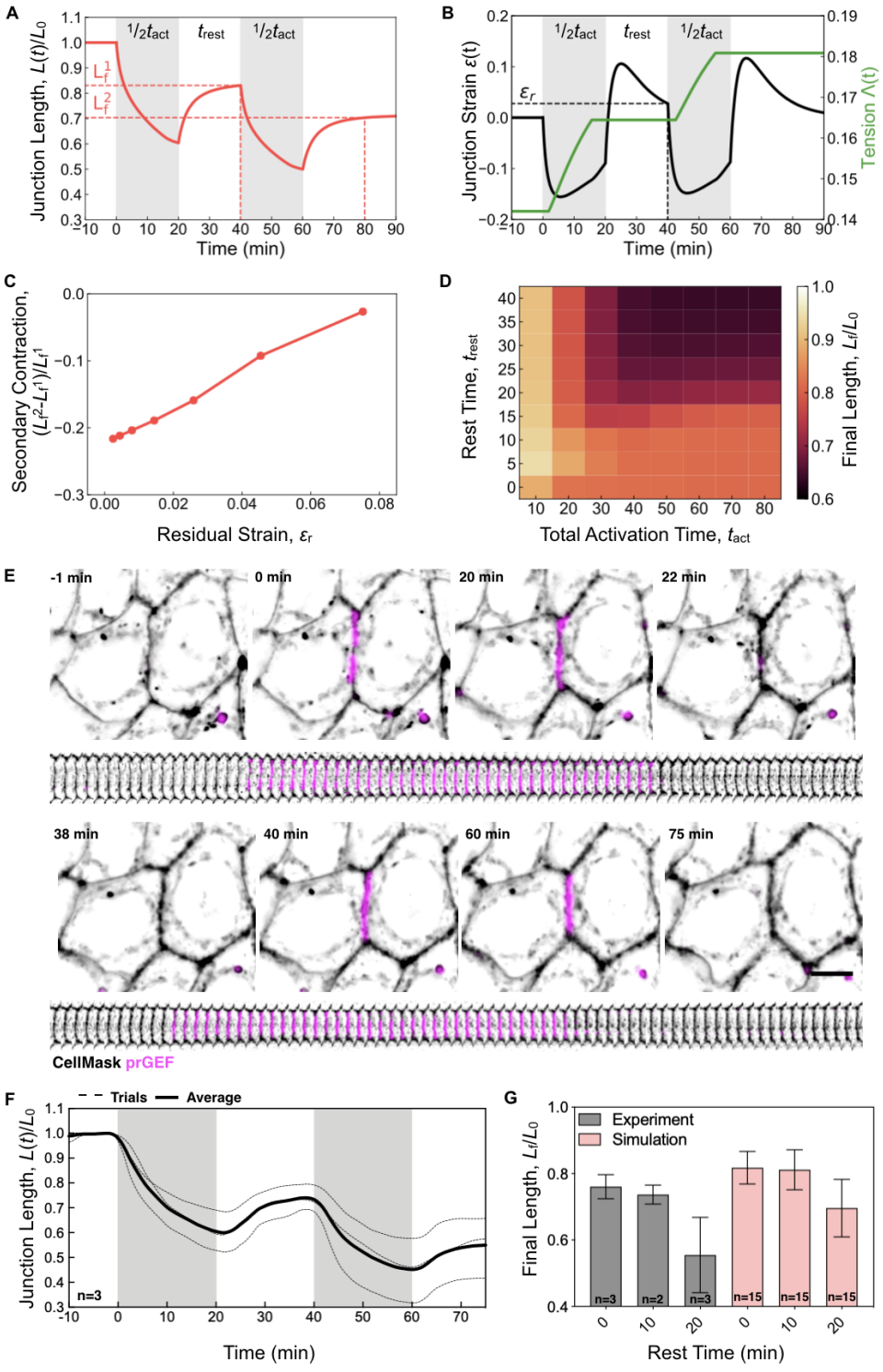

Figure 3.6: Pulsatile RhoA Enables Junctional Ratcheting

Figure 3.6: Pulsatile RhoA Enables Junctional Ratcheting. (Continued) A-B) Normalized junction length (A), and junction strain (B, left, black) and tension (B, right, green), during two 20-minute activations with a 20-minute rest period, t_{rest}. The residual strain, ϵ_r, is the junction strain at the end of the rest period. C) The average additional contraction that occurs after the second pulse as a function of residual strain obtained from n=15 simulations. D) Final junction length (heat scale) as a function of rest time and total activation time, for pulsed activation scheme in A+B. E-F) Representative image (E) and normalized junction length over time (F) of a junction in an experiment with a two 20-minute activation with a 20-minute rest period. Scale bar is 10μm. G) Final normalized junction length for varying rest times in experiments (grey, n=2 or 3) and simulations (pink, n=15 for each condition). Error bars indicate standard deviation of the number of experiments/simulations indicated within each bar.

previously, a single 40-minute pulse shortens the junction length by 20%. Dual pulses separated by <10 minutes induce a similar extent of contraction (Fig. 3.6G, Fig. 3.7). However, when the rest time is increased to 20 minutes, the junction shortens to 40-50% of the original length (Fig 3.6E-G), in agreement with our model predictions.

3.4.5 RhoA-induced junction contraction initiates membrane coalescence and internalization

To gain insight into the cell biological mechanisms underlying junctional tension and length remodeling, we examine changes in the cell membrane that occur during Rho-mediated junctional shortening. We measure membrane intensity profiles perpendicular to the junction, averaged along the junction length at several times, t=0, 5 and 20 min, during activation (Fig 3.8A). Initially, the line scans reveal a narrow intensity profile of the membrane, with a full-width at half max of 0.75μm (Fig. 3.8B,C) that reflect membrane localization at the cell-cell interface. During stimulated junction contraction, both the peak and width of the membrane intensity profile increases (Fig. 3.8B,C), reflecting the accumulation and coalescence of membrane during contraction. To measure the change in membrane intensity proximal to the activated junction, we measure the average intensity in a region a distance 1.5μm away from the peak intensity and observe a dramatic increase during both the fast and slow contraction phases (Fig. 3.8D). Close examination of these regions reveals vesicles

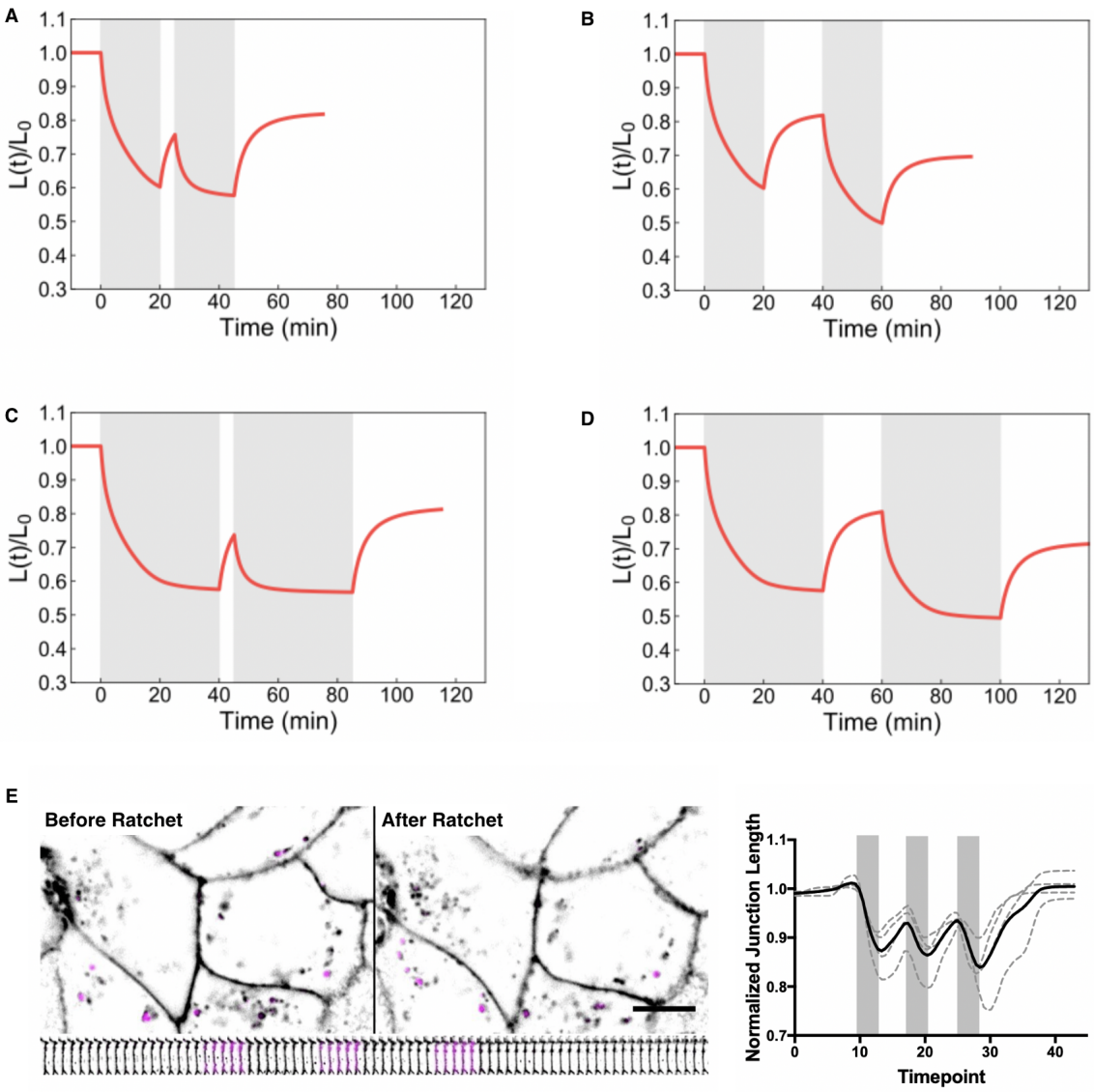

Figure 3.7: Modifications to t_{act} and t_{rest} adjust the junctional ratchet. Normalized junction length over time for (A) two 20-minute activations with a 5-minute rest, (B) two 20-minute activations with a 20-minute rest, (C) two 40-minute activations with a 5-minute rest, and (D) two 40-minute activations with a 20-minute rest. (E) Optogenetic activation comprised of three 2.5 minute activations separated by 2 5-minute rest periods. (left) images of the junction prior to and after activation scheme. (right) junction length as a function of time over the optogenetic experiment.

emanating from the junction during the slow contractile phase of activation (Fig. 3.8E, red arrow). Notably, we see these vesicles emanating from concentrated membrane regions that span a few microns along the junction proper (Fig. 3.8E, yellow arrows), similar in size to the regions that undergo local contraction (Fig. 3.1H,I).

To further interrogate the relationship between changes in junction length and membrane internalization, we developed an assay to monitor the response of cell sheets to a uniform increase in RhoA activity induced by washing out its inhibitor, C3 transferase. Our goal with this washout assay was to examine the tissue-level response to acute RhoA activation, recapitulating our optogenetic activations. In control conditions, time-lapse imaging of monolayers expressing a Stargazin-Halo membrane marker show little cellular movement over the course of two hours (Fig 3.8F). We quantify cell shape using a dimensionless shape parameter, defined as the ratio of the cell perimeter to the square root of the cell area [98]. This shape parameter is a reliable measure of junction perimeters and cell shapes in response to varying cortical tension. In control conditions, the shape parameter is 3.9, indicating a compact, hexagonal shape (Fig 3.8G), and the average number of fluorescently labeled vesicles per cell remains low (<4) over two hours, consistent with a low rate of membrane internalization during this time (Fig 3.8H).

To globally inhibit Rho activity, we incubated the monolayers in media containing C3 transferase for four hours (Fig. 3.8F). Rho inhibitor treatment induces an increase in the cell shape parameter to 4.5, reflecting a more elongated shape and induces increased cell motion (Fig. 3.8G). The mean number of vesicles per cells remained low (~ 2) over 2 hours (Fig 3.8H). Thus, global RhoA inhibition induces changes in overall cell shape, and increases junction length, but does not modify the amount of membrane internalization that occurs over several hours.

To explore how a global increase in Rho activity modulates cell shape and surface membrane reorganization, we visualize changes in cell shape upon washing out C3 transferase (Fig 3.8F). After C3 transferase washout, the cell shape parameter decreased from 4.3 to 3.9,

consistent with the increased contractility driving the transition from a more elongated to hexagonal shape with decreased perimeter and therefore junction lengths (Fig 3.8G). Strikingly, this change in junction length is accompanied by significant increase in cytoplasmic vesicles, increasing to a mean of 10-19 vesicles per cell two hours after C3 washout (Fig 3.8F, H). Thus, we observe a significant increase in internalized membrane that occurs during Rho-mediated changes in junction length. Consistent with our optogenetic data, increased RhoA activity causes a decrease in junction length and induces vesicle internalization and membrane remodeling response.

To further examine RhoA-mediated membrane remodeling, we generate mosaic monolayers of cell lines expressing spectrally distinct membrane tags, Stargazin-Halo:Janelia-646 and Stargazin-GFP (Fig. 3.8J). This mosaic labeling allows us to determine which cells contribute membrane during individual internalization events. The internalized vesicles within a given cell 2 hours after C3 washout have the same fluorescence as that of the cell's plasma membrane, indicating that during junction shortening, cells internalize their own membranes, but not that of their neighbors. (Fig. 3.8I). When we examine junctions between differently-labelled cells at high resolution, we could resolve a heterogeneous distribution of labeled membranes, characterized by patchy variation in both label's intensities along the junction's length (Fig. 3.8J). Kymographs of junctions during RhoA-mediated shortening show that this patchy distribution of membrane labels persists but varies over time (Fig. 3.8K). This indicates that, along the adherens junction, membrane materials from the two cells disappear abruptly and asynchronously over time. Examining regions proximal to the adherens junction at these time points reveals that membrane internalization occurs via extended, tubule-like structures from concentrated membranous regions (Fig. 3.8L, yellow arrows), consistent with our optogenetic data (Fig. 3.8E). Together, these data indicate that during Rho-mediated junction shortening, membrane at the adherens junction remodels and is internalized within micrometer-sized domains.

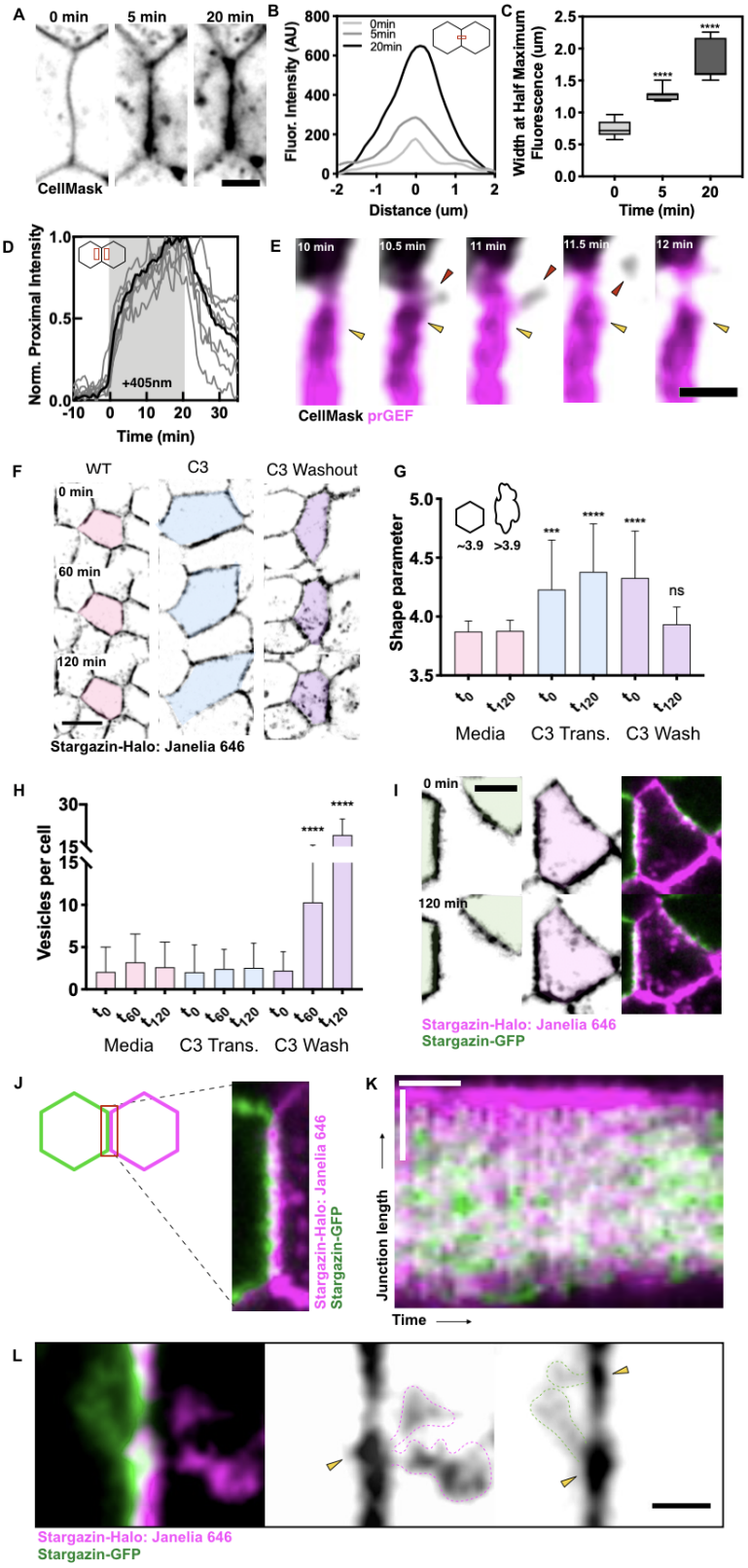

Figure 3.8: Compressive strain induces the remodeling of slackened membrane

Figure 3.8: Compressive strain induces the remodeling of slackened membrane. (Continued) A) Representative images of a junction at t=0, 5 and 20 minutes after activation. Scale bar is 5μm. B) Cell Mask intensities along a line perpendicular to the at times in (A). CC The full width at half maximum fluorescence from data in (B). Each box is average of n=8 regions, ****=p<0.0001 compared to t=0 data. D) Normalized fluorescence intensity for region proximal to the activated junction during an optogenetic experiment. Data for 8 regions is shown, with average indicated by bold line. E) Representative image of a junction between 10-12 minutes after activation showing membrane vesiculation and internalization. Scale bar is 2μm. F) Stargazin images at 0, 60, and 120 minutes of wild type cells, with C3 transferase treatment, or immediately after a C3 transferase wash out at t=0 min. Scale bar is 10μm. G) Quantification of cell shape parameters from F) Each bar is the average/SD of n=30 cells for each condition. H) The number of vesicles observed within cell interior in images from F. Each bar is the average/SD of n=30 cells for each condition. I) Representative images of a mosaically labelled cell (pink) undergoing self-internalization from 0 to 120 minutes. J) Representative image of a mosaically labelled cell-cell junction showing heterogeneous distribution of membrane. K) Kymograph of junction undergoing shortening in I shows distinct membrane regions appearing during contraction. Horizontal scale bar is 20 minutes, vertical scale bar is 5μm. L) Representative image showing tubular vesicles emanating from membrane regions during junction contraction. Scale bar is 2μm.

3.4.6 Permanent junction shortening requires formin-dependent clustering and dynamin-mediated endocytosis of E-cadherin.

During morphogenic processes in Drosophila development, adherens junction remodeling is mediated by the internalization of junctional components, including E-cadherin [75]. We therefore sought to determine the relationship between RhoA-mediated membrane remodeling and junctional components. To determine how E-cadherin puncta are impacted by optogenetic RhoA activation, we visualize E-cadherin in live cells by incubation with fluorescent conjugates of HECD1 antibody to preserve trans-cadherin interactions while labeling endogenous E-cadherins [154]. Notably, this labeling reveals a punctate pattern of E-cadherin along cell junctions (Fig. 3.9A, B), and this treatment did not induce any junction length changes or endocytic events prior to light activation and optogenetically-induced junction contraction was similar to control cells. Consistent with the heterogenous shortening of junction segments, we observe heterogeneity in the remodeling of E-Cadherin, involving local events in which groups of E-cadherin puncta at the center of the junction coalesce together, intensify, and are

then are internalized within the slow remodeling phase of RhoA stimulation (Fig. 3.9A yellow arrows). Thus, internalization of E-cadherin clusters occurs during junctional shortening triggered by optogenetic activation of RhoA.

We next sought to elucidate the molecular regulation of observed membrane remodeling and internalization. Immunolocalized E-cadherin exists as distinct puncta along lateral junctions of epithelial monolayers (Fig. 3.9B, yellow arrows). Consistent with previous work [75], we find this clustering is formin-dependent, as treatment with the pan-formin inhibitor SMIFH2 abolishes E-cadherin punctae (Fig. 3.9B). To test if formin-mediated E-cadherin clustering is important for junction remodeling in response to optogenetic activation of RhoA, we treat monolayers with SMIFH2 and stimulate the junction for 20 minutes (Fig. 3.9C, D). SMIFH2 treatment has no impact on the initial junction contraction relative to controls (Fig 3.9D, G). However, in contrast to controls, upon removal of light, SMIFH2-treated junctions return to their original length and no permanent length reduction is observed (Fig. 3.9D, G).

If internalization of E-cadherin clusters by endocytosis is important for junction remodeling, then blocking vesicle internalization should also prevent irreversible changes in junction length in response to optogenetic activation of RhoA. To test this prediction, we treat monolayers with Dynasore, a pharmacological inhibitor of dynamin-mediated vesicle scission [155]. Indeed, treating monolayers with Dynasore does not alter the initial contractile phase in response to optogenetic activation of RhoA (Fig 3.9E, F, G), but the slower remodeling is abolished, and junctions return to their original lengths following the end of an activation (Fig 3.9F,G). Thus, dynamin is required for junctional remodeling. Together, these data suggest that the permanent junction shortening that occurs after a pulse of increased RhoA activity requires formin-mediated E-cadherin clustering and dynamin-mediated endocytosis (Fig. 3.9H).

3.5 Discussion

In this study, we utilized optogenetics to investigate how transient activation of RhoA can induce longer lasting irreversible changes in cell shape in model epithelia. Exploiting

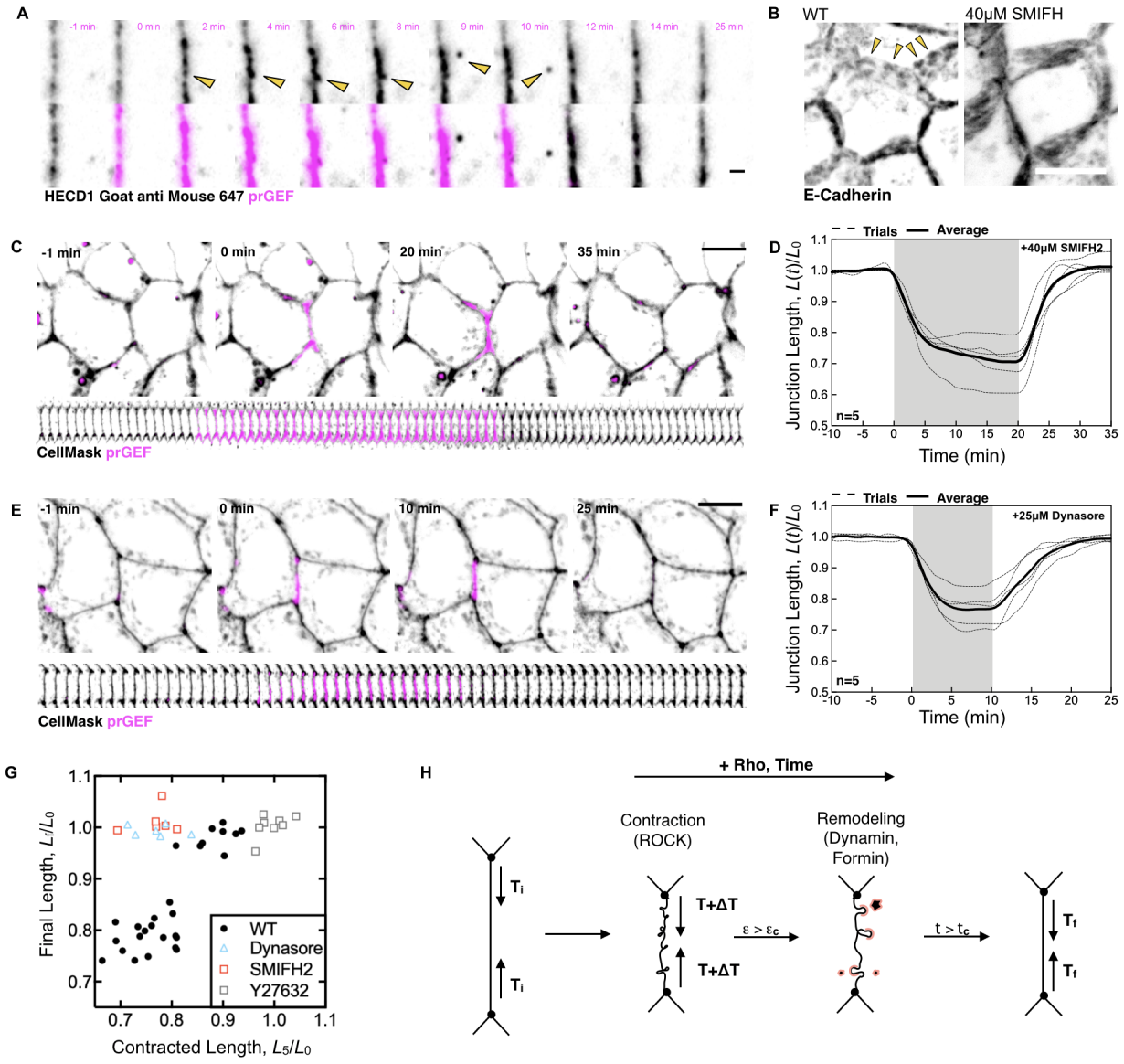

Figure 3.9: Endocytosis of Formin-mediated E-cadherin clusters is necessary for length changes. A) Image of cells treated with primary and secondary antibodies. Scale bar is 2μm. B) Z-stack projection of a cell stained for E-cadherin and a z-stack projection of a cell treated with SMIFH2 and stained for E-cadherin. Scale bar is 10μm. Arrows indicate regions of E-cadherin rich junctional puncta. C) Images of SMIFH2 treated cells. Scale bar is 10μm. D) The normalized junction lengths over time in SMIFH treated cells from C for n=5 junctions. E) Representative images of cells treated with Dynasore and undergoing a 10-minute activation. Scale bar is 10μm. F) Quantification of normalized junction length over time in Dynasore treated cells from E for n=5 junctions. G) The final junction length as a function of the initial contracted length for perturbations. H) Summary of the junction remodeling. The initial tension of a junction is T_i. A stepwise increase in tension, ΔT drives contraction. If the junction is deformed above the critical strain, $\Delta\Lambda > \epsilon_c$, dynamin and formin-dependent junction remodeling. After sufficient time, the junction remodels to a new length with a new base tension, T_f.

optogenetic control, we identified how changes in the strength and temporal structure of RhoA activation can access qualitatively different regimes of junctional remodeling. We find that small changes in junction length are completely reversible. In contrast, sufficiently strong or prolonged activation of RhoA can drive junctions across a deformation threshold to trigger junctional tension remodeling that drives irreversible junction shortening. Furthermore, episodic pulses of RhoA activity, separated by periods of quiescence, can induce a greater degree of irreversible change than a prolonged pulse of the same strength. These results provide a basis for understanding how the strength and pattern of RhoA activity can encode fine-tuned instructions for epithelial morphogenesis.

Our data have significant implications for the use of simple vertex models to describe morphogenetic remodeling of epithelial tissues [4, 102, 106, 151]. In traditional vertex models, junction lengths evolve solely in response to junction tension and cell elasticity. These models and their existing variants capture reversible changes in junction length in response to small contractions, but they are inadequate to describe the time-dependent junction shortening dynamics we observe in response to sustained or multiple pulses of RhoA activation. To describe these responses, we find that it is necessary and sufficient to consider two additional properties: continuous relaxation of junctional strain, and local remodeling of active junction tension above a critical strain threshold (see also [94]). Threshold-dependent remodeling of active tension encodes the trigger for irreversible deformation. Continuous relaxation of junction strain sets a limit on the amount of irreversible deformation produced by a single pulse of activation and sets the timescale on which the system is refractory to further input, allowing for frequency-dependent modulation of morphogenetic change. This combination of strain threshold and frequency dependence provides a way to balance dual requirements for epithelial tissue homeostasis and large-scale remodeling. A strain threshold maintains architectural homeostasis against small fluctuations in contractile activity, while higher amplitude patterned activity can direct major morphogenetic movements in epithelial tissues.

The exact mechanisms underlying junctional strain relaxation remain unknown. However,

the tendency to relax internal strain is a property of any material whose load-bearing elements undergo turnover in such a way as to replace strained elements with new unstrained elements. For example, turnover of actin filaments is thought to underlie strain relaxation in cortical actin networks, endowing those networks with effectively viscous behaviors [156, 157]. At the filament scale, mechanical strains accelerate severing and turnover of F-actin [158], providing a putative force-sensitive fluidization of actin networks. In addition, turnover of structural elements of adherens and/or tight junctions, through exocytosis/endocytosis or other mechanisms, may also contribute to strain relaxation [77]. Strain relaxation in epithelial junctions could arise from mechanosensitive mechanisms either within the actin cortex itself or via turnover of adherens and/or other junctional adhesions. Understanding the mechanisms that govern and tune junctional remodeling to account for both length changes and strain relaxation will be an important target for future work.

Our experiments strongly support the idea that junctional tension remodeling is strain-thresholded. However, the origins of this strain threshold, and the mechanisms underlying changes in local junctional tension, remain unclear. Because there is no clear relationship between the strains on activated junctions and neighboring junctions during the response to activation (3.3), we think it likely that the mechanism for strain-dependent tension remodeling is intrinsic to individual junctions. Our observations highlight a few key features of junction contraction induced by exogenous RhoA activation. First, contraction is heterogeneous, mediated by a few contractile regions, occupying ∼26% of the junction' length, that shorten rapidly and completely during exogenous RhoA activation (Figs 3.1, 3.8J,K, 3.9A). Second, contraction of these regions appears to be sufficient to account for the extent of fast junction contraction (∼20%) and the expected strain threshold (∼20%) to triggering tension remodeling. Third, contraction is associated with local accumulation of membrane within contractile regions, consistent with local membrane buckling (Fig. 3.9H). Fourth, local clustering and coalescence of E-cadherin puncta also occur during contraction (Fig. 3.9A). Finally, local endocytosis of junctional membrane, E-cadherin, and other junctional components correlates

with, and is critical for, irreversible junctional shortening driven by super-threshold pulses of RhoA activity.

This model is in line with recent work documenting roles for the Rab trafficking pathway in promoting irreversible changes in junction length during epithelial morphogenesis [66, 75, 86, 150, 159]. Internalization of slackened membrane has been described during dorsal closure [86] and germ band elongation [66] in Drosophila embryos. Thus, our and other data point towards a more general model in which strain induces membrane buckles that either initiate or control the rate of endocytosis to control junction length (Fig. 3.9H). In principle, such mechanisms could act either to stabilize cell shapes or promote irreversible change in cell shape, depending upon the nature of feedback in the system. Indeed, it will be of interest to explore any feedback mechanisms between RhoA and the general endocytic machinery. Already it has been shown that Dia signaling, downstream of RhoGEF2, can induce ectopic clathrin recruitment at junctions [75].

The possibility that local clustering, coalescence, and internalization of E-cadherin could play a role in junction remodeling is consistent with recent work reporting how differences in the subcellular origin of contractile forces affects junctional E-cadherin endocytosis [82]. Polarized junctional NMII generates shear stress that destabilizes and dissociates E-cadherin trans-interactions for their subsequent internalization via heterogeneous load distribution [82]. Our data similarly document punctate patterns of local E-cadherins that heterogeneously contract upon RhoA activation (Fig. 3.9A). Formin activity is required for the formation and coalescence of these puncta. Thus formin-mediated actin assembly and E-cadherin clustering may help to organize the distinct contractile units that drive heterogenous junction contraction, In addition, coalescence of E-cadherin puncta may help to stabilize regions of slackened membrane which act as endocytic hubs, and assist in packaging buckled regions of membrane/cortex for dynamin-mediated internalization. It will be of interest to further dissect the molecular basis of this formin-mediated E-cadherin endocytosis.

Cells in developmental systems are tuned to undergo dynamic processes such as inter-

calation events and undergo fast contractions to reach what we propose to be a threshold strain. In vivo, junctions contract at a strain rate of $0.5min^{-1}$ [64] with cycles of pulsatility being significantly shorter. Here, junction contractions range from 90-120 seconds and rest periods range from 2-7 minutes [64, 66]. We do not produce any significant length changes post activation when using optogenetic activation schemes that are more characteristic of developmental systems (Fig. S3E). We also find that the Caco-2 junction contraction rate ($0.047min^{-1}$) is slower than developing tissues. This difference in tissue deformability may arise from sub-cellular or tissue-scale effects. For instance, in vivo, multiple junctions are shrinking in the face of tension [67]. Neighboring pulses also occur in antiphase with junctional contractions; such an oscillatory contractile structure may further shorten the junctions or stabilize cell shapes [160]. Additionally, our system lacks any basolateral protrusions that coordinate with apicojunctional vertex formation to facilitate tissue fluidity [161]. Despite these differences, our simplified system and approach present a means to isolate how temporal regulation of junctional Rho activity sculpts junctional length and provide insights into in vivo junctional ratcheting.

3.6 Methods

Plasmids and Generation of Cell lines: Lentiviral vectors described here were generated with the aid of SnapGene Software (GSL Biotech LLC). The optogenetic membrane tether consisting of Stargazin-GFP-LOVpep and prGEF constructs were constructed by PCR amplification of the region of interest and inserting it into a lentiviral vector, pWPT-GFP (12255; Addgene) using restriction sites BamHI and SalI. This created the lentiviral constructs WPT-Stargazin-GFP-LOVpep and WPT-mCherry-prGEF. pWPT-Stargazin-Halo was constructed by inserted a PCR amplified a Halo tag region into the the pWPT-Stargazin-GFP-LOVpep backbone isolated by PCR amplification.

Lentivirus was produced using 293T cells (a gift from G. Green, University of Chicago, Chicago, IL) using Fugene 6 transfection reagent (Promega) to transfect the lentiviral

vectors, a pHR1-8.2-delta-R packaging plasmid, and VSV-G pseudo typing plasmid (gifts from M. Rosner, University of Chicago, Chicago, IL). Viral supernatant was collected, filtered, and incubated with target Caco-2 cells for 24hr in the presence of 8ug/ml polybrene (EMD Millipore). After viral transfection, cells were sorted by fluorescence (UChicago Flow Cytometry Core) and screened for optimal expression of constructs by fluorescence microscopy.

Collagen gel preparation: Collagen gels were prepared by mixing Rat tail collagen 1 (Corning) with collagen polymerizing reagents to a final concentration of 2mg/ml. Collagen polymerizing agents were prepared with media mixed with 1M Hepes and 7.5% NaHCO3 for a final ratio of 1:50 and 1:23.5, respectively. Four-well chambers (Ibidi) were coated with 30ul of 2mg/ml collagen solution and polymerized in the incubator for 10min before plating cells.

Microscopy: Cells were imaged on an inverted Nikon Ti-E (Nikon, Melville, NY) with a Yokogawa CSU-X confocal scanning head (Yokogawa Electric, Tokyo, Japan) and laser merge model with 491, 561, and 642nm laser lines (Spectral Applied Research, Ontario, Canada). Images were collected on a Zyla 4.2 sCMOS Camera (Andor, Belfast, UK). Optogenetic recruitment utilized a Mosaic digital micromirror device (Andor) coupled to a 405nm laser. A 60x 1.49 NA ApoTIRF oil immersion objective (Nikon) or a 60x 1.2 Plan Apo water (Nikon) objective was used to collect images. MetaMorph Automation and Image Analysis Software (Molecular Devices, Sunnvyale, CA) controlled all hardware.

Live-cell imaging: To ensure a mature and polarized epithelial monolayer, Caco-2 cells were plated at a confluent density on a collagen gel within an Ibidi chamber and cultured for two days prior to any experiments. Ibidi chambers were then placed in culture media supplemented with 10mM Hepes and maintained at 37oC or maintained with a stage incubator for temperature, humidity, and CO2 control (Chamlide TC and FC-5N; Quorum Technologies). For the stage incubator, the stage adapter, stage cover, and objective were maintained at 37C, whereas humidified 5% CO2 was maintained at 50C at its source to prevent condensation within its tubing.

For optogenetic experiments, cell-cell junctions were labeled with CellMask Deep Red

plasma membrane stain (Molecular Probes, Life Technologies). Cells were imaged in the 561 and 647 channel every 35 seconds. The first 10min was used document average junction length fluctuations and the last 15 minutes to document junction recovery. For analysis of the timescales of RhoA activation, the activation period was 2.5, 5, 10, 20, or 40 minutes. During the stated activation period, a local region was drawn around the cell-cell junction in MetaMorph and illuminated by the 405nm laser for 1000ms immediately before the acquisition of each image. Activated regions were adjusted in real time to isolate the prGEF at contracting junctions. Unless otherwise stated, laser power was set at 1000AU. For determining junction strain rates as a function of laser intensity analysis, laser power was reduced to 750 or 500AU.

Mosaic labeling of cells was performed by mixing the two cell lines, Stargazin-Halo and Stargazin-GFP, at least a day before imaging and grown to ensure a confluent and polarized monolayer. For visualization, Stargazin-Halo cells were conjugated with the Halo ligand, JaneliaFluor 646 (a kind gift from Luke Lavis, HHMI Janelia Research Campus, Ashburn, VA).

Drug treatments: For optogenetic experiments, cells were treated with stated drug for at least one hour before any optogenetic activations and imaging. Treatments here were 30uM Y-27632 (Sigma), 25uM Dynasore (Tocris), 40uM SMIFH2 (a gift from D. Kovar, University of Chicago, Chicago IL), or 1:1500 dilution of HECD1 antibody (Abcam) and Alexa Fluor Goat anti Mouse 647 (Invitrogen). For C3 transferase washout experiments, cells were incubated with 1ug/ul C3 transferase (Cytoskeleton, Inc.) diluted in serum-free media for 4 hours, washed with PBS, and then replaced with fresh media.

Image analysis: For junction length analysis, junction lengths were measured manually in each frame using the free hand line tool in FIJI software (Schneider et al., 2012). Strain and strain rates were calculated from this data using custom R scripts. Junction width analysis was done by taking a junctional region of 3um by 3um and measuring fluorescence intensities with the FIJI intensity analysis tool. Full width by half maximum was calculated by hand in Excel. Proximal fluorescence intensity analysis was done by taking a region proximal to the

junction outside of the junctional regions and also measured using the FIJI intensity analysis tool. Localization of microdomains was calculated by measuring the distance of concentrated membrane regions from each vertex using the FIJI line tool. Vesicle number was calculated using FIJI by thresholding and segmenting the image to create a mask of vesicles within the cell perimeter, which was overlaid onto the channel for segmentation and measurement analysis in FIJI. Cell perimeter and area was calculated manually by tracing cell junctions with the line tool in FIJI. Shape parameter was then calculated in Excel.

Immunofluorescence: Cells were seeded onto collagen gels in Lab Tek II Chamber Slides (Thermo Fisher Scientific) and allowed to form a polarized, mature monolayer before fixing. Cells were fixed in a solution of 4% paraformaldehyde with 0.1% Triton X-100 in PBS solution (Corning). Cells were permeabilized in 0.5% Triton X-100 for 10 min and blocked with 2.5% BSA and 0.1% Triton X-100 in PBS for 1 hr. Cells were incubated with mouse HECD1 antibody (Abcam) at 1:300 in blocking solution overnight at 4C and washed three times in 0.1% Triton X-100 for 20 min each, and then placed in secondary antibody Alexa Fluor Goat anti Mouse 647 (Invitrogen) in blocking solution for 1 hr. After another three 20-min washes with 0.1% Triton X-100, slide chambers were removed. Samples were prepared with 20μl ProLong Gold (Thermo Fisher Scientific) per well and sealed with glass coverslips. Slides were allowed to dry, sealed with nail polish, and stored at 4C.

Quantification and statistical analysis: Statistical significance was determined under specific experimental conditions and was established during a two-tailed Student t-test in Prism (Graphpad, La Jolla California). n represents the number of junctions activated and used in each experiment, as indicated in the figures. For analysis of shape parameters and vesicle internalization, 30 cells were used for each condition.

Model implementation: The vertex model is implemented using Surface Evolver [162]. A tissue of 50 cells is generated and relaxed, without junctional remodeling, to a stable energy minimum. 15 different edges within the tissue are selected for activation, with the tissue reset to its stable state after activation. A time step of Δ_t=0.058 s is used to numerically

simulate the dynamics.

Cell-based model for epithelium with variable tension and junctional remodeling Vertex model for epithelial mechanics: Each cell is modelled by a two-dimensional polygon, with edges representing cell-cell junctions, and vertices three-way junctions. The mechanical energy for the tissue is given by [90]: $E = \sum_\alpha \frac{1}{2} K \left(A_\alpha - A_0\right)^2 + \sum_{ij} \Lambda_{ij} L_{ij}$, where the first term represents the area elasticity of each cell, A_α is the area of cell α, A_0 is the preferred area, and K is the areal elastic modulus. The second term is the interfacial energy resulting from cortical tension and cell-cell adhesion, where L_{ij} is the length of edge ij connecting vertices i and j, and Λ_{ij} is the tension on that edge.

The net mechanical force acting on vertex i with position x_i is given by $F_i = -\partial E / \partial x_i$. Assuming overdamped dynamics, the equation of motion for the vertex i is: $\mu \frac{dx_i}{dt} = F_i$, where μ is an effective friction coefficient. Prior to RhoA induced contractions, all cell-cell junctions are assumed to carry uniform tension, Λ. Under applied mechanical strain both tension and junctional lengths can remodel as described below.

To model the mechanical effect of optogenetic activation of RhoA on cell junctions, we increase the tension on the activated edge ij, by an amount $\Delta\Lambda = \Gamma_{opt} L_{ij}$, where Γ_{opt} is applied contractile force per unit length, and L_{ij} is the length of the edge. The increase in tension is assumed to be proportional to the edge length, so as to produce a strain that is independent of the initial edge length, as observed in our experiments. Having a constant strain, $\Delta\Lambda = \Lambda_{opt}$, applies a higher strain on shorter edges.

Mechanosensitive junctional remodeling: Each cell-cell junction has a rest length, L_{ij}^m, which is the length at which the junctional elastic strain is zero and the tension is constant. Prior to RhoA induced contraction of edge ij, $L_{ij}^m = L_{ij}$. As the junctional edges contract or expand due to applied forces, the rest length remodels over time to adjust to the current length of the edge [151] $\frac{dL_{ij}^m}{dt} = k_l \left(L_{ij} - L_{ij}^m\right)$ where k_l is the rate of rest length remodeling. When the edge is stretched, or compressed, above a critical strain, ϵ_c, the edge tension begins to remodel:

$$\frac{d\Lambda_{ij}}{dt} = \begin{cases} -k_e \left(L_{ij} - L_{ij}^m \right), \text{ if } \epsilon_{ij} > \epsilon_c \\ -k_c \left(L_{ij} - L_{ij}^m \right), \text{ if } \epsilon_{ij} < -\epsilon_c \\ 0, \text{ otherwise} \end{cases}$$

where k_e is the rate of tension remodeling during extension, k_c the rate of tension remodeling during compression, and $\epsilon_{ij} = \left(L_{ij} - L_{ij}^m \right) / L_{ij}^m$ is the strain on the edge. since cell membrane can buckle easily under compression, and stiffen under extension, we allow the remodeling rates to be different during extension and compression.

Short timescale contraction: If the contraction is induced for a short period such that $\epsilon > -\epsilon_c$ then the edge tension does not remodel and remains constant at Λ. The edge length contracts by an amount proportional to Γ_{opt}, and the rest length remodels at a rate k_l to approach the current length. As the applied contraction is turned off, $\Gamma_{opt} = 0$, the edge length fully recovers to its pre-stimulus value, determined by the balance between tension (Λ) and elasticity.

Long timescale contraction: During long timescale contraction of an edge, the edge gains a permanent increase in tension due to tension remodeling ($\epsilon < -\epsilon_c$) . As a result, the balance between edge tension and elasticity is altered, leading to a shorter final length in the steady state after the contraction is turned off

Ratcheting: since we observe that the strain on an edge is independent of the initial edge length, applying a second activation to an already-shortened junction should lead to further contraction, even in the case of a long, saturated contraction. During the first contraction, at long times the strain rate slows down and the rest length remodels and the strain falls below the critical strain, stopping tension remodeling and eventually leading to a saturation of the contraction. After activation the edge recoils to a new length. A second activation leads to a fast contraction, which strains the edge above the critical strain, and so the tension continues to increase, leading to a further decrease in junction length. Thus, applying repeated contractions can repeatedly shorten the junction.

Different model limits A) Vertex model with constant tension and constant rest length $\left(\frac{dL_{ij}^m}{dt} = 0; \frac{d\Lambda_{ij}}{dt} = 0\right)$ Using the traditional vertex model, we find that, regardless on contraction time, junctions always return to their initial length after contraction. Other common variants on the vertex model also fail to capture the change in length of the edges, such as including an energy term proportional to square of the perimeter). The stable state of the junction is such that forces balance since forces do not change during a contraction, the stable state remains unchanged and the junction returns to its initial length. This model is equivalent to setting tension remodeling to zero. B) Vertex model with constant rest length and tension remodeling $\left(\frac{dL_{ij}^m}{dt} = 0\right)$ − With no rest length remodelling, an activation would shorten the edge and increase the edge tension. After the activation, the new steady state length is shorter than the rest length, leading to a further increase in tension and an even shorter rest length. This positive feedback loop would lead to the collapse of any junction after an activation. C) No critical strain for tension remodeling ($\epsilon_c = 0$) - With $\epsilon_c = 0$, after activations the edges slowly recover to their original length. With no critical strain, the tension increases during and activation, but immediately after activation it begins to decrease. As a result, the junction extends, further decreasing the tension until it returns to its original length. In particular, the recoil continues for a long time when compared to experiments. With a critical strain, the tension stops decreasing and a new steady state is reached. D) Constant applied tension - Increasing the tension by a constant amount during an activation, Λ_{opt} instead of $\Gamma_{opt}L$, shrinks edges at a constant speed, independent of initial length, and so shorter edges experience a much higher strain rate than longer edges. In contrast, using a tension proportional to the edge length leads to a strain rate independent of edge length, as in experiments.

Model Parameters: Model parameters are fit to the experimental data by minimizing the error between simulated and experimental data, for $2, 5, 10, 20$, and 40 -minute activations. We minimize the mean square error between individual simulated lengths and mean experimental lengths during an activation during and after the activation, averaged over the different

activation times:

$$\text{Error } = \frac{1}{5}\sum_a \sum_{ij} \frac{1}{T_a}\int_0^{T_a} \left(\left\langle \frac{L^a_{exp}(t)}{L^a_{exp}(0)} \right\rangle - \frac{L^a_{ij}(t)}{L^a_{ij}(0)} \right)^2 dt$$

where $a = 2, 5, 10, 20, 40$ indicates the activation time, ij, indicates the simulated edge being activated, T_a is the total time recorded in experiments for activation a, and $\left\langle \frac{L^a_{exp}(t)}{L^{(0)}_{exp}} \right\rangle$ is the normalized length in experiments averaged over all activations. We then use the Nelder-Mead algorithm implemented in scipy to minimize the error, giving the parameters in the table below.

We nondimensionalize our parameters by rescaling length by $A_0^{1/2}$ and force by $KA_0^{3/2}$, so that the nondimensional energy becomes

$$E = \Sigma_\alpha \frac{1}{2}\left(A_\alpha - 1\right)^2 + \sum_{ij} \Lambda_{ij} L_{ij}$$

Parameter	Symbol	Value
Default edge tension	Λ	0.142
Rest length remodeling rate	k_l	0.159/min
Contraction tension remodeling rate	k_c	0.0203/min
Extension tension remodeling rate	k_e	0.000/min
Critical strain	ϵ_c	0.122
Optogenetic contractility	Γ_{opt}	0.0846
Viscosity	μ	1.132mins

3.7 Acknowledgements

KEC acknowledges an HHMI Gilliam Fellowship, National Academies of Sciences Ford Foundation Fellowship, and NIH training grant GM007183. MLG acknowledges funding from NIH RO1 GM104032 and ARO MURI W911NF1410403. This work was partially supported

by the UChicago MRSEC, which is funded by the National Science Foundation under award number DMR-1420709. MFS is supported by an EPSRC funded PhD studentship. SB acknowledges funding from the Royal Society (URF/R1/180187) and HFSP (RGY0073/2018). EM acknowledges funding from NIH RO1 HD099931.

CHAPTER 4

FEEDBACK BETWEEN RHOA AND E-CADHERIN ELICIT AN ASYMMETRIC JUNCTIONAL MECHANORESPONSE

4.1 Overview, aims, and contributions

The work described here uses pharmacological and optogenetic activations of RhoA to determine the origins of contractile asymmetry during junction contractions. We couple experimental data with mathematical modeling to discern the functional relationship between vertex motion, junction tension, and adhesive drag.

The aims include the following:

- To elucidate the origins of contractile asymmetry during junction contractions
- To examine physically how a junction contracts upon force application
- To derive an enhanced, mathematical Vertex model to account for experimental data
- To determine the feedback between RhoA and E-Cadherin that generates vertex motions and frictional drag

The manuscript is currently in preparation. The contributions are as follows:

Kate Cavanaugh: Manuscript preparation, experimental data collection, and data analysis.

Tracy Chmiel: Data analysis on fiducial displacements, center of contractions, vertex percent motion, and RhoA localization.

Michael Staddon: Simulations of the vertex-based model and theoretical analysis.

Srikanth Budnar: Generation of E-Cadherin CRISPR cell lines.

Alpha Yap: Review and editing the manuscript.

Shila Banerjee: Review and editing the manuscript, theoretical analysis of the vertex-based model.

Margaret Gardel: Review and editing the manuscript, supervision of work.

4.2 Abstract

Tissue morphogenesis may arise from the culmination of discrete changes in cell-cell junction behaviors, namely ratcheted junction contractions that lead to collective cellular rearrangements. Mechanochemical signaling in the form of RhoA underlies these ratcheted contractions, which occur asymmetrically as one highly motile vertex contracts toward a relatively less motile tricellular contact. While this phenomenon is well characterized, the underlying mechanism driving differential vertex movement remains unknown. Here, we use optogenetic and pharmacological RhoA activators in model epithelia to uncover the mechanism leading to this asymmetry in vertex motion. We find that both local and global RhoA activation leads to increases in junctional tension, thereby facilitating vertex motion. RhoA activation occurs in discrete regions along the junction and is skewed towards the less-motile vertex. At these less-motile vertices, E-cadherin acts as an opposing factor to limit vertex motion through increased frictional drag. Surprisingly, we uncover a feedback loop between RhoA and E-cadherin, as regional optogenetic activation of specified junctional zones pools E-cadherin to the location of RhoA activation. Incorporating this into a mathematical model, we find that this novel circuit between RhoA-mediated tension, E-cadherin-induced frictional drag, and vertex motion recapitulates experimental data. We test this model by altering E-cadherin interactions and thus frictional drag, which modulated the resulting RhoA-induced vertex asymmetry. As such, the location of RhoA determines which vertex is under high tension, pooling E-cadherin and increasing the frictional load at the tricellular vertex to limit its motion. This feedback drives a tension-dependent intercellular "clutch" at tricellular vertices which stabilizes vertex motion upon tensional load.

4.3 Introduction

Morphogenesis relies on the tight spatiotemporal control of cell-cell junction lengths [1]. Contractile forces, acting at adherens junctions, alter junction lengths as a cyclic ratchet

[64–66, 145, 163]. Preceding these ratcheted contractions are highly dynamic pulses of active GTP-bound RhoA [57, 59, 64], the strength and temporal pattern of which control junction tension to confer junction length [94, 114]. Through effector activation, highly complex contractile actomyosin arrays assemble rapidly in response to intercellular biochemical signals and/or physical cues from neighboring cells [35]. As such, this highly complex GTP cycle is thought to give rise to spatiotemporal changes in junction length which drive processes like convergent extension. While the molecular components of these mechanochemical systems are well characterized, the mechanisms by which they act to regulate junction tensions and resulting cellular shapes remain largely unknown.

There exists a previously unknown yet innate asymmetry in junction contraction, possibly fueled by heterogeneous force production along the junction length [78]. During junction contractions, non-uniform force production causes very local actomyosin flows to specific regions of the junction for qualitatively different junctional responses. Bicellular edges, for example, act as independent contractile units apart from tricellular endpoints [77, 78]. Medioapical actomyosin flows to the bicellular interfaces generate contractile forces sufficient to deform junctions [59, 64]. Flows to the tricellular vertices restrict these contractions, thus stabilizing the junctional ratchet [78]. The coordination between these spatially distinct actomyosin flows causes asymmetric junction shortening, where a motile vertex contracts into a less-motile vertex to facilitate localized contractions that guide global tissue rearrangements [78]. While this contractile asymmetry is well characterized, its molecular, cellular, and mechanical origin remains unclear. Moreover, it is unknown what designates these junctional zones as contractile in nature.

Cells sense and respond to mechanical inputs through force-sensitive feedbacks acting at junctional adhesion receptors [164]. Apical adhesions, composed namely of E-cadherin, mediate intercellular cell-cell adhesion. However, E-cadherin should be envisaged not as a static participant of cellular adherence but rather as a dynamic sensor of stress that dictates cellular behavior. For example, heightened adhesive force stimulates the RhoA pathway and

myosin light chain phosphorylation, resulting in an overall increase in actin polymerization at adherens junctions [169]. Additionally, force-sensitive effector proteins, like beta-catenin and alpha-catenin, stimulate a catch bond with actin that is strengthened when adhesion complexes experience tensile force [167]. Together these mechanisms cause clustering of E-cadherin molecules and actin to trigger adhesion complex growth [168]. In this way, these proteins subsequently generate a reinforcement response to anchor junctions against applied force [166]. However, it is still unclear if and how cells' force-sensitive coupling of actomyosin and adhesion complexes modulate junction length to coordinate morphogenetic movements within tissues.

Here, we used optogenetic and pharmacologic modulation of RhoA activity to discern how a junction physically contracts upon increases in intercellular force production. We found that junctions inherently contracted asymmetrically upon uniform RhoA activation, with one motile vertex and one less-motile vertex. We then used computational modeling to offer predictions as to how this asymmetry arose. Our experimental data indicated that vertex tension, as predicted by canonical models of epithelial tissues, was insufficient to account for such asymmetry. We then explored how asymmetric contraction and asymmetric friction accounted for experimental results. Here, we found that an asymmetry in RhoA localization generated qualitatively different junctional regimes of contraction and subsequent vertex asymmetry. We found that, upon RhoA activation, tricellular vertices exhibited a mechanoresponse to locally reinforce the vertex to restrict its movement via increases in E-cadherin friction. When feedback between RhoA-mediated tension and E-cadherin-induced friction was incorporated into our model, we were able to recapitulate experimental data. By modulating E-cadherin friction with pharmacological perturbations, we induced symmetry back into the system or abolished junction contraction entirely. Our modeling and experimental data therefore point to a unified model of asymmetry induced by both friction and local contraction that is mediated by a RhoA-dependent mechanosensitive rigidity transition of tricellular vertices.

4.4 Results

4.4.1 RhoA-mediated tension drives vertex motion

To examine how RhoA controls junction contractions, we formed a model tissue by plating a colorectal adenocarcinoma (Caco-2) cell line endogenously CRISPR tagged for E-cadherin on polymerized collagen gels at full confluency to facilitate the monitoring of junctional movements (Fig. 4.1A). We then measured junction length by measuring the interfacial distance from tricellular vertex to the other tricellular vertex. In control conditions, there were negligible changes in junction length over the course of a 2-hour period (Fig. 4.1B, 4.2A). Here, the junction length was maintained and only fluctuated about 1% after the two-hour period (Fig. 4.1B).

We then treated cells with a cell permeable, pharmacological RhoA Activator, CN03, to globally and acutely increase RhoA activity across the entire tissue. We began imaging upon the addition of CN03, at time (t)=0min, and examined junction fluctuations and contractions resulting from RhoA increases until (t)=125min. About 30% of the junctions showed a robust contractile phenotype which led to length changes to about 80% of original junction lengths (Fig. 4.1C, 4.2A). We then manually tracked each vertex over time and measured its displacement (Fig. 4.1D). With the addition of simple media, we found that there was little to no vertex movement (Fig. 4.1B, E). In contrast, CN03 containing media induced asymmetric junction contraction, where one vertex moved significantly more than the other vertex. This asymmetry is reminiscent of observations in developmental systems [78, 171] (Fig. 4.1C, F).

To explore the impact of localized Rho activity, we then used an optogenetic approach. The logic behind this experiment was to have isolated junctions acutely experience heightened and targeted RhoA activation. For spatial and temporal control over RhoA activity, we used a Caco-2 cell line expressing the TULIP optogenetic two-component system [108, 110, 113, 114]. TULIPs' two components include the 1) membrane-tethered photosensitive LOVpep anchor

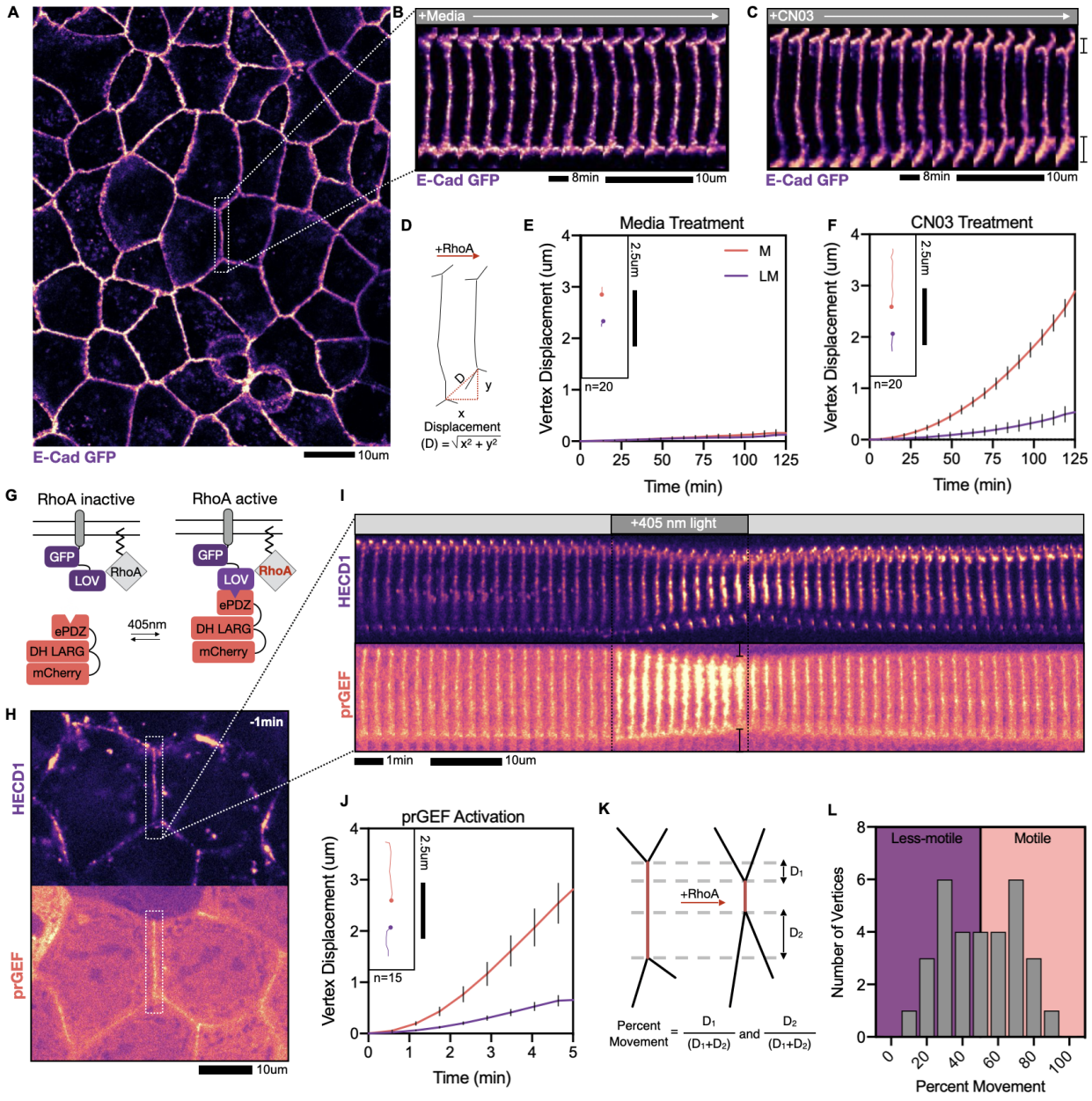

Figure 4.1: RhoA-mediated tension drives vertex motion

Figure 4.1: RhoA-mediated tension drives vertex motion (Continued) A. Representative image of a homeostatic epithelial tissue endogenously expressing E-Cadherin GFP. B. Zoomed in images of WT junction over the course of two hours showing no junction length changes with the addition of media. C. Representative images of timelapse video over the course of two hours showing asymmetric junction shortening with the addition of the CN03 compound. D. Schematic of junction shortening and displacement measurement analysis. E. Vertex displacement analysis for junctions in WT conditions showing little-to-no vertex motion. Inlay shows particle tracks for a representative vertex pair in WT conditions. F. Vertex displacement analysis for junctions in CN03 treatment showing asymmetry in vertex displacements. Inlay shows particle tracks for a representative vertex pair in CN03 treatment. G. Schematic of the TULIP optogenetic system to drive local RhoA activation. H. Zoomed out image of a targeted junction at -10min before optogenetic activation. Top image shows HECD1 junction labeling of E-cadherin and bottom image shows prGEF localization. I. Timelapse of the junction in H undergoing a 5-min optogenetic activation showing asymmetric junction contraction within the activation period and junction relaxation post-activation. J. Vertex displacement analysis for the junction within the 5-min optogenetic activation period. Displacement analysis shows similar vertex asymmetry upon increases in RhoA activity. Inlay shows particle tracks during the 5-min optogenetic activation period for a representative vertex pair. K. Schematic documenting the percent movement analysis. L. A histogram of the percent motions of all vertices undergoing optogenetic activation shows two peaks at 30% and 70%, further documenting vertex asymmetry.

protein and the 2) prGEF complex that houses the photorecruitable PDZ domain attached to the catalytic DH domain of the RhoA-specific GEF, LARG. Blue light (405nm) activation causes a conformational change in the LOVpep domain to expose a docking site for the engineered PDZ domain within the prGEF complex. This blue light activation increases the binding affinity between the two components, thereby recruiting the prGEF to the membrane where it drives local RhoA activation (Fig. 4.1G) [108, 110, 113, 114]. This system has high temporal resolution, as both junctional prGEF recruitment and dissociation are on the order of 30-60 seconds. prGEF recruitment is tightly confined to the targeted cell-cell junction, consistent with previously published work (Fig. 4.1I) [114]. Overall, this system gives tight spatiotemporal control over RhoA activity for which to study how junctions contract upon increases in RhoA activity.

In order to visualize the movement of adhesive sites, serving as fiducial marks along the junction, we labeled E-Cadherin using an antibody labeling technique targeting its extracellular domain. We bathed the cells for at least an hour in E-cadherin primary antibody,

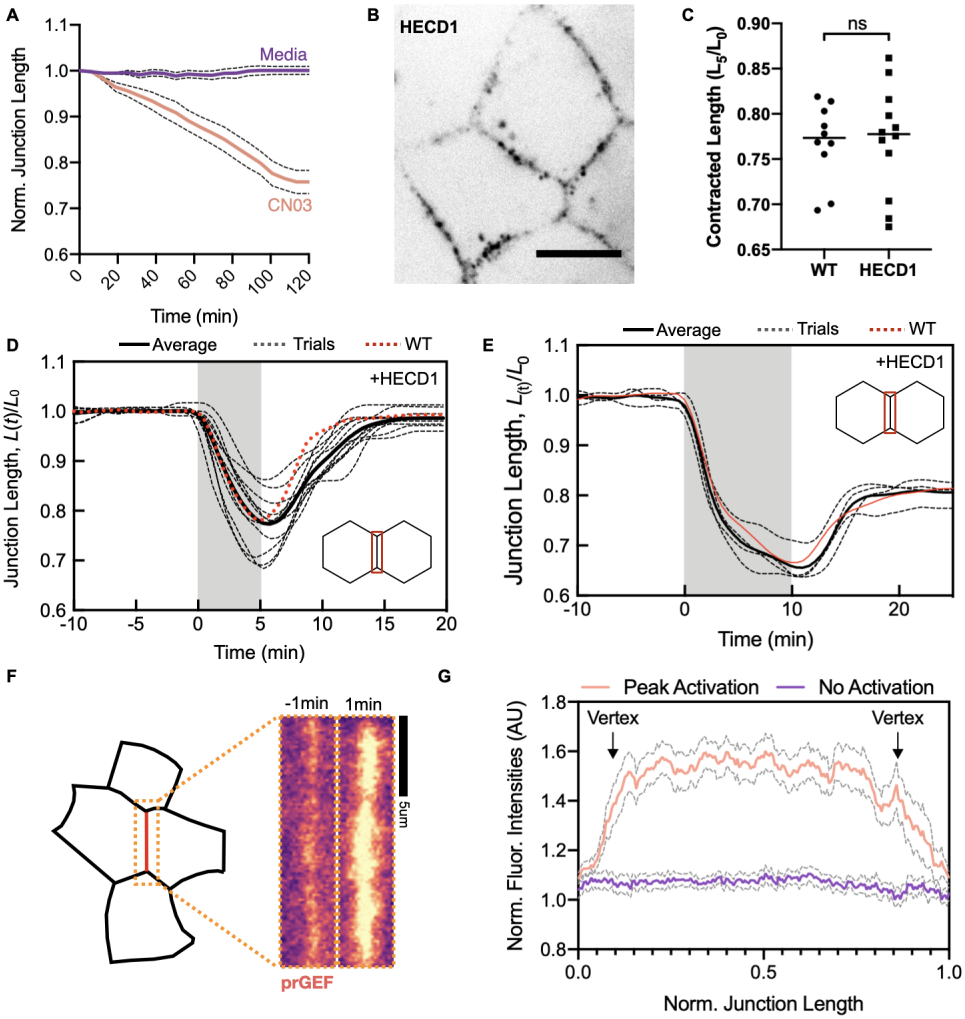

Figure 4.2: HECD1 treatment is noninvasive to the tissue. A. Normalized junction length over the course of two hours in WT and CN03 treatment. WT junctions show no junction length changes while CN03 treatment shows junction contraction to about 80% of original lengths. B. Zoomed out image of junctions labeled with HECD1 shows E-cadherin puncta along the junctions. C. Contracted length, or the length after 5 minutes divided by the initial length, after optogenetic activation at T5 between Control and HECD1-labeled cells. HECD1 treatment shows no difference in contracted lengths. D. Normalized junction length over time for each individual junction in HECD1 treatment showing similar contractile phenotypes after 5-minutes of optogenetic activation compared to the average WT junction contraction, with the junction returning to its original length post-activation. E. Normalized junction length for a 10-minute activation of HECD1 treated cells compared to WT controls. Junctions in HECD1 treatment show similar contractile phenotypes as WT conditions, with the junctions readjusting to about 80% of their original lengths post-activation. F. Schematic of an activated junction (left) with uniform junctional prGEF localization before and after optogenetic activation (right). G. Normalized fluorescence intensities along a normalized junction length showing that the peak activation's prGEF recruitment is uniform along the junction proper compared to pre-activation.

HECD1, and its corresponding fluorescently labeled secondary antibody. HECD1 antibodies target the extracellular region of Ectodomain 2 within E-cadherin, thereby preserving cellular cohesion and intercellular E-cadherin binding in trans via Ectodomains 1. Upon washing out the antibody, we found that this labeling produced a punctate pattern of E-cadherin that delineated the cell-cell junctions and vertices (Fig. 4.1H, 4.2B). Importantly, we found that this treatment had no effect on junction contraction or length remodeling (Fig. 4.2C-E)[114], indicating that this treatment was non-invasive. Specifically, we found that, over a 5-minute light activation period, the targeted HECD1-labeled junctions rapidly contracted to 70-80% of their original length and then returned to their original lengths after light termination, consistent with previous reports (Fig. 4.1I, 4.2C-D) [114]. This contraction was surprisingly consistent across multiple junctions with vastly different initial lengths and geometries.

The vertex displacements in response to local RhoA activation were also asymmetric (Fig. 4.1I, J). To quantify the asymmetry, we measured percent movement of each vertex and plotted its probability density (Fig. 4.1K). We. This revealed an asymmetry in the histogram with peaks around 30% and 70%, further indicating an inherent asymmetry to junction contraction (Fig. 4.1L). This was starkly contrasted to a symmetric contraction with one peak centered a to 50%. Interestingly, this vertex asymmetry occurred despite uniform prGEF recruitment along the junction, discarding the possibility that heterogeneous regions of RhoGEF recruitment could trigger asymmetric junction contraction (Fig. 4.2F-G).

4.4.2 Asymmetric RhoA drives contractile asymmetry

Junctions could either contract uniformly along their length or contain individual sub-junctional segments that contract varying amounts. To explore these possibilities, we used the variable intensities of HECD1 labeling to examine local variations in deformations along the junction. A line-scan along the junction, taken over time, created a kymograph for which to analyze fiduciary flows before, during, and after light-actuated junction contraction (Fig. 4.3A).

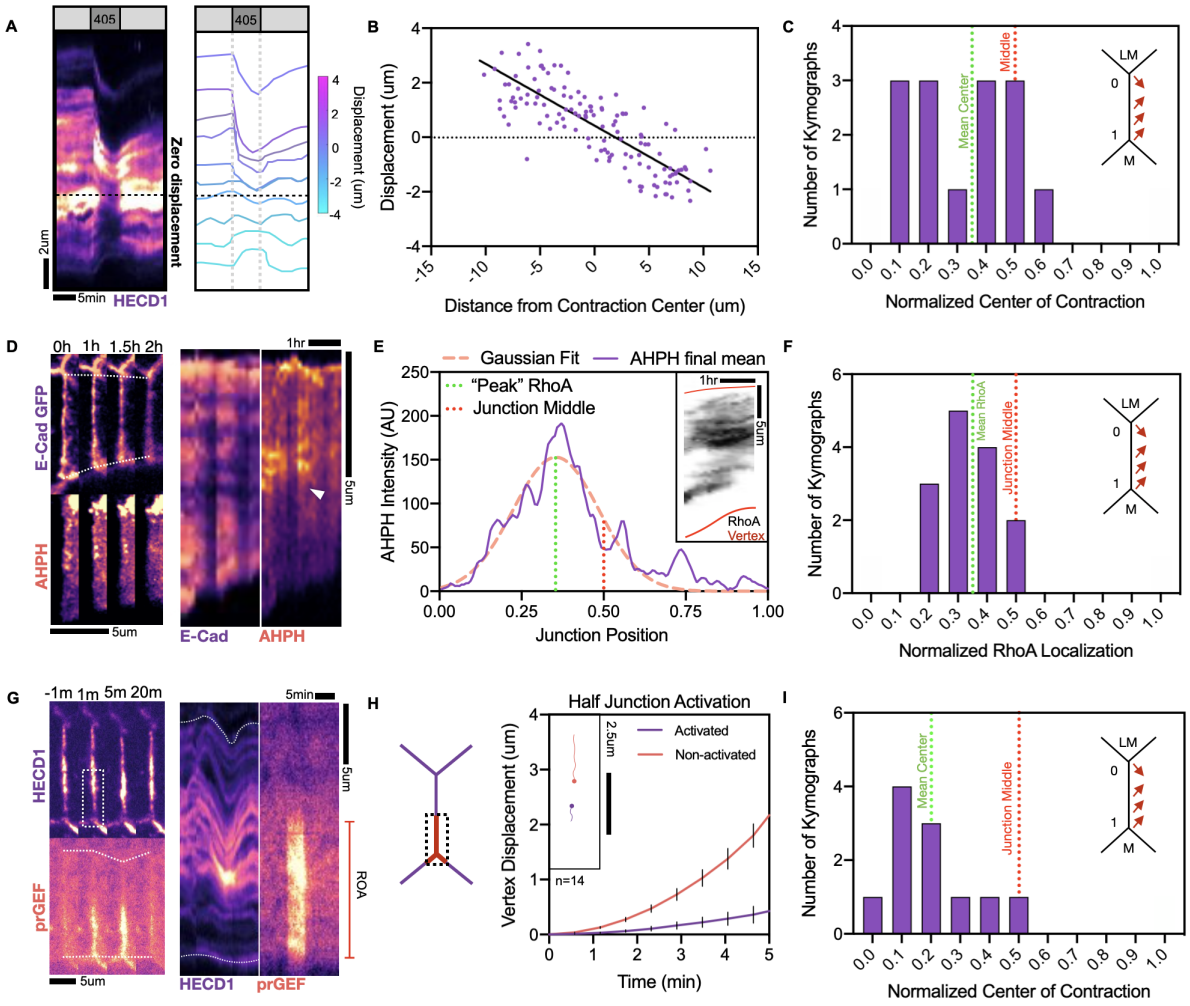

Figure 4.3: Asymmetric RhoA drives contractile asymmetry A. (Left) Representative kymograph of an optogenetically activated junction labeled with HECD1. (Right) Fiducial marks seen in the kymograph are color coded according to their displacement. B. Displacement analysis of each fiducial mark's flows as a function of the distance from the contraction center. C. Inlay shows diagram of the Less-motile (LM) vertex being labeled as 0 and the Motile (M) vertex being labeled as 1. The localization of zero displacement (as seen in A) of the fiduciary marks indicates the center of the junction as being skewed towards the less motile vertex. D. (Left) Representative junction in CN03 treatment expressing E-cadherin-GFP and transfected with the AHPH. (Right) Kymograph shows a RhoA flare that is biased towards the less-motile vertex. E. Analysis of the junctional AHPH intensity plots averaged over the last 5 frames of the kymograph fitted to a Gaussian curve. Dotted line indicates the peak of the Gaussian fit, indicating the centralized location of the RhoA biosensor. Inlay shows representative kymograph from which the plot was taken. F. Pooled analysis of the peak of the RhoA biosensor, as calculated in E, showing mean junctional RhoA localization as being skewed towards the less-motile vertex. G. Representative image and kymograph of a junction undergoing half-junction activation. H. Vertex displacement of bottom-junction activation. Inlay shows individual vertex tracks in a vertex pair. I. Normalized center of contraction analysis for bottom-junction activation.

Using these kymographs, we then measured fiducial marks' and vertices' maximal displacement over time (Fig. 4.3A). The maximal displacement of each contracting E-cadherin puncta was measured as a function of the position along the junction, for which we then calculated a linear fit. The kymograph's center of contraction was determined by the root value of that linear fit, and the center of contraction was then normalized so that the position of the more motile vertex was 1 with the less motile vertex was 0. For a heterogeneous contraction, the displacement of a fiducial marker would not be proportional to its distance from the contraction center. Instead, we found that the maximum fiducial displacement as a function of the distance from the center of the junction contraction revealed a monotonic, linear trend indicative of a uniform contraction (Fig. 4.3B).

We next sought to characterize the asymmetry in contraction. For a symmetric contraction, we expected to see the center of contraction at 0.5. Instead, we found that the location of zero displacement for the fiduciary marks to be skewed towards the less-motile vertex (Fig. 4.3A, C). Analyzing multiple kymographs revealed that the mean center of junction contraction was consistently closer to the less-motile vertex with a mean center of junction contraction at 0.32 (Fig. 4.3C).

In development, RhoA pulses precede junction contractions [59, 64], we next sought to directly determine the role and location of active RhoA in this asymmetric junction contraction. It is possible that RhoA activation is not uniform along the junctions, giving rise to heterogeneous stress along the junction. For this, we turned to examining the well-established RhoA biosensor (AHPH) containing the GTP-RhoA binding C-terminal portion of Anillin [136]. We transfected the E-cadherin expressing cells with the AHPH and then turned to our CN03 wash-ins to visualize RhoA upon junction contraction. We observed that junctional RhoA flares were skewed towards the less-motile vertex (Fig. 4.3D, E inlay). These flares were absent from junctions without CN03 treatment (Fig. 4.4A-D). We then analyzed the normalized RhoA localization by averaging junctional RhoA intensities over the last 5 frames of the kymograph. Fitting a Gaussian curve to this data, we labeled the

peak of this Gaussian as the location of the "peak" RhoA region (Fig. 4.3E). By analyzing fourteen kymographs, we found that the mean RhoA region was also skewed towards the less motile vertex with a mean localization of 0.35 (Fig. 4.3F), in the proximity of the center of contraction (Fig. 4.3C).

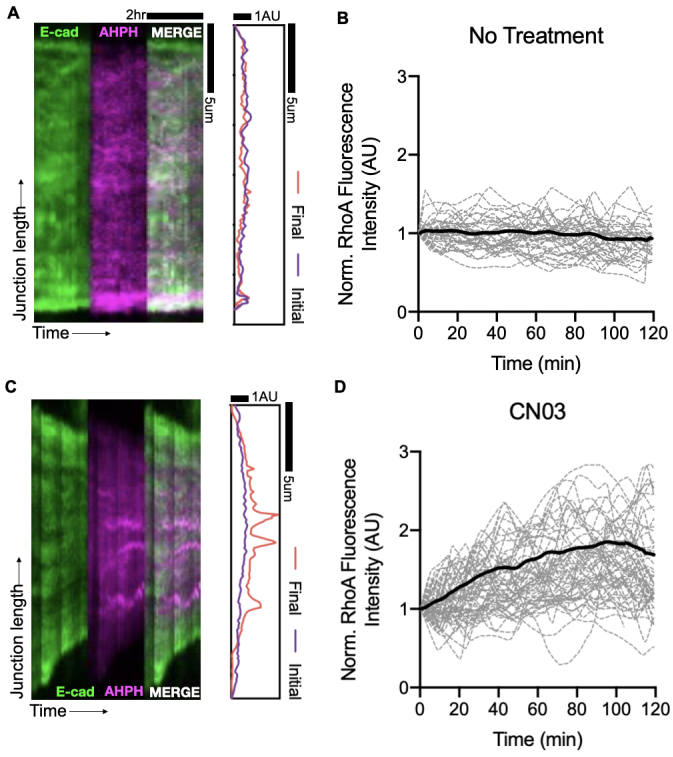

Figure 4.4: Transient RhoA flares occur along the junction during shortening. A. Representative kymograph showing a junction in WT treatment. B. Quantification of normalized RhoA AHPH intensity over the course of two hours in WT treatment. C. Representative kymograph of a junction in CN03 treatment undergoing shortening. D. Quantification of normalized RhoA AHPH intensity in CN03 treatment.

The above data indicated that the location of RhoA flares were critical in determining asymmetric contraction, with reduced mobility of the vertex proximal to active RhoA. To test this hypothesis, we exploited the optogenetic approach to systematically activate only a portion of the junction. When the lower half of the junction was activated, the junction contracted to about 85% of its original length, similar to the extent for full junction activation. The vertex proximal to the region of activation (ROA) was significantly less mobile than the distal vertex (Fig. 4.3G, H). Kymograph analysis in the HECD1 channel revealed that the

center of contraction for the half junction activation was 0.2 (Fig. 4.3I), skewed even further towards the less-motile vertex than for uniform activation. Altogether these data indicate that asymmetry in RhoA activation dictates the bias in vertex motion.

4.4.3 E-cadherin opposes vertex motion via frictional drag

RhoA acts at cell-cell interfaces to regulate morphology through its effect on actomyosin tension and adhesion strength [114]. To explore the possibility that changes in adhesion strength underlie vertex immobility, we analyzed E-cadherin localization, as visualized by HECD1 fluorescence, at tricellular vertices during optogenetic stimulation. We observed HECD1 fluorescence in punctae along the junction and at both vertices. We monitored the HECD1 fluorescence at both vertices during an activation experiment. At the more mobile vertex, we found that the HECD1 intensity did not vary significantly during the experiment (Fig. 4.5A, red arrow). By contrast, at the less mobile vertex, we found there was a marked increase of HECD1 immediately after activation which diminished after exogenous stimulation was removed (Fig. 4.5A, B). This trend was consistent across numerous junctions and paired vertices (Fig. 4.5C). Together these data indicate that apical E-cadherin elicits a tricellular mechanoresponse to possibly induce friction and limit vertex motion upon increases in junctional RhoA.

Similarly, upon fixing and staining the tissue, we saw preferential localization of E-cadherin to tricellular contacts upon modulation of RhoA activity using pharmacological inhibitors (C3 transferase) and activators (CN03) compared to WT media conditions (Fig. 4.5D). By inhibiting RhoA activity, we found little tricellular E-cadherin compared to bicellular junction E-cadherin when fixed and stained (Fig. 4.5E, F). In heightened RhoA activity, we found an increase in tricellular E-cadherin recruitment compared to WT controls (Fig. 4.5E, F). These data indicate that E-cadherin is mechanosensitive, possibly indicating that a functional circuit between E-cadherin and RhoA.

As we suspected E-cadherin-mediated frictional drag influenced junction contraction, we

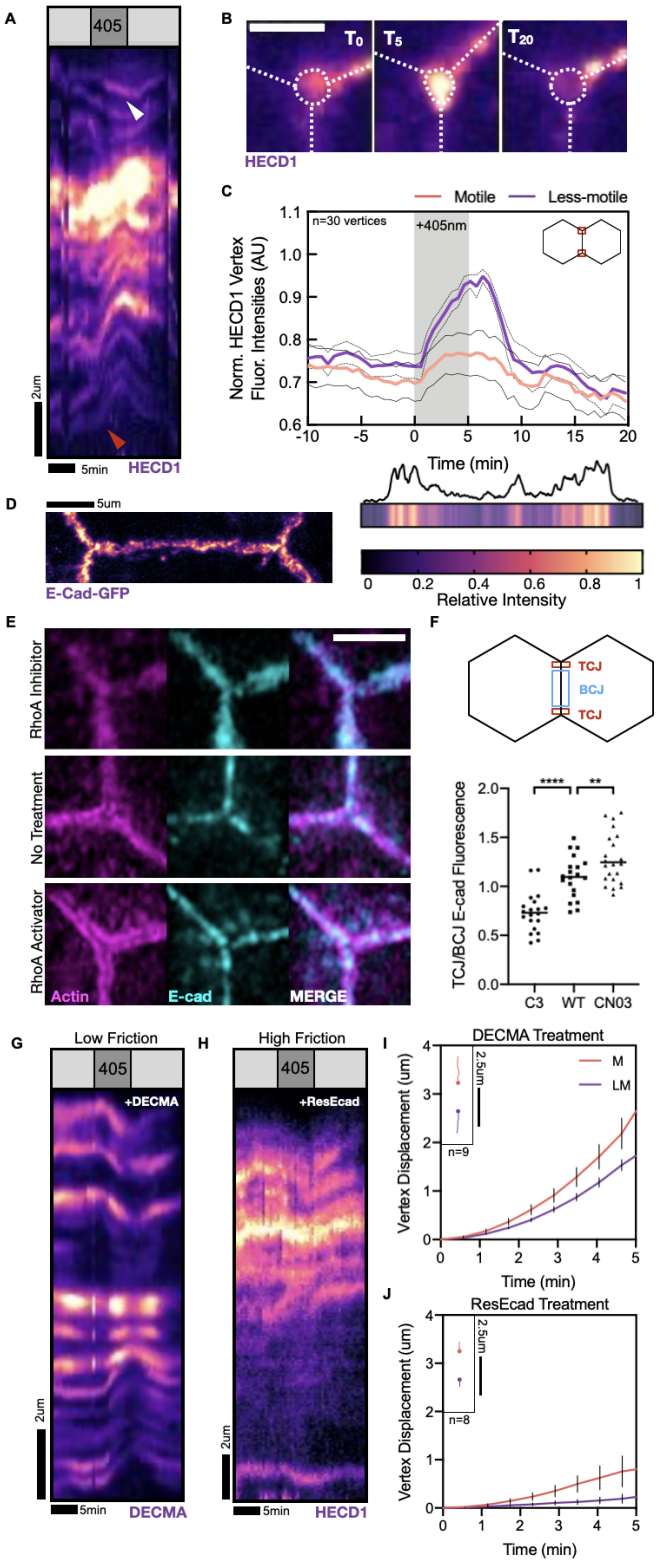

Figure 4.5: E-Cadherin at tricellular contacts regulates vertex friction

Figure 4.5: E-Cadherin at tricellular contacts regulates vertex friction (Continued) A. Representative kymograph of optogenetic activation showing increases in E-cadherin pooling at the less-motile vertex (white arrow) versus the motile vertex (red arrow). B. Representative image of a less-motile tricellular contact showing E-cadherin pooling at the vertex after 5 minutes of optogenetic activation. C. Quantification of vertex fluorescence intensities of motile and less-motile vertices. Less-motile vertices show increases in E-cadherin pooling and subsequent vertex fluorescence compared to motile vertices. D. (Left) Representative image of E-Cadherin GFP labeled cell showing preferential localization of E-Cad to the vertices. (Right) Linescan and corresponding heat map of intensity values along the junction shown on the left. E. Representative images of cell junctions treated with RhoA activator (bottom), media (middle), or RhoA Inhibitor (top). Cells are stained for actin in magenta and E-cadherin in cyan. F. Quantification of tricellular junction:bicellular junction E-cadherin intensities for RhoA conditions. G. Representative kymograph of treated junction with the E-cadherin blocking antibody, DECMA. DECMA treatment introduced symmetry back into contraction upon optogenetic activation. H. Representative kymograph of cells treated with ResEcad showing little-to-no junction contraction. I. Vertex displacement analysis of DECMA-treated junctions showing symmetric contraction. Inlay shows particle tracks of a representative vertex pair during optogenetic activation. J. Vertex displacement analysis of ResEcad-treated junctions showing a severe reduction in the contraction of junctions, resulting in reduced vertex motions and asymmetry. Inlay shows particle tracks of a representative vertex pair during optogenetic activation.

next sought to modulate E-cadherin interactions. First, we used a function blocking antibody, DECMA, and its conjugated secondary antibody to visualize junctional dynamics. DECMA binds specifically to Ectodomain 1 on E-cadherin, abolishing any trans interactions between E-cadherin molecules, thereby reducing E-cadherin binding. Upon addition of DECMA, we found a similar labeling pattern of E-cadherin that coated the junction (Fig. 4.5G). Optogenetic activation induced similar junctional contractions compared to WT conditions, but the contraction was more symmetric (Fig. 4.5G, I). To increase junctional friction, we next sought to increase the levels of E-cadherin through the cell-permeable, pharmacological isoxazolocarboxamide compound, ResEcad [172]. This compound has been shown to induce a dose-dependent increase in E-cadherin levels in adenocarcinoma cells, thereby modulating junctional friction levels. We found ResEcad treatment severely suppressed optogenetically-induced junction contraction (Fig. 4.5H, J). Of note, we found that this frictional force was restricted to the apical adhesion complexes, as modulating substrate stiffness did not affect vertex asymmetry (Fig 4.6A-I). These data indicate that modulating E-Cadherin levels

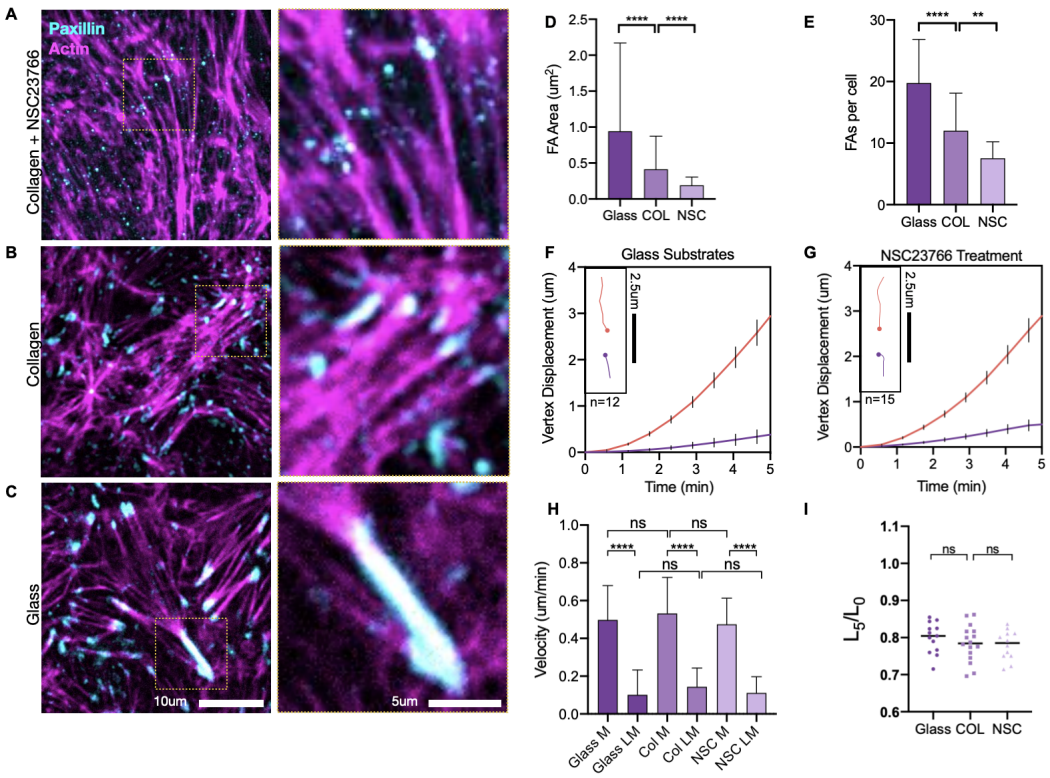

Figure 4.6: Vertex asymmetry is independent of basal substrate friction. A. A. Representative image (left) and zoom (right) of the basal substrate surface of cells plated on collagen with Rac Inhibitor, NSC23766, which has been shown to decouple cell-substrate interactions while maintaining cell-cell interactions. Paxillin, a focal adhesion marker, is in cyan and actin is in Magenta. B. Representative image (left) and zoom (right) of the basal substrate surface of cells plated on collagen. Paxillin is in cyan and actin is in magenta. C. Representative image (left) and zoom (right) of the basal substrate surface of cells plated on glass. Paxillin is in cyan and actin is in magenta. D. Quantification of focal adhesion (FA) area among all three conditions showing decreasing FA size with softer substrates (collagen) and substrate decoupling (collagen + NSC23766). E. Quantification of FA number per cell among different conditions show decreasing FA number with softer substrates (collagen) and substrate decoupling (collagen + NSC23766). F. Vertex displacement analysis of activated junctions of cells plated on glass shows vertex asymmetry. Inlays show representative particle tracks of a vertex pair during the optogenetic activation period. G. Vertex displacement analysis of activated junctions of cells plated on collagen + NSC23766 shows vertex asymmetry. Inlays show representative particle tracks of a vertex pair during the optogenetic activation period. H. Analysis of vertex velocities of motile (M) and less-motile (LM) vertices among all three substrate stiffness conditions. Analysis shows asymmetry within each condition, but similar asymmetry across all three conditions tested, suggesting vertex asymmetry is independent of substrate stiffness. I. Quantification of the contracted length after optogenetic activation, L5, divided by the initial junction length, L0, among all substrate stiffness conditions tested. Data show the contracted length is similar among all conditions, suggesting substrate does not affect initial junction contractions.

and interactions, inducing either low or high friction, can influence both the magnitude and asymmetric nature of vertex motions.

4.4.4 Towards a mechanical model of vertex asymmetry

To quantitatively explain the biomechanical origins of asymmetric vertex motion, we developed a continuum mechanical model for the junction dynamics arising from the balance of tensional forces of the primary junction with the two neighboring shoulder junctions, and a frictional drag acting at the vertices to resist their motion (Fig. 4.7A). We modeled the junction as a linear elastic continuum with compressional modulus E, tension Λ, and dissipating stresses with a friction coefficient μ(Fig. 4.7B). Our approach stands in contrast to existing vertex models of epithelial tissues modelled as networks of edges under uniform and constant tension, with the vertex positions determined by force balance from the neighboring junctions. By modelling the junction as an elastic continuum, we allow for the junction tension and friction forces to vary along the length of the junction, such that the displacement along the junction may be tracked during a contraction event (Fig. 4.7C). Mechanical force balance at a point along the junction can be written as

$$\mu \frac{\partial u}{\partial t} = -E \frac{\partial^2 u}{\partial x^2} - \frac{\partial \Lambda}{\partial x} \ldots\ldots\ldots (1)$$

where $u(x,t)$ is the displacement along the junction at time t, and x is the position along the junction. The shoulder junctions were modeled as providing a spring-like resistance to motion, with an effective stiffness k that depend both on both the tension and the geometry of the shoulder junctions (see Model Methods). Force balance at the tricellular vertices is given by

$$E \frac{\partial u}{\partial x} + \Lambda = k_1 u \ldots\ldots\ldots (2)$$

at $x = x_1$ and

$$E \frac{\partial u}{\partial x} + \Lambda = -k_2 u \ldots\ldots\ldots (3)$$

at $x = x_2$, with k_1 and k_2 being the stiffnesses of the two shoulder junctions. To simulate RhoA-induced contraction, we apply a uniform contractile stress for a duration of 5 minutes to a junction initially at rest and record the resulting displacements of the two vertices. These displacements are obtained by solving Eq. (1) subject to the boundary conditions given by Eqs (2) and (3). We then used the model to test three different mechanisms for asymmetric vertex motion and heterogeneous mechanical response arising from (i) differential elastic resistance at the shoulder junctions, (ii) differential friction and (iii) asymmetric tension along the junction.

Differential elastic resistance at the shoulder junctions - We first tested how the asymmetry in vertex motion was regulated by differential elastic resistance from the shoulder junctions using our continuum mechanical model. For each vertex, we sample the shoulder junction stiffness k_i from a Normal distribution with mean k_0 and standard deviation $k_0/3$. For each vertex, we then compared the percentage of total vertex displacement (relative displacement), $u_i/\left(u_1 + u_2\right)$, against the percentage of total shoulder stiffness (percent, or relative stiffness), $k_i/\left(k_1 + k_2\right)$. Expectedly, we found that vertex displacement depends linearly on shoulder stiffness, with relative displacement decreasing with increasing relative stiffness (Fig. 4.7D).

To test the model predictions using our experimental data, we estimated the elastic resistance at shoulder junctions by computing the tensions along shoulder junctions and change in their geometries during a contraction event, as measured by calculating junction length and the interior angles normal to the activated junction (see Model Methods). From the angles between the activated junction and its neighbors, we calculated the relative tensions on each junction by balancing forces both along the junction and perpendicular to it. From these tensions, we then calculated the differential change in force due to a differential change in vertex position, which defines the effective stiffness of the shoulder junctions (see Methods). However, when we quantified the relative stiffness using data from our optogenetic experiments, we found no correlation with relative vertex displacement (Fig. 4.7G) , indicating that asymmetric elastic resistance at the vertices do not play a role in

predicting asymmetric vertex motion upon contraction.

Differential friction along the junction - An alternative mechanism for asymmetric vertex motion could arise from heterogeneous adhesive properties at the tricellular vertices or even along the junction proper that may alter the frictional drag. Indeed, our experimental data show that there is a marked increase in E-cadherin level at the less mobile vertex compared to the motile one (Fig. 4.3). We therefore sought to test if different frictional forces at the vertices could capture the asymmetric vertex motion. At each vertex, friction is set to a random value sampled from a normal distribution with mean μ_0 and standard deviation $\mu_0/3$, and values are linearly interpolated along the junction. We found a linear dependence of relative displacement $u_i/\left(u_1+u_2\right)$ on relative friction $\mu_i/\left(\mu_1+\mu_2\right)$, with μ_1 and μ_2 being the friction coefficient at the two vertices, such that increased friction resulted in reduced motion (Fig. 4.7E). As an estimate of the friction in experimental measurements, we measured the relative percentage of HECD1 at each vertex compared to the total amount of HECD1 within each vertex pair. To our surprise, we did not find any correlation between vertex motion and initial cadherin-mediated friction (Fig. 4.7H). In fact, HECD1 was distributed rather evenly at both vertices before optogenetic activation.

Tension asymmetry along the junction - Finally, we considered the effects of varying tension along the junction induced by RhoA mediated contractility. We varied tension along the junction by setting the tension at each vertex to be a random value sampled from a normal distribution with mean Λ_0 and standard deviation $\Lambda_0/3$, and linearly interpolated tension along the junction. We found that vertices under higher tension (more contractility) underwent larger displacements (Fig. 4.7F). To measure relative junction tension, we returned to our CN03 wash in experiments to measure RhoA intensities. We split the junction into two halves and measured the relative intensity of AHPH at each junctional portion compared to the total amount of AHPH along the junction proper. Plotting relative displacement as a function of this percentage of RhoA intensity, we found a correlation between less-motile vertices and the relative amount of junctional RhoA present (Figure 4l). Here, data suggested

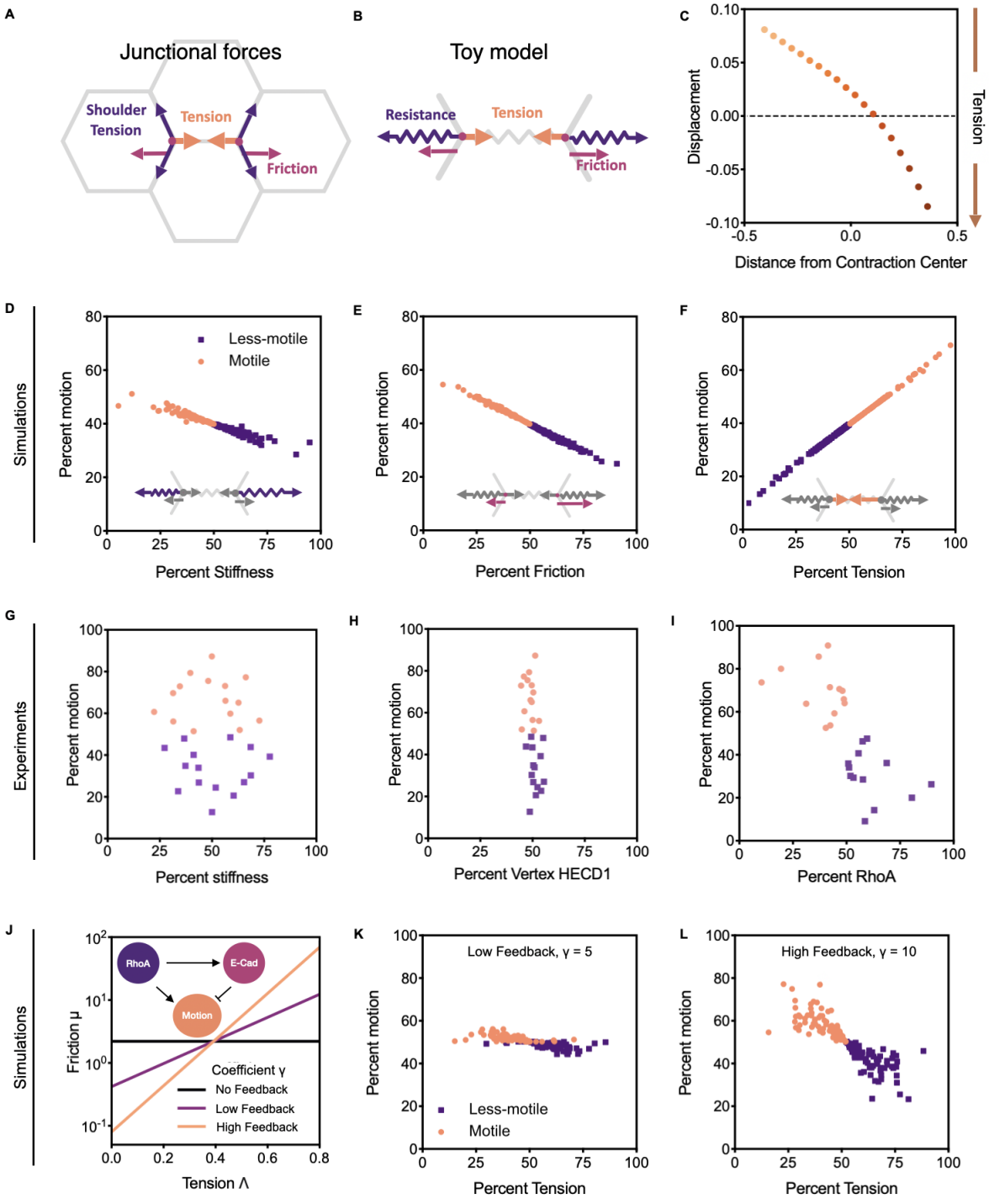

Figure 4.7: Mechanical forces regulating vertex motion asymmetry

Figure 4.7: Mechanical forces regulating vertex motion asymmetry (Continued) A. Schematic of the junctional forces involved in designatinig vertex asymmetry. B. Toy model schematic, showing the main forces involved in driving vertex asymmetry. Shoulder junctions are modeled through a spring-like resistance to motion of the vertices. The junction is modeled as an elastic continuum, where tension and friction may vary along the junction, having difference values at the two vertices. C. Displacement after contraction against initial position along the junction. D. Percent stiffness against percent motion of the whole junction. E. Percent friction against percent motion of the whole junction. F. Percent tension at the vertex against the percent motion of the whole junction. G. Experimental data plotting percent motion as a function of percent stiffness showing no correlation. H. Experimental data plotting percent motion as a function of the normalized E-cadherin intensities at T-10 before optogenetic activation. I. Experimental data plotting percent motion as a function of the normalized distance to RhoA, as calculated in Figure 2E. 1 represents low tension (large distance to RhoA) and 0 represents high tension (close to RhoA activation). J. Friction against tension for different force scales γ. Inlay shows schematic representing feedback between RhoA and E-Cadherin that generates vertex motion. K-L Percent motion against percent tension for γ=5, and γ=10.

that the closer the RhoA was to a vertex, the less it moved, consistent with our data in Fig. 4.3B. This was starkly contrasted to highly motile vertices, which were distal to RhoA regions and experienced little RhoA-mediated tension. Together these data suggest that asymmetries in friction, tension, and stiffness parameters alone were insufficient to explain asymmetries in vertex movement during junction contractions.

Model with feedback between junctional tension and vertex friction - Our experimental observations informed us that vertices with higher recruitment of RhoA moved less (Fig. 4.3), in contrast to simulations which predicted that more tension gave rise to more vertex displacements (Fig. 4.7F). At the same time, less mobile vertices also showed a marked increase in E-cadherin levels (Fig. 4.5). Thus, there may be mechanosensitive recruitment of E-cadherin through increased tension, resulting in an increases cell-cell friction. This is conceptually similar to mechanosensitive frictional drag of focal adhesion complexes, where the friction increases with increasing cell-substrate traction stress [173]. If this feedback between tension and friction were high enough, then an increase in tension would increase friction to such an extent that these vertices would move slower.

To test this model, we allowed mechanosensitive remodeling of friction by tension along

the junction in our continuum model. Again, we varied tension along the junction by setting the tension at each vertex to be a random value sampled from the normal distribution with mean Λ_0 and standard deviation $\Lambda_0/3$, and linearly interpolated tension along the junction. Using a low-force catch bond model, the friction coefficient is given by $\mu = \mu_0 e^{\Lambda\gamma}$, where μ_0 is the friction coefficient at zero tension, and γ is a feedback parameter with γ^{-1} setting the tension scale for mechanosensitive frictional slip (Fig. 4.7J). For $\gamma = 0$ there is no feedback between tension and friction, such that there is increasing motion with increasing tension (Figure 4F). For intermediate feedback strength, $\gamma = 5$, an increased tension was countered by increased friction, resulting in no correlation between relative junctional tension and displacement (Figure 4K). For high feedback between tension and friction, $\gamma = 10$, the increase in friction was high enough to slow down motion at high tension vertices. As a result, we found a negative correlation between vertex tension and motion (Fig. 4.7L), successfully recapitulating the experimental data (Fig. 4.7I). These simulations, coupled with experimental data, indicate that the E-cadherin recruitment at tricellular vertices likely increases local friction coefficient to limit junction contraction in a RhoA-dependent manner.

4.4.5 Local RhoA drives E-Cadherin pooling

Our model uncovers a positive feedback between RhoA activation and E-cadherin recruitment to tricellular vertices, which increases local friction and reduces vertex mobility. To further determine the extent of interdependencies between Rho-mediated E-cadherin recruitment and junction contractility, we used our optogenetic approach to locally activate regions that do not typically experience RhoA activation, as determined by Fig. 4.3D-F. These data revealed that RhoA is stochastically skewed towards one vertex but is typically lower at vertices. As such, we next sought to activate specifically the tricellular vertex to witness any feedback at this region. Vertex activation was insufficient to induce junction contraction, with the vertices exhibiting little to no vertex displacement compared to WT full-length activation (Fig. 4.8A, B). However, tricellular vertex activation did induce a 30% increase

in E-cadherin over a 5-minute activation that diminished with removal of the exogenous RhoA activation (Fig. 4.8A, C). Moreover, we found that the activated vertex experienced a significant increase in E-cadherin intensities compared to the non-activated vertex (Fig. 4.8C). These data indicate that, upon RhoA activation, E-cadherin is concentrated, or pooled, towards the region of activation.

To explore the hypothesis that very local RhoA activation induces E-cadherin pooling, we then activated only the center of the junction (Fig. 4.8D). Activation at the center third of the junction created a contraction whose extent was similar to WT full-length activation. As the center was being activated, there was a noticeable concentration of E-cadherin puncta to the region of activation (Fig. 4.8D). Displacement analysis for the center activation indicated that the contraction was more symmetric, with both vertices moving considerably and relatively evenly upon RhoA activation in the center third of the junction (Fig. 4.8E). However, when the junction was activated in the center third, analysis of the HECD1 fiducial marks revealed that the center of contraction was indeed in the middle of the junction with a mean center of contraction being 0.47 (Fig. 4.8F). These data hint at the possibility that tricellular vertices generate considerable friction during junction contraction, as the lack of activation at vertices produced a symmetric contraction.

To understand the origin of this E-cadherin pooling, we examined junctions activated only at the center third of the junction. We saw E-cadherin pooling upon junctional prGEF recruitment within the activation period (Fig. 4.8G). Here, prGEF recruitment preceded this concentration of E-cadherin, as smaller puncta of E-cadherin coalesced to a concentrated point upon blue light activation (Fig. 4.8G, white arrows). We then measured the fluorescence intensities of both the prGEF and the HECD1 along the junction without the vertices to exclude the contributions of shoulder HECD1 from adjacent cells. This revealed a 15% increase in prGEF intensities compared to HECD1, whose change in intensities was negligible. This led us to a mechanism whereby local, heterogeneous RhoA pulls adhesion molecules from distal regions of the junction to the region of RhoA activation, as analysis of the fluorescence

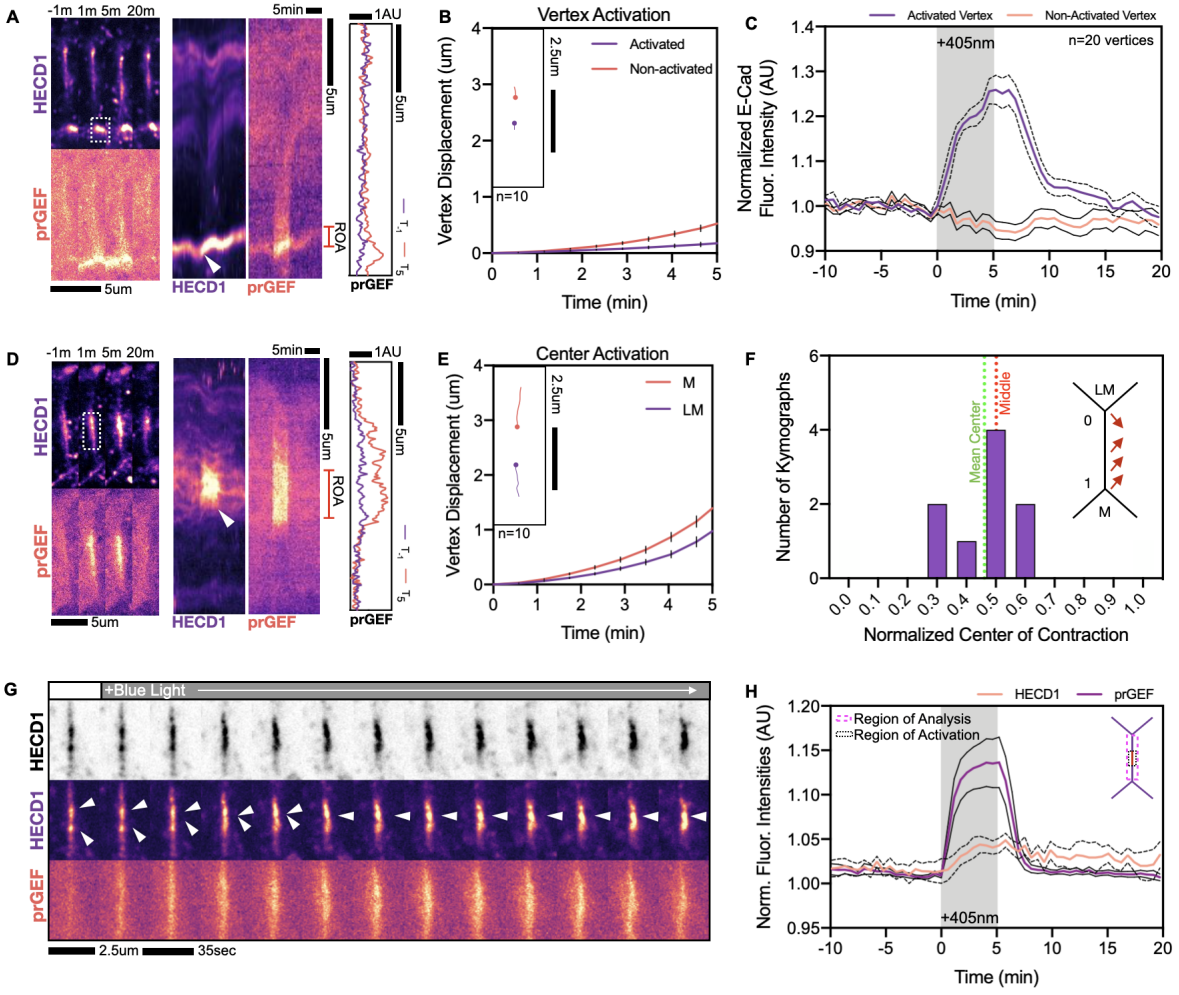

Figure 4.8: RhoA pools E-cadherin to the location of activation. A. Representative image and kymograph of a junction undergoing only vertex activation at the tricellular contact. B. Vertex displacement analysis of vertex activation showing little-to-no vertex motion within the optogenetic activation period. Inlay shows individual vertex tracks for two vertices of the same junction. C. Normalized HECD1 (E-cadherin) fluorescence intensities for vertices during vertex activation between the activated and non-activated vertices. Activated vertices show increases in E-cadherin fluorescence intensities. D. Representative image and kymograph of a junction undergoinig center-junction activation. E. Vertex displacement analysis of center-junction activation showing contractile symmetry is restored. Inlay shows individual vertex tracks for two vertices of the same junction. F. Normalized center of contraction analysis for center-junction activation showing the center of contraction is in the middle of the junction, consistent with where RhoA is activated. G. Representative stills within the optogenetic activation period showing pooling of E-cadherin upon prGEF recruitment. H. Quantification of normalized intensities for HECD1 and prGEF.

intensities shows a consistent mean fluorescence intensity over time for HECD1 compared to the prGEF (Fig. 4.8H). This suggested a possible mechanism by which E-cadherin slides along contracting actin filaments towards RhoA. No new cadherin was recruited to this region, as fluorescence intensities were conserved along the junction over time.

4.5 Discussion

We present here a vertex mechanoresponse that mediates asymmetric junction contraction. We find that this RhoA-dependent contraction occurs uniformly along the junction length, with both the center of contraction and RhoA localization skewed towards the less-motile vertex. Modeling these data, we find that base stiffness, friction, and tension parameters alone cannot successfully recapitulate experimental data. Instead, we find experimentally that contraction coincides with the pooling of E-cadherin to the less-motile vertex to create frictional drag. Modulating this friction either induces symmetry or reduces asymmetry in contraction. We further find that the localization of optogenetic RhoA pools E-cadherin to the region of activation, indicating a novel feedback loop between RhoA-mediated tension and E-cadherin induced friction. Incorporating this feedback circuit into our model, we were able to successfully recapitulate vertex asymmetry, in that less-motile vertices experience greater relative tension in the form of RhoA.

This defines a novel molecular "clutch" model for tricellular contact engagement during junction contractions. In the absence of RhoA activity, or at distal regions with less RhoA, little E-cadherin is recruited to the vertices. When RhoA-mediated tension is applied to the junction, proximal tricellular adhesions undergo a rapid pooling of E-cadherin that restricts contractile motion in a process similar to that of a "frictional slip" seen in focal adhesions. At focal adhesions, traction stress builds along with frictional drag. The frictional slip is then abrogated once a threshold force is reached, thus providing immobilization of a stable adhesion for adhesion growth [173]. We envision a similar mechanism operating at tricellular vertices in that a mechanosensitive rigidity transition of tricellular contacts engages the clutch

to strengthen adhesions under load. This adhesion reinforcement restricts vertex motions asymmetrically, as RhoA-mediated tension is stochastically skewed towards one vertex.

These data beg the question as to how RhoA is stochastically placed along the junction. We believe the junction is split into discrete domains that are primed for RhoA activation. These primed regions could be borne out of heterogeneities in adhesive complexes, which exist as puncta along the junction [170]. For example, lower junctional E-cadherin levels spatially orient medioapical contractile flows to coordinate junction contractions [72]. We similarly see RhoA flares tracking in regions of low E-cadherin, supporting the notion that E-cadherin-depleted domains could specify primed RhoA regions (data not shown). These domains' potential for RhoA activation can be exacerbated by the junctional landscape. The local junction composition, specifically lipid and other protein signaling, could generate these distinct contractile units. Indeed, RhoA can function via a coincidence detection scheme upon cyclic binding to the lipid PIP_2 and the junctional protein Anillin [33]. Protein-lipid microdomains, scattered along the junction, could therefore create a permissive environment for RhoA activation that is necessary for junction contractions. Spatial heterogeneities in adhesion, lipids, and protein localization could therefore be critical in determining which portion of the junction is capable of activating RhoA. Further work is needed to discern what specifies these unique microdomains.

These data have serious implications for the canonical mathematical models of epithelial tissues, those like the vertex model. In traditional vertex models, the tissue is a network of edges and nodes whose geometry and topology depends on active forces. The positions of these vertices anchoring bicellular interfaces are determined by the parameters of interfacial tension and pressure within each cell [4, 90]. Vertices can then move in response to active forces, but the extent of this movement is proportional to the parameters describing vertex friction, shoulder edge tension, and tricellular contact stiffness. Using our toy model, no one single parameter describing friction, tension, or stiffness was able to recapitulate experimental data. Instead, we find that the incorporation of a feedback circuit between RhoA and

E-cadherin successfully modeled vertex asymmetry.

Yet what is the physiological benefit in restricting vertex motion? In the Drosophila Germband, tricellular E-cadherin recruitment is associated with the stabilization of the junctional ratchet. This stabilization ensures progressive interface shortening to facilitate cellular rearrangements [78]. In our optogenetic system, we do not find stable, irreversible contractions at short timescales but rather elastic junctional deformations. As such, it is unlikely that this vertex reinforcement stabilizes junctions, at least in our system. Alternatively, this restriction in vertex motion could maintain a cohesive epithelial layer. Strong contractions, in principle, could compromise intercellular junctions and barrier functions. Indeed, vertices are principal sites of epithelial fracture in highly tensile epithelia [174]. Mechanosensitive reinforcement of vertices could therefore restrict major cell and tissue deformations to maintain tissue homeostasis. This mechanism seems plausible, as RhoA-mediated junctional mechanotransduction is a known regulator of tissue integrity [174].

Most studies of cell shape changes, to date, concern the movement of bicellular interfaces between two neighboring cells. Here, we show that bicellular interfaces and tricellular contacts are decoupled, lending to junctional asymmetry upon contraction. In development, these junctional zones experience spatially distinct contractile flows that drives qualitatively different and rather opposing junctional responses. Medioapical flows to the bicellular region correspond to junction deformations while flows to the tricellular contacts restrict such contractions [64, 78]. We see similar junctional responses by optogenetically activating specific junctional zones, with the region of RhoA activation pooling E-cadherin. Our previous work examining stable junction deformations show that longer optogenetic activations facilitate junction length changes through E-cadherin clustering and internalization [114]. It would be of interest to see how optogenetic activation of these junctional zones at longer timescales would facilitate their remodeling. It is possible that RhoA-mediated E-cadherin pooling along the bicellular zone defines specific contact regions that act as endocytic hubs to facilitate junctional shortening. It is currently unclear if the tricellular zone undergoes similar endocytosis. How endocytosis

is differentially regulated at these junctional zones is an interesting question for future work.

4.6 Methods

Cell culture: E-Cadherin-GFP CRISPR and optogenetic Caco-2 cell lines (generated in Cavanaugh et al., 2020) were cultured in DMEM media (Mediatech, Herndon, VA), and supplemented with 10% Fetal Bovine Serum (Hyclone; ThermoFisher Scientific, Hampton, NH), 2 mM L-glutamine (Invitrogen, Carlsbad, CA), and penicillin-streptomycin (Invitrogen). Cell lines were cultured in a humidified incubator at 37C with 5% CO2.

Live cell imaging:To ensure a confluent and mature epithelial monolayer, Caco-2 cells were plated densely on 2um/ml polymerized collagen gels (unless specified otherwise) coating the bottom of a 4-well Ibidi Chamber (Ibidi). Cells were then allowed to grow for at least 1-2 days to ensure a polarized and confluent monolayer. Ibidi chambers were then placed into a stage incubator with temperature, humidity, and CO2 control (Chamlide TC and FC-5N; Quorum Technologies). All pieces of the stage incubator (stage, adapter, cover, and objective) were maintained at 37C. To analyze RhoA dynamics, 5ug of AHPH RhoA biosensor DNA (Budnar et al., 2019; a kind gift from Alpha Yap) was transfected into E-cadherin CRISPR cells using Lipofectamine 3000 (Invitroogen) at least 24 hours before imaging. For CN03 wash-in experiments, cells were imaged in the 488 and 561 channels every 5 or 8 minutes, until 2 hours of timelapse imaging was completed. At the beginning of imaging, either media or 1ug/ml CN03 was added to the media to document junctional responses. To visualize E-Cadherin in the optogenetic system, we bathed the cells in HECD1 (Abcam) primary and secondary antibody, Alexa Fluor goat Anti-Mouse 647 (Invitrogen), both at a 1:1500 dilution in normal media for at least 24 hours. When applicable, E-cadherin was visualized using DECMA (Abcam) primary and secondary Alexa Fluor Goat Anti-Rat (Invitrogen) antibodies at 1:1500 dilution in normal media for at least 24 hours. Before imaging, cells were washed with PBS and replaced with normal media or media containing chemical perturbations described below. For optogenetic experiments, cells were imaged in the 561 and 647 channel every 35 seconds.

The first 10 minutes was to establish a baseline junctional response before the 5-minute optogenetic activation, with the last 15 minutes documenting junctional relaxation. During the activation period, a region around the junction was manually drawn in MetaMorph and adjusted in real time for illumination by the 405nm laser for 1000ms immediately before the acquisition of each image. Laser power was at 1000AU. For junction and vertex movement analysis, via both CN03 and optogenetic means, we chose to analyze junctions that were distal from cell divisions and/or apoptotic extruding cells to ensure a cohesive monolayer. For picking optogenetic cells, cells were chosen based off of their expression level, which showed junctional recruitment and depletion of the prGEF from the cytosol. All junctions were imaged at the apical plane just below the surface to visualize all vertices and junctional connections.

Drug treatments: Cells were treated with a 1:1500 DECMA antibody treatment 24 hours before experimentation. Optogenetic cells were treated with 25uM ResEcad (Calbiochem) or 100uM NSC23766 (Tocris) 24-48 hours before optogenetic activation. WT Caco-2 cells were treated with 1ug/ml CN03 (Cytoskeleton, Inc) or 1ug/ml C3 Transferase (Cytoskeleton, Inc) for at least 4 hours before fixing and staining to analyze E-cadherin localization. E-cadherin CRISPR cells were imaged upon the exposure to 1ug/ml CN03.

Immunofluorescence: Cells were plated onto polymerized collagen gels coating a Lab Tek II Chamber slide (Thermo Fisher Scientific). Once a confluent monolayer was formed, cells were fixed with 4%PFA with 0.1% Triton X-100 in PBS solution (Corning). Permeabilization was achieved through 0.5% Triton X-100 for 10 min and then cells were blocked with 2.5% BSA and 0.1% Triton X-100 in PBS for one hour. Primary antibody, Paxillin at 1:300 or HECD1 at 1:300, was incubated in blocking solution overnight at 4C and then washed at least 3 times for 20 minutes in 0.1% Triton X-100. Slides were the coated with secondary antibody, Alexa Fluor Goat anti-Mouse (Invitrogen), and phalloidin (ThermoFisher) in blocking solution for one hour. After 3 consecutive 20-minute washes in 0.1% Triton X-100, slide chambers were removed and coated with 20ul ProLong Gold (ThermoFisher Scientific). Slides were then

sealed with glass coverslips before drying and sealing with nail polish. Slides were then stored at 4C.

Microscopy: Optogenetic experiments were performed on an inverted Nikon T-E (Nikon, Melville, NY) with a laser merge module with 491, 561, and 642nm laser lines (Spectral Applied Research, Ontario, Canada) with a Yokogawa CSU-X confocal scanning head (Yokogawa Electric, Tokyo, Japan). The Zyla 4.2 sCMOS Camera (Andor, Belfast, UK) collected the images. Optogenetic activation was achieved using a Mosaic digital micromirror device (Andor) attached to a 405nm laser. Images were collected on a 60X 1.2 Plan Apo water (Nikon) objective. MetaMorph Automation and Image Analysis Software (Molecular Devices, Sunnyvale, CA) controlled all hardware. Fix-and-stain and live-cell imaging of CN03 wash-ins were performed on an LSM 980 system with an Airyscan 2 (Zeiss) detector in super resolution-mode with a 63x NA1.4 oil objective (Zeiss). Microscopy software used was the Zen digital imaging suite (Zeiss).

Image analysis: Vertex displacement and individual vertex traces were acquired by manually tracking each vertex in a vertex pair using the Manual Tracking tool in Fiji (Schneider et al., 2012). Junction lengths were analyzed by manually measuring in each frame the junction length using the free hand line tool in FIJI software. Junction kymographs were generated with a python script written in FIJI to reconstruct user-drawn line segments along the junction proper. Kymographs were made from unregistered image stacks to preserve asymmetry in junction contraction. Linescans of activated regions and E-cadherin along the junction were taken using the Plot Profile tool of a hand-drawn line along the junction in FIJI. Linescans were taken before optogenetic activation and after 5 minutes of activation. Junction intensity profiles were then normalized for the junction length from 0 to 1. Vertex fluorescence HECD1 intensities were calculated by drawing a circle around the vertex region in each frame and measuring the intensities over the time course using the FIJI intensity analysis tool. Contracted length was calculated by dividing the length of the junction at T=5 divided by the length at T=0 during optogenetic activation. Tricellular enrichment of

E-cadherin was calculated by taking the ratio of the tricellular E-cadherin region proximal to the vertex contact and dividing it by the bicellular junction length in between two vertices. This intensity measurement was done by drawing a region proximal to the vertex to analyze tricellular E-cadherin using the Intensity analysis tool, and then calculating the intensity by drawing a box region around the bicellular interface. To analyze focal adhesion size and number, the paxillin channel was thresholded and made into a binary mask to calculate the area of focal adhesions within a cell, as indicated by boundary edges seen from apical actin staining. The binary mask was then overlaid onto the paxillin channel to segment the image and calculate the area of paxillin with a threshold of 0.25um2 and also the number of focal adhesions within that cellular region identified by apical actin staining. Percent movement was calculated as the displacement of each vertex from the original vertex position in a kymograph divided by the sum of both vertex displacements. Contractile uniformity within each junction was analyzed by manually tracking E-cadherin puncta in each kymograph using the paintbrush tool in FIJI. The maximal displacement of each contracting E-cad puncta as a function of the position along the junction was found and linearly fit using the MATLAB fit function. The kymograph's center of contraction was determined by the root value of the linear fit, and the center of contraction was then normalized so that the position of the less-motile vertex was 0 and the more motile vertex as 1, meaning the center of the junction would be the position of 0.5. RhoA localization along the junction was found by averaging the AHPH RhoA intensity at the final five timepoints within the kymograph and fitting it to a gaussian using the Matlab fit function. The junction position of the gaussian peak was determined to be the center of RhoA localization and normalized.

Model implementation: The junction is model by an elastic continuum with Young's modulus E, RhoA induced contractility $\lambda(x)$ and friction $\mu(x)$, which my both vary along the junction. The shoulder junctions are modelled as provided a simple spring like resistance to deformation, with stiffness k. To numerically solve the model for the junction, we discretize the system into n equally spaced points along the junction, x_i, with tension

λ_i and friction coefficient μ_i. The discretized equations of motion are given by: $\mu_0 \dot{x}_0 = \frac{E(x_1 - x_0 - l)}{l} + \lambda_1 - kx_1$, $\mu_i \dot{x}_i = \frac{E(x_{i+1} - x_{i-1} - 2l)}{l} + \lambda_{i+1} - \lambda_{i-1}$, for i $= 1, 2, \ldots,$ n $- 1$, $\mu_n \dot{x}_n = \frac{E(x_n - x_{n-1} - l)}{l} - \lambda_{n-1} + k\,(x_n - 1)$ where $l = \frac{1}{n}$ is the distance between position along the junction. The equations are then integrated numerically over time using the python package scipy. For each set of simulations, 100 samples are taken. The default model parameters are given in the table below. These values are used unless otherwise stated. Parameters are fit by comparing simulations to 5-minute contraction data, and 20-minute contraction data at half-light intensity from [114], by applying half the tension.

Parameter	Symbol	Value
Shoulder stiffness	k	1
Junction Young's Modulus	E	1
Friction Coefficient	μ	2.5/min
Tension	λ	0.4
Number of points	n	21

Calculating shoulder stiffness: To estimate the mechanical resistance to motion from the shoulder junctions, we use a simple line tension model of the junctions. Assuming that line tension from the junctions is under force balance, we may calculate the relative tensions from the force balance and derive an effective mechanical energy of the system as the central junction changes length. From this, the second derivative gives us the mechanical stiffness from the shoulder junctions. Let λ be the tension of the central junction, λ_1 and λ_2 the tensions of the two shoulder junctions, and θ_1 and θ_2 be the angles between the shoulder junctions and the central junction, and l_1 and l_2 be the initial shoulder junction lengths. By force balance we have: $\lambda_1 \sin\theta_1 = \lambda_2 \sin\theta_2$ and $\lambda = \lambda_1 \cos\theta_1 + \lambda_2 \cos\theta_2$ in the x and y directions, respectively, which give the relative tensions. Next, we calculate the effective resistance from the shoulders by considering the second derivative of the energy with respect to the junction length, y. We can write the shoulder junction lengths as $L_i(y) = \left(l_i^2 \sin^2\theta_i + y^2\right)^{\frac{1}{2}}$ with first derivative $\frac{dL_i}{dy} = \frac{y}{L_i}$ and second derivative $\frac{d^2 L_i}{dy^2} = \frac{\sin^2\theta_i}{L_i}$ Thus, the mechanical

energy $E = \lambda_1 L_1 + \lambda_2 L_2 - \lambda y$ has second derivative at the initial position of $\frac{d^2E}{dy^2} = \frac{\lambda_1 \sin^2\theta_1}{l_1} + \frac{\lambda_2 \sin^2\theta_2}{l_2} = k$, the effective shoulder stiffness.

4.7 Acknowledgements

KEC acknowledges an National Academies of Sciences Ford Foundation Fellowship, HHMI Gilliam Fellowship, and NIH training grant GM007183. MLG is supported by funding from NIH RO1 GM104032 and ARO MURI W911NF1410403. This work was partially supported by the UChicago MRSEC, which is funded by the National Science Foundation under award number DMR-1420709. MFS acknowledges an EPSRC funded PhD studentship. SB is supported by funding from the Royal Society (URF/R1/180187) and HFSP (RGY0073/2018). SB and ASY were supported by grants and fellowships from NHMRC Australia (GNT1123816, Fellowship1136592) and the Australian Research Council (DP19010287).

CHAPTER 5

THESIS SUMMARY AND CONCLUSIONS

5.1 Summary

5.1.1 An Optogenetic Paradigm for Junction Length Maintenance

Kinematic observations of junction deformations in response to stress have produced the bulk of information regarding the molecular origins of contractile forces directing morphogenesis. To date, most studies have relied on the visualization of Rho's downstream effectors to correlate mechanochemical signaling with cell shape changes [59, 62, 64, 67, 69, 74]. Fluorescence receovery after photobleaching experiments have revealed that NMII is stabilized at the cortex in regions of increased mechanical tension, offering a positive feedback loop in the generation of stable junction contractions at DV interfaces [67]. Here, NMII's phosphorylation state ensures progressive interface shortening [69]. These and other data support the idea that spatiotemporal increases in RhoA-mediated mechanical tension drive stable junction deformations within the ratchet [102]. However, much of this literature has used genetic or pharmacological means to globally inhibit Rho-mediated junction tension. These perturbations often destroy any spatiotemporal feedbacks of the actomyosin network's response. New methods are therefore needed to directly modulate the spatiotemporal, tensional changes that drive morphogenetic processes.

Optogenetics is an emerging and powerful method that controls protein localization with focused light [175]. Light-mediated protein dimerization in distinct subcellular compartments can spatially activate endogenous RhoA to test morphogenetic contractile zones' function in regulating cell-cell junction viscoelasticity and deformability. A number of two-component optogenetic systems have been employed historically [94, 110–116]. These systems have successfully studied the nature of cell and tissue mechanics both in vivo and in vitro. However, they have not had the spatial resolution to isolate single junctions to probe their

underlying mechanics.

Here, I present, to my knowledge, the first optogenetic system that has targeted cell-cell interfaces to examine their mechanics. This system has high temporal resolution compared to most other systems, with full recruitment and dissipation occuring within 30-60 seconds of light activation. Upon activation, the junction rapidly contracts within less than a minute of experiencing heightened RhoA. The junction shows a robust contraction with even the center third of the junction being illuminated. This contraction is dependent on RhoGEF recruitment and subsequent RhoA activation, as titrating the light reduces the initial strain values. As such, this system is powerful, as it can be used to study the effect of localization, strength, and duration of RhoA's signal in regulating junction length.

5.1.2 Adaptive Junction Mechanics

I demonstrate in Chapter 3 a stress dependence for irreversible junction deformations. Here, junctions behaved elastically at short timescales while at longer timescales, the junctions exhibited a surprising viscoelastic response in which the junctions exhibited a new equilibrium length upon RhoA removal. By titrating the light to reduce the initial strain values and Λ_a, the junctions behaved akin to an elastic material, suggesting a thresholded viscoelastic response of intercellular junctions. These data deviated from the predictions of the canonical Vertex model for epithelium. Similarly, treating junctions as Kelvin-Voigt or Maxwell materials failed to capture the experimental junction response in this system.

To account for the experimental data, two key adaptive mechanisms were necessary in modeling junctional mechanics: continuous junctional strain relaxation and thresholded tension remodeling. Tension remodeling only above a critical strain threshold enables irreversible deformation for sufficiently strong or sustained activation of force. Such a strain threshold allows for a filter of small amplitude fluctuations in intracellular force production, mechanically buffering the system. For a junction whose material components, like F-actin, undergo turnover, old strained material will be replaced by new, unstrained material.

Junctional strain will therefore relax. Continuous strain relaxation at junctions allows the system to gradually lose memory of its mechanical deformation. One consequence of this is that long contractions only remodel junctions up to a limit, as strain relaxation prevents further remodeling.

These optogenetics data support the existence of a mechanical feedback between junctional strain and tension, elucidating a robust mechanism to direct morphogenesis, while strain relaxation via actomyosin modulation regulates tensional homeostasis. We find that strain triggers remodeling of junctional tension. Tension then induces strain on the junction, which is continuously relaxed, limiting the amount of remodeling under long contractions (Fig. 5.1). Active tension remodeling therefore enables viscoelasticity in the Vertex model. This is in line with recent work documenting a more active junctional viscoelasticity [105, 106]. Together, these findings on junctional deformability point to a new, emerging phenomenon: adaptive junction mechanics.

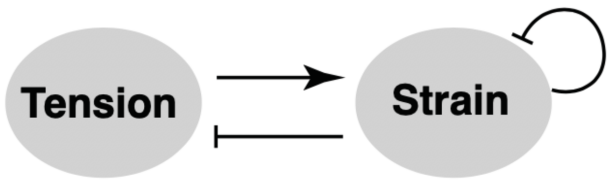

Figure 5.1: Schematic of tension remodeling feedback.

5.1.3 Adaptive Mechanics Capture Ratcheting Behavior

Adaptive mechanics provide key insight into why actomyosin pulses are often oscillatory in nature. Post-contraction, there is a period of residual positive strain that makes the system refractory to any following input, enabling frequency-dependent modulation of RhoA signal and subsequent junction length changes. Resting periods therefore allow strain equilibration such that a new cycle of contraction can reach the critical strain value. Indeed, shorter rest periods show reduced junction length changes and secondary contractions compared to rest periods that allow for the residual strain to reach zero. As a result, pulsatile contractions

with sufficient periods of quiescence enable large-scale irreversible deformations via junctional ratcheting, thus recapitulating the mysterious ratcheting phenomenon commonly seen in development [66, 145, 163, 176].

5.1.4 Mechanosensitive Endocytosis and Cell Shape Stabilization

Contractility has been examined extensively as a key regulator of T1 transitions within the Vertex model. And yet, T1 transitions provide an extreme example of a topological transition involving decreasing membrane surface area. Until now, the data in the literature was rather correlative in that contractility and cellular shape changes coincided with endocytic events [66, 75]. The degree to which any mechanical and endocytic pathways coordinate during morphogenesis has remained unclear. My study provides definitive proof that RhoA induces endocytosis of junctional material across a strain threshold. Depending on the nature of force in the system, these RhoA fluctuations can either maintain junctional homeostasis or drive significant morphogenetic length changes. In essence, cells can sense their strain and modulate resulting tensional phenotypes via endocytosis to dissipate contractile stress. Together these data offer a fascinating new concept in adaptive junction mechanics mediated by the endocytic turnover of junctional components.

5.1.5 Asymmetric Junction Contraction Mediated by RhoA

I describe in Chapter 4 the discovery of a molecular clutch operating at tricellular contacts to reinforce vertices upon increases in tensional load. Such a mechanoresponse drives vertex asymmetry upon contraction, giving rise to a motile and less-motile vertex. Here, E-cadherin is both pooled towards regions of high tension that occur stochastically and asymmetrically along the junction length. Proximal RhoA therefore drives a reinforcement of vertex E-cadherin to limit vertex motion while pooling interfacial E-cadherin to the location of activation. This molecular clutch likely represents an evolutionarily conserved mechanism for cellular-based adhesions, since this mechanoresponse is similar to that of focal adhesion complexes, which

also experience a tension-dependent engagement and stabilization of basal substrate adhesive complexes [173]. As such, adhesion growth and immobilization in response to force seem to be a common feature of cells and tissues to sense and respond to environmental cues.

Modeling these data, together we found that canonical models of epithelial tissues were unable to explain experimental results. Individual parameters including tension, friction, and stiffness alone were unable to fully account for vertex asymmetry. Experimentally, RhoA increased junctional tension to facilitate vertex motion while E-cadherin opposed this motion via frictional drag. RhoA, however, also pooled E-cadherin to increase that frictional load (Figure 5.2). This led us to discover a functional circuit between RhoA and E-cadherin to mediate asymmetric vertex motion. The incorporation of this feedback was critical in recapitulating acquired data.

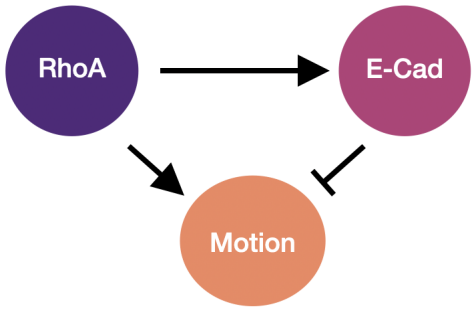

Figure 5.2: Schematic of the feeedback model between RhoA and E-cadherin.

5.1.6 Vertex Models of Epithelial Tissues

These data in Chapters 3 and 4 call into question the efficacy of common mathematical models of junction mechanics. These models, which are sufficient to recapitulate global tissue order and geometry during homeostasis and certain morphogenetic processes, seem to lack critical parameters modeling mesoscale junctional dynamics described here. As such, this body of work has considerably improved the validity of these applied mathematical models to truly recapitulate junctional phenotypes resulting from applied RhoA-mediated

tension. The incorporation of various feedback mechanisms among junction tension, strain, and friction have enhanced currently available models. These data further uncover the intricate mechanisms by which junctions operate to maintain order or undergo significant shape changes. Indeed, it seems very plausible that such junctions must have adaptive mechanisms to ensure the correct morphogenetic or homeostatic program takes place. These adaptive mechanisms were discovered by altering the spatiotemporal nature and magnitude of signal driving intercellular stresses, further demonstrating the power of optogenetics in deciphering morphogenetic processes.

5.2 Future Directions

5.2.1 Characterizing the Initiation of Junction Contraction

An immediate implication of this work is how mechanochemical signaling underlies proper cell and tissue mechanics. It is unclear how the strength of active RhoA confers the rate and amount of junction contraction. My optogenetic system allows for the direct modulation of the amount of RhoA activation by varying the light intensities (Fig. 3.5). I find that light intensities ranging from 750-1000AU produce an initial contraction, L_5/L_0, of approximately 0.8. However, at a lower light intensity of 500AU, the initial contraction decreases so that L_5/L_0 increases to 0.89. One implication of these data is that there is a minimum level of RhoA activity that is necessary to induce a strong contraction, essentially providing for a binary response that is triggered upon a threshold RhoA. Junction contractions may therefore be buffered to small changes in RhoA activity. It is also possible that the system is limited in its contraction by the saturation of junctional NMII. As such, it would be worthwhile to visualize RhoA and downstream actomyosin contractile arrays upon blue light activation to document their stoichiometry. Further work exploring the dosage of light intensity on RhoA-mediated junction contraction is therefore needed.

The perijunctional actomyosin network must dynamically contract, yet remain linked to

junctional AJs for force production and propagation across an epithelium [71, 76]. These data propose a molecular clutch mechanism in which actomyosin networks must be engaged at adhesive complexes for proper junction contraction. Indeed, disruption of AJs causes cellular actomyosin networks to contract away from the cell periphery, resulting in altered force generation [177]. When the clutch is engaged, proper junction contraction can occur. The molecular clutch can be affected by the level of actin crosslinkers, the cadherin-catenin complex, or other peripheral AJ proteins. Some of the proteins implicated in the modulating junctional tensions include afadin [71], alpha-catenin [178], and alpha-actinin [179]. It is therefore tempting to speculate as to these proteins' functions in regulating the contractile optogenetic phases seen in Chapter 3. Genetic mutations to tune the level of actin engagement may therefore result in altered contractile strain and junction rest lengths, since we have shown that the junction contains an inherent strain threshold.

Engagement of the molecular clutch must be coupled with asymmetric force production at adhesive complexes. The mechanical model suggests that initial contraction is sensitive to base epithelial tension, dictated by adhesion levels (Fig. 3.4). However, it is unknown if the levels and types of various cell-cell adhesions impact the rate or extent of junctional contraction and remodeling. Recent data has shown that increasing E-cadherin at vertical junctions reduces the junctional ratchet, suggesting that E-cadherin actually resists contractile deformations [78]. Similarly, knockdown of tight junction proteins ZO-1/ZO-2 elevated RhoA-mediated junctional contractility, suggesting that ZO family proteins work to reduce tension upon contraction [77]. It is therefore of interest to modulate the levels and types of junctional components to witness how adhesive drag influences contractile phenotypes. It would be compelling to witness a dose-dependent response in junctional contraction as a function of adhesion levels.

5.2.2 Dissecting the Mechanism of Junction Remodeling

I find that heightened and sustained RhoA-mediated contraction induces dynamin-dependent junction remodeling (Fig. 3.9). Dynamin has overlapping molecular functions in both Clathrin- and Caveolar-mediated endocytosis [180]. Here, dynamin operates in vesicular scission to cleave the membrane neck of endocytic pits [181]. While these endocytic modes' cargo is diverse, junctional E-cadherin is often trafficked [182], lending to the possibility that both mechanisms operate at the AJ to regulate E-cadherin levels. As such, it is important to discern which mechanism operates at the junction for length regulation. Whether E-cadherin endocytosis is initiated by clathrin or caveolin subunits depends in part on the activation of upstream Rab regulators and the presence of various adaptor proteins [81]. The upstream regulation, and what triggers the initiation of either endocytic module during junction length changes, also remains unknown. Further work is therefore necessary to elucidate the endocytic machinery under RhoA-mediated control.

Formins have been implicated in the regulation of E-cadherin endocytosis [75]. Here, Drosophila RhoGEF2-mediated activation of the formin Diaphanous (Dia) was shown to concentrate and package E-cadherin molecules for their ultimate internalization upon junction contraction. Data in Chapter 3 (see Fig. 3.9) directly support this view, in that the pan-formin inhibitor SMIFH2 completely abolished E-cadherin punctae and subsequent junction length remodeling. Since this compound inhibits all formin activity, it is therefore necessary to confirm which formin is acting at the ZA for E-cadherin clustering and junction length regulation. One promising candidate is Dia1, which controls junctional tension in a RhoA-dependent manner at the ZA in Caco-2 cells [169]. However, humans have fourteen other formins, one of which may be responsible for these remodeling phenotypes [183]. It is also interesting to consider the mechanism by which E-cadherins cluster into larger macromolecular assemblies and the role of formin-mediated actin polymerization in this process. Whether or not there is a critical threshold amount for E-cadherin internalization is subject to further investigation, as well.

5.2.3 Examining Mechanical Stress Dissipation

Stress dissipation can operate at the level of tension-sensitive actin polymerization and depolymerization kinetics. At the filament scale, mechanical strain accelerates the severing and turnover of F-actin filaments for network fluidization [158, 184]. Since AJs contain a rich perijunctional actomyosin belt, it is no surprise that actin depolymerization agents play an important role in their contractile responses. AIP1, a cofactor of the actin severing protein Cofilin, localizes to tension-bearing shrinking junctions within T1 transitions of the Drosophila wing disc [185]. Here, AIP1/Cofillin is responsible for the remodeling of the perijunctional actomyosin ring to facilitate vertex formation. Similar depletion of Cofilin results in separations of the contractile machinery from the cell periphery, abolishing cell shape changes within the Drosophila mesoderm [177]. It would be of interest to explore the role of actin depolymerization in my optogenetic system to see if it underlies strain relaxation. It is plausible that the dosage of depolymerizing factors dictates the extent to which new rest lengths are stabilized. The ratchet's rest period could also be tuned based on these turnover dynamics, resulting in extended or shortened periods of strain relaxation.

My data suggest a mechanism by which increased mechanical tension contracts the junction, generating regions of slackened and locally curved plasma membrane for internalization. BAR family proteins are well known sensors of plasma membrane curvature and function in force-dependent AJ remodeling [186]. BAR proteins therefore generate a novel mechanotransduction mechanism via plasma membrane deformation that is independent of the canonical tension-induced signaling from conformational changes within the cadherin-catenin complex [187]. Interestingly, many BAR proteins control the activity of both Rho GTPases and endocytic regulators, thus connecting membrane deformations to membrane trafficking and cytoskeletal remodeling [188, 189]. These BAR proteins may underlie the feedbacks between junction tension and strain, as BARs can locally reduce RhoA concentrations by directly binding GTP-RhoA and recruiting RhoGAPs [190]. As such, RhoA-mediated compression of the membrane and recruitment of BARs can locally reduce RhoA signaling to maintain tensional

homeostasis. Whether and how BAR proteins are required for this stress dissipation is an important question for further work.

It is interesting to speculate as to how macromolecular protein assemblies translate into the tissue-scale viscoelastic behaviors. For instance, focal adhesion-anchored actin bundles, or stress fibers, show a zyxin-dependent elasticity upon RhoA-mediated contraction [113]. Here, zyxin is recruited for stress fiber repair and maintenance. Not only is zyxin binding proportional to the amount of mechanical force, but its stability at substrate adhesive plaques is also tension-dependent. Zyxin, while being best known for mediating cell-substrate interactions, is present at AJs and tunes actin assembly here [191, 192]. Similar members of the zyxin family and LIM domain-containing proteins are recruited to AJs in a tension-dependent manner during CE [176]. Whether zyxin directly influences the elasticity of the perijunctional actomyosin belt is currently unknown. Exploring zyxin's role during optogenetically-induced contraction and resulting relaxation would therefore uncover the molecular basis of junctional elasticity. It would further demonstrate how microscopic protein interactions translate into macroscopic tissue-scale viscoelasticity necessary to drive morphogenetic processes.

5.2.4 Exploring Vertex Asymmetries

I find that heterogeneous RhoA flares persist over the course of junction shortening in CN03 treatment. A significant, open question arising from Chapter 4 is what specifies these heterogeneous regions of RhoA that drive contractile asymmetries. These data suggest that the junction contains regions that are "primed" for RhoA activation and are stochastically placed along the junction proper, perhaps due to the local junctional landscape. Preliminary data shows RhoA flares track in regions of low E-Cadherin and concentrated plasma membrane, defining distinct domains along the junction length. RhoA contractile regions could therefore arise from local lipid signaling, which has been shown to influence RhoA kinetics in complex with Anillin via a coincidence detection scheme [33]. Indeed, depletion of PIP_2 via Neomycin treatment depletes junctional RhoA and halts any junction contractions upon CN03 treatment

(data not shown). From these data, a mechanism could exist whereby local pooling of PIP_2 and Anillin create permissive environments for RhoA activation to facilitate junction shortening. As such, it will be of interest to further explore the nature of PIP_2 and Anillin localization and signaling during optogenetic activation.

I find that bicellular interfaces and tricellular contacts define almost opposing contractile units during junction contraction. How these two domains coordinate during junctional remodeling seen in Chapter 3 remains unknown. One of the most compelling pieces of data examining junctional asymmetries is the systematic activation of regional junctional zones, specifically the bottom half, vertex, and center zones. These data support the notion that asymmetric RhoA mediates contractile asymmetry and the pooling of E-Cadherin to the region of activation. It would be interesting to see how activation of these junctional zones mediates junction length remodeling and ratchet stabilization with longer activation times. It is feasible to imagine a situation where local E-Cadherin clustering and pooling defines specific contact regions that act as endocytic hubs. This would indicate that the specific RhoA-primed region would mark the location of junctional removal for stress dissipation.

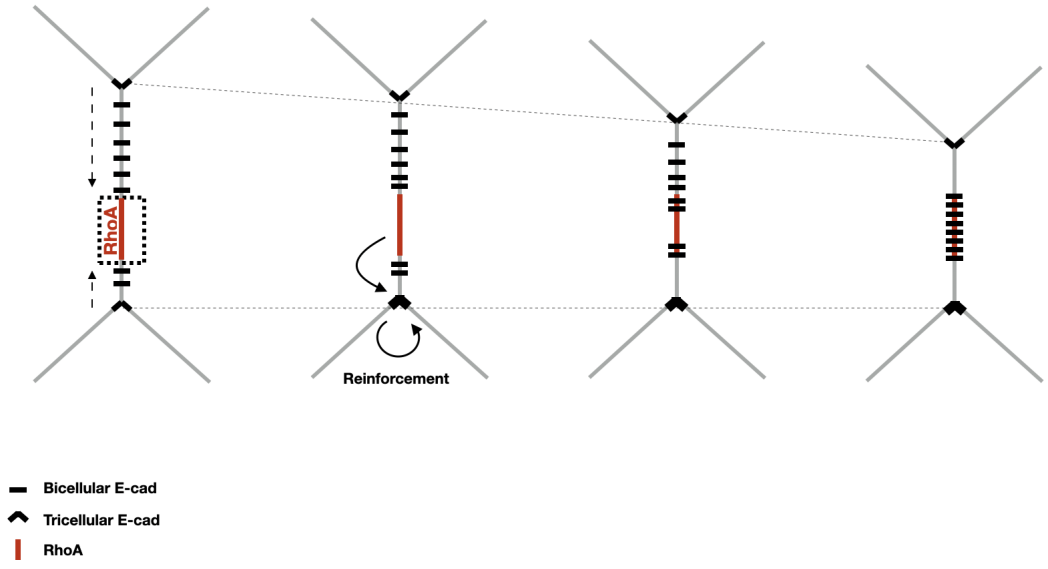

Figure 5.3: Schematic of the molecular clutch model reinforcing tricellular contacts.

Tricellular and bicellular contacts represent two distinct contractile units that sense and

respond to force. Data suggest that adhesions are highly dynamic along bicellular interfaces compared to tricellular contacts. As I see a conservation of interfacial E-cadherin even through optogenetic prGEF recruitment, this suggests that no new E-cadherin is being recruited to junction in response to RhoA. As such, I envision a mechanism whereby E-cadherins at the apical adhesion belt slide along actin filaments, which are contracting via RhoA activation. This local contraction depletes E-cadherin from distal interfacial junctional regions, thereby conserving the amount of E-cadherin at the junction (Figure 5.3). Currently, the nature of E-cadherin-mediated friction at the vertex is unclear. We see a local reinforcement of the vertex cadherins, suggesting that local tension induces the pooling of E-cadherin to tricellular contacts. That these flows are restricted to the vertices suggest an immobilization and stabilization of cadherins at this region. Interestingly, tricellular contacts represent a junctional zone that is compositionally unique compared to the bicellular interface. Here reside large proteins that are only found at tricellular contacts. These proteins include tricellulin and angulin, for example, which seal the paracellular space at the vertex region [193]. These large proteins could restrict E-cadherin flows, creating an almost bulky zone of heightened adhesion that restricts vertex motion. As such, it would be of interest to explore the nature of these tricellular proteins and their influence on vertex asymmetry. It would be very compelling to reduce these proteins' levels and witness symmetry or acceleration in contraction.

5.3 Outlook

Mechanochemical signaling is highly dynamic, with spatiotemporal RhoA pulses and flows mediating cell and tissue morphogenesis. To date, elucidating the role of mechanochemical RhoA signaling has been difficult, as most perturbations disrupt global mechanochemistry. As such, new techniques are necessary to probe the effects of mechanical forces in both space and time. Here, I detailed the use of optogenetics to control subcellular RhoA activity in model epithelia. These optogenetic tools for cell culture offered a means to advance our

understanding of junction mechanics, further testing and enhancing canonical models of epithelia to discern the nature of forces that drive cellular shape. A key finding of the work presented here is that commonly used mathematical models seem incomplete, and require additional feedback parameters to recapitulate experimental data detailed above. Specifically, feedback between 1) tension and strain and 2) tension and friction mediate our observed junctional phenotypes in response to spatiotemporal RhoA activity. Optogenetic control of RhoA made the discovery of these circuits possible. Such a bottom-up approach offers a minimal system in which to recreate morphogenetic processes seen in development to explore their underlying mechanisms. Still, questions remain about the mechanism behind RhoA-mediated cellular shape changes. The platform presented here offers a unique, minimal, and advantageous system to answer these remaining questions. As such, it will be exciting to witness the exploration of mechanical forces in morphogenesis in the future.

BIBLIOGRAPHY

1. Lecuit, T., Lenne, P.-F. & Munro, E. Force Generation, Transmission, and Integration during Cell and Tissue Morphogenesis. *Annual Review of Cell and Developmental Biology* **27,** 157–184. https://doi.org/10.1146/annurev-cellbio-100109-104027 (2019) (2011).

2. Lecuit, T. & Mahadevan, L. Morphogenesis one century after On Growth and Form. en. *Development* **144.** Publisher: Oxford University Press for The Company of Biologists Limited Section: EDITORIAL, 4197–4198. ISSN: 0950-1991, 1477-9129. https://dev.biologists.org/content/144/23/4197 (2020) (Dec. 2017).

3. Thompson, D. W. *On Growth and Form* en. ISBN: 9780521437769 9781107325852 Library Catalog: www.cambridge.org Publisher: Cambridge University Press. July 1992. /core/books/on-growth-and-form/5E06D10C10D0F0124A32E4B93B11DB4A (2020).

4. Fletcher, A. G., Osterfield, M., Baker, R. E. & Shvartsman, S. Y. Vertex Models of Epithelial Morphogenesis. en. *Biophysical Journal* **106,** 2291–2304. ISSN: 00063495. https://linkinghub.elsevier.com/retrieve/pii/S0006349513057949 (2019) (June 2014).

5. Abzhanov, A. The old and new faces of morphology: the legacy of D'Arcy Thompson's 'theory of transformations' and 'laws of growth'. en. *Development* **144.** Publisher: Oxford University Press for The Company of Biologists Limited Section: REVIEW, 4284–4297. ISSN: 0950-1991, 1477-9129. https://dev.biologists.org/content/144/23/4284 (2020) (Dec. 2017).

6. Jaffe, A. B. & Hall, A. RHO GTPASES: Biochemistry and Biology. *Annual Review of Cell and Developmental Biology* **21,** 247–269. https://doi.org/10.1146/annurev.cellbio.21.020604.150721 (2020) (2005).

7. Arnold, T. R., Stephenson, R. E. & Miller, A. L. Rho GTPases and actomyosin: Partners in regulating epithelial cell-cell junction structure and function. en. *Experimental Cell Research. Cell Sensing and Signaling via Cell-Cell Adhesion* **358,** 20–30. ISSN: 0014-4827. http://www.sciencedirect.com/science/article/pii/S0014482717301829 (2020) (Sept. 2017).

8. Cook, D. R., Rossman, K. L. & Der, C. J. Rho guanine nucleotide exchange factors: regulators of Rho GTPase activity in development and disease. *Oncogene* **33,** 4021–4035. ISSN: 0950-9232. https://www.ncbi.nlm.nih.gov/pmc/articles/PMC4875565/ (2019) (July 2014).

9. Bos, J. L., Rehmann, H. & Wittinghofer, A. GEFs and GAPs: Critical Elements in the Control of Small G Proteins. *Cell* **129,** 865–877. ISSN: 0092-8674. http://www.sciencedirect.com/science/article/pii/S0092867407006551 (2019) (June 2007).

10. Cherfils, J. & Zeghouf, M. Regulation of Small GTPases by GEFs, GAPs, and GDIs. *Physiological Reviews* **93,** 269–309. ISSN: 0031-9333. https://www.physiology.org/doi/full/10.1152/physrev.00003.2012 (2019) (Jan. 2013).

11. Pollard, T. D. Actin and Actin-Binding Proteins. en. *Cold Spring Harb Perspect Biol* **8,** a018226. ISSN: 1943-0264. http://cshperspectives.cshlp.org/lookup/doi/10.1101/cshperspect.a018226 (2020) (Aug. 2016).

12. Dominguez, R. & Holmes, K. C. Actin Structure and Function. *Annual Review of Biophysics* **40.** _eprint: https://doi.org/10.1146/annurev-biophys-042910-155359, 169–186. https://doi.org/10.1146/annurev-biophys-042910-155359 (2020) (2011).

13. Blanchoin, L., Boujemaa-Paterski, R., Sykes, C. & Plastino, J. Actin Dynamics, Architecture, and Mechanics in Cell Motility. en. *Physiological Reviews* **94,** 235–263. ISSN: 0031-9333, 1522-1210. https://www.physiology.org/doi/10.1152/physrev.00018.2013 (2020) (Jan. 2014).

14. Floyd, C., Papoian, G. A. & Jarzynski, C. Quantifying dissipation in actomyosin networks. *Interface Focus* **9.** ISSN: 2042-8898. https://www.ncbi.nlm.nih.gov/pmc/articles/PMC6501337/ (2020) (June 2019).

15. Hartman, M. A. & Spudich, J. A. The myosin superfamily at a glance. en. *J Cell Sci* **125.** Publisher: The Company of Biologists Ltd Section: Cell Science at a Glance, 1627–1632. ISSN: 0021-9533, 1477-9137. https://jcs.biologists.org/content/125/7/1627 (2020) (Apr. 2012).

16. Sweeney, H. L. & Houdusse, A. Structural and Functional Insights into the Myosin Motor Mechanism. *Annual Review of Biophysics* **39,** 539–557. https://doi.org/10.1146/annurev.biophys.050708.133751 (2020) (2010).

17. Geeves, M. A. Review: The ATPase mechanism of myosin and actomyosin. en. *Biopolymers* **105.** _eprint: https://onlinelibrary.wiley.com/doi/pdf/10.1002/bip.22853, 483–491. ISSN: 1097-0282. https://onlinelibrary.wiley.com/doi/abs/10.1002/bip.22853 (2020) (2016).

18. Houdusse, A. & Sweeney, H. L. How Myosin Generates Force on Actin Filaments. English. *Trends in Biochemical Sciences* **41.** Publisher: Elsevier, 989–997. ISSN: 0968-0004. https://www.cell.com/trends/biochemical-sciences/abstract/S0968-0004(16)30152-9 (2020) (Dec. 2016).

19. Van Roy, F. & Berx, G. The cell-cell adhesion molecule E-cadherin. en. *Cell. Mol. Life Sci.* **65,** 3756–3788. ISSN: 1420-9071. https://doi.org/10.1007/s00018-008-8281-1 (2020) (Dec. 2008).

20. Shapiro, L. & Weis, W. I. Structure and Biochemistry of Cadherins and Catenins. *Cold Spring Harb Perspect Biol* **1.** ISSN: 1943-0264. https://www.ncbi.nlm.nih.gov/pmc/articles/PMC2773639/ (2020) (Sept. 2009).

21. Charras, G. & Yap, A. S. Tensile Forces and Mechanotransduction at Cell–Cell Junctions. English. *Current Biology* **28.** Publisher: Elsevier, R445–R457. ISSN: 0960-9822.

https://www.cell.com/current-biology/abstract/S0960-9822(18)30157-X (2020) (Apr. 2018).

22. Ratheesh, A. *et al.* Centralspindlin and alpha-catenin regulate Rho signalling at the epithelial zonula adherens. en. *Nature Cell Biology* **14,** 818–828. ISSN: 1476-4679. https://www.nature.com/articles/ncb2532 (2020) (Aug. 2012).

23. Vassilev, V., Platek, A., Hiver, S., Enomoto, H. & Takeichi, M. Catenins Steer Cell Migration via Stabilization of Front-Rear Polarity. English. *Developmental Cell* **43.** Publisher: Elsevier, 463–479.e5. ISSN: 1534-5807. https://www.cell.com/developmental-cell/abstract/S1534-5807(17)30827-4 (2020) (Nov. 2017).

24. Carramusa, L., Ballestrem, C., Zilberman, Y. & Bershadsky, A. D. Mammalian diaphanous-related formin Dia1 controls the organization of E-cadherin-mediated cell-cell junctions. en. *Journal of Cell Science* **120.** Publisher: The Company of Biologists Ltd Section: Research Article, 3870–3882. ISSN: 0021-9533, 1477-9137. https://jcs.biologists.org/content/120/21/3870 (2020) (Nov. 2007).

25. Michael, M. *et al.* Coronin 1B Reorganizes the Architecture of F-Actin Networks for Contractility at Steady-State and Apoptotic Adherens Junctions. en. *Developmental Cell* **37,** 58–71. ISSN: 15345807. https://linkinghub.elsevier.com/retrieve/pii/S1534580716301162 (2020) (Apr. 2016).

26. Priya, R. *et al.* Bistable front dynamics in a contractile medium: Travelling wave fronts and cortical advection define stable zones of RhoA signaling at epithelial adherens junctions. en. *PLOS Computational Biology* **13,** e1005411. ISSN: 1553-7358. https://journals.plos.org/ploscompbiol/article?id=10.1371/journal.pcbi.1005411 (2020) (Mar. 2017).

27. Priya, R. *et al.* Feedback regulation through myosin II confers robustness on RhoA signalling at E-cadherin junctions. en. *Nature Cell Biology* **17,** 1282–1293. ISSN: 1476-4679. https://www.nature.com/articles/ncb3239 (2020) (Oct. 2015).

28. Priya, R., Yap, A. S. & Gomez, G. A. E-cadherin supports steady-state Rho signaling at the epithelial zonula adherens. en. *Differentiation. Mechanotransduction* **86,** 133–140. ISSN: 0301-4681. http://www.sciencedirect.com/science/article/pii/S0301468113000030 (2020) (Oct. 2013).

29. Bement, W. M., Miller, A. L. & Dassow, G. v. Rho GTPase activity zones and transient contractile arrays. en. *BioEssays* **28,** 983–993. ISSN: 1521-1878. https://onlinelibrary.wiley.com/doi/abs/10.1002/bies.20477 (2020) (2006).

30. Wildenberg, G. A. *et al.* p120-Catenin and p190RhoGAP Regulate Cell-Cell Adhesion by Coordinating Antagonism between Rac and Rho. English. *Cell* **127,** 1027–1039. ISSN: 0092-8674, 1097-4172. https://www.cell.com/cell/abstract/S0092-8674(06)01407-3 (2020) (Dec. 2006).

31. Wang, D., Chadha, G. K., Feygin, A. & Ivanov, A. I. F-actin binding protein, anillin, regulates integrity of intercellular junctions in human epithelial cells. en. *Cell. Mol. Life Sci.* **72,** 3185–3200. ISSN: 1420-9071. https://doi.org/10.1007/s00018-015-1890-6 (2020) (Aug. 2015).

32. Reyes, C. C. *et al.* Anillin Regulates Cell-Cell Junction Integrity by Organizing Junctional Accumulation of Rho-GTP and Actomyosin. English. *Current Biology* **24,** 1263–1270. ISSN: 0960-9822. https://www.cell.com/current-biology/abstract/S0960-9822(14)00459-X (2020) (June 2014).

33. Budnar, S. *et al.* Anillin Promotes Cell Contractility by Cyclic Resetting of RhoA Residence Kinetics. English. *Developmental Cell* **49,** 894–906.e12. ISSN: 1534-5807. https://www.cell.com/developmental-cell/abstract/S1534-5807(19)30328-4 (2020) (June 2019).

34. Terry, S. J. *et al.* Spatially restricted activation of RhoA signalling at epithelial junctions by p114RhoGEF drives junction formation and morphogenesis. en. *Nature Cell Biology*

13, 159–166. ISSN: 1476-4679. https://www.nature.com/articles/ncb2156 (2020) (Feb. 2011).

35. García-Mata, R. & Burridge, K. Catching a GEF by its tail. English. *Trends in Cell Biology* **17,** 36–43. ISSN: 0962-8924, 1879-3088. https://www.cell.com/trends/cell-biology/abstract/S0962-8924(06)00326-6 (2020) (Jan. 2007).

36. Shindo, A. Models of convergent extension during morphogenesis. en. *WIREs Developmental Biology* **7.** _eprint: https://onlinelibrary.wiley.com/doi/pdf/10.1002/wdev.293, e293. ISSN: 1759-7692. https://onlinelibrary.wiley.com/doi/abs/10.1002/wdev.293 (2020) (2018).

37. Carreira-Barbosa, F. *et al.* Flamingo regulates epiboly and convergence/extension movements through cell cohesive and signalling functions during zebrafish gastrulation. en. *Development* **136.** Publisher: The Company of Biologists Ltd Section: Research Article, 383–392. ISSN: 0950-1991, 1477-9129. https://dev.biologists.org/content/136/3/383 (2020) (Feb. 2009).

38. Shook, D. R., Kasprowicz, E. M., Davidson, L. A. & Keller, R. Large, long range tensile forces drive convergence during Xenopus blastopore closure and body axis elongation. *eLife* **7** (ed McDevitt, T. C.) Publisher: eLife Sciences Publications, Ltd, e26944. ISSN: 2050-084X. https://doi.org/10.7554/eLife.26944 (2020) (Mar. 2018).

39. Williams, M., Yen, W., Lu, X. & Sutherland, A. Distinct Apical and Basolateral Mechanisms Drive Planar Cell Polarity-Dependent Convergent Extension of the Mouse Neural Plate. en. *Developmental Cell* **29,** 34–46. ISSN: 15345807. https://linkinghub.elsevier.com/retrieve/pii/S1534580714001002 (2020) (Apr. 2014).

40. Nikolopoulou, E., Galea, G. L., Rolo, A., Greene, N. D. E. & Copp, A. J. Neural tube closure: cellular, molecular and biomechanical mechanisms. en. *Development* **144,** 552–566. ISSN: 0950-1991, 1477-9129. http://dev.biologists.org/lookup/doi/10.1242/dev.145904 (2020) (Feb. 2017).

41. Lienkamp, S. S. *et al.* Vertebrate kidney tubules elongate using a planar cell polarity–dependent, rosette-based mechanism of convergent extension. en. *Nature Genetics* **44.** Number: 12 Publisher: Nature Publishing Group, 1382–1387. ISSN: 1546-1718. https://www.nature.com/articles/ng.2452 (2020) (Dec. 2012).

42. Chacon-Heszele, M. F., Ren, D., Reynolds, A. B., Chi, F. & Chen, P. Regulation of cochlear convergent extension by the vertebrate planar cell polarity pathway is dependent on p120-catenin. en. *Development* **139.** Publisher: Oxford University Press for The Company of Biologists Limited Section: Research Article, 968–978. ISSN: 0950-1991, 1477-9129. https://dev.biologists.org/content/139/5/968 (2020) (Mar. 2012).

43. Zallen, J. A. & Wieschaus, E. Patterned Gene Expression Directs Bipolar Planar Polarity in Drosophila. en. *Developmental Cell* **6,** 343–355. ISSN: 15345807. https://linkinghub.elsevier.com/retrieve/pii/S1534580704000607 (2020) (Mar. 2004).

44. Tetley, R. J., Blanchard, G. B., Fletcher, A. G., Adams, R. J. & Sanson, B. Unipolar distributions of junctional Myosin II identify cell stripe boundaries that drive cell intercalation throughout Drosophila axis extension. *eLife* **5** (ed Paluch, E.) Publisher: eLife Sciences Publications, Ltd, e12094. ISSN: 2050-084X. https://doi.org/10.7554/eLife.12094 (2020) (May 2016).

45. Monier, B., Pélissier-Monier, A., Brand, A. H. & Sanson, B. An actomyosin-based barrier inhibits cell mixing at compartmental boundaries in Drosophila embryos. en. *Nature Cell Biology* **12.** Number: 1 Publisher: Nature Publishing Group, 60–65. ISSN: 1476-4679. https://www.nature.com/articles/ncb2005 (2020) (Jan. 2010).

46. Bertet, C., Sulak, L. & Lecuit, T. Myosin-dependent junction remodelling controls planar cell intercalation and axis elongation. eng. *Nature* **429,** 667–671. ISSN: 1476-4687 (June 2004).

47. Irvine, K. D. & Wieschaus, E. Cell intercalation during Drosophila germband extension and its regulation by pair-rule segmentation genes. en. *Development* **120.** Publisher: The Company of Biologists Ltd Section: JOURNAL ARTICLES, 827–841. ISSN: 0950-1991, 1477-9129. https://dev.biologists.org/content/120/4/827 (2020) (Apr. 1994).

48. Blankenship, J. T., Backovic, S. T., Sanny, J. S. P., Weitz, O. & Zallen, J. A. Multicellular Rosette Formation Links Planar Cell Polarity to Tissue Morphogenesis. English. *Developmental Cell* **11.** Publisher: Elsevier, 459–470. ISSN: 1534-5807. https://www.cell.com/developmental-cell/abstract/S1534-5807(06)00400-X (2020) (Oct. 2006).

49. Zallen, J. A. & Blankenship, J. T. Multicellular dynamics during epithelial elongation. en. *Seminars in Cell & Developmental Biology* **19,** 263–270. ISSN: 10849521. https://linkinghub.elsevier.com/retrieve/pii/S1084952108000074 (2020) (June 2008).

50. Johnston, D. S. & Nüsslein-Volhard, C. The origin of pattern and polarity in the Drosophila embryo. English. *Cell* **68.** Publisher: Elsevier, 201–219. ISSN: 0092-8674, 1097-4172. https://www.cell.com/cell/abstract/0092-8674(92)90466-P (2020) (Jan. 1992).

51. Paré, A. C. *et al.* A positional Toll receptor code directs convergent extension in Drosophila. en. *Nature* **515.** Number: 7528 Publisher: Nature Publishing Group, 523–527. ISSN: 1476-4687. https://www.nature.com/articles/nature13953 (2020) (Nov. 2014).

52. Chin Chiang & Beachy, P. A. Expression of a novel Toll-like gene spans the parasegment boundary and contributes to hedgehog function in the adult eye of Drosophila. en. *Mechanisms of Development* **47,** 225–239. ISSN: 0925-4773. http://www.sciencedirect.com/science/article/pii/0925477394900418 (2020) (Sept. 1994).

53. Kambris, Z., Hoffmann, J. A., Imler, J.-L. & Capovilla, M. Tissue and stage-specific expression of the Tolls in Drosophila embryos. en. *Gene Expression Patterns* **2,** 311–317. ISSN: 1567-133X. http://www.sciencedirect.com/science/article/pii/S1567133X02000200 (2020) (Dec. 2002).

54. Lavalou, J. *et al. Formation of mechanical interfaces by self-organized Toll-8/Cirl GPCR asymmetry* en. preprint (Developmental Biology, Mar. 2020). http://biorxiv.org/lookup/doi/10.1101/2020.03.16.993758 (2020).

55. Benton, M. A. *et al.* Toll Genes Have an Ancestral Role in Axis Elongation. English. *Current Biology* **26.** Publisher: Elsevier, 1609–1615. ISSN: 0960-9822. https://www.cell.com/current-biology/abstract/S0960-9822(16)30409-2 (2020) (June 2016).

56. Paré, A. C. *et al.* An LRR Receptor-Teneurin System Directs Planar Polarity at Compartment Boundaries. en. *Developmental Cell* **51,** 208–221.e6. ISSN: 15345807. https://linkinghub.elsevier.com/retrieve/pii/S153458071930663X (2020) (Oct. 2019).

57. Kerridge, S. *et al.* Modular activation of Rho1 by GPCR signalling imparts polarized myosin II activation during morphogenesis. en. *Nature Cell Biology* **18,** 261–270. ISSN: 1465-7392, 1476-4679. http://www.nature.com/articles/ncb3302 (2019) (Mar. 2016).

58. Garcia De Las Bayonas, A., Philippe, J.-M., Lellouch, A. C. & Lecuit, T. Distinct RhoGEFs Activate Apical and Junctional Contractility under Control of G Proteins during Epithelial Morphogenesis. en. *Current Biology* **29,** 3370–3385.e7. ISSN: 09609822. https://linkinghub.elsevier.com/retrieve/pii/S0960982219310334 (2020) (Oct. 2019).

59. Munjal, A., Philippe, J.-M., Munro, E. & Lecuit, T. A self-organized biomechanical network drives shape changes during tissue morphogenesis. en. *Nature* **524,** 351–355.

ISSN: 0028-0836, 1476-4687. http://www.nature.com/articles/nature14603 (2019) (Aug. 2015).

60. Simões, S. d. M., Mainieri, A. & Zallen, J. A. Rho GTPase and Shroom direct planar polarized actomyosin contractility during convergent extension. en. *The Journal of Cell Biology* **204,** 575–589. ISSN: 0021-9525, 1540-8140. http://www.jcb.org/lookup/doi/10.1083/jcb.201307070 (2019) (Feb. 2014).

61. Siang, L. C., Fernandez-Gonzalez, R. & Feng, J. J. Modeling cell intercalation during Drosophila germband extension. en. *Phys. Biol.* **15,** 066008. ISSN: 1478-3975. https://doi.org/10.1088%2F1478-3975%2Faad865 (2020) (Sept. 2018).

62. Yu, J. C. & Fernandez-Gonzalez, R. Local mechanical forces promote polarized junctional assembly and axis elongation in Drosophila. *eLife* **5** (ed Wallingford, J. B.) Publisher: eLife Sciences Publications, Ltd, e10757. ISSN: 2050-084X. https://doi.org/10.7554/eLife.10757 (2020) (Jan. 2016).

63. Collinet, C., Rauzi, M., Lenne, P.-F. & Lecuit, T. Local and tissue-scale forces drive oriented junction growth during tissue extension. en. *Nature Cell Biology* **17,** 1247–1258. ISSN: 1465-7392, 1476-4679. http://www.nature.com/articles/ncb3226 (2019) (Oct. 2015).

64. Rauzi, M., Lenne, P.-F. & Lecuit, T. Planar polarized actomyosin contractile flows control epithelial junction remodelling. en. *Nature* **468,** 1110–1114. ISSN: 0028-0836, 1476-4687. http://www.nature.com/articles/nature09566 (2019) (Dec. 2010).

65. Fernandez-Gonzalez, R. & Zallen, J. A. Oscillatory behaviors and hierarchical assembly of contractile structures in intercalating cells. en. *Physical Biology* **8,** 045005. ISSN: 1478-3975. http://stacks.iop.org/1478-3975/8/i=4/a=045005?key=crossref.5d1d4c182134675374c151cf5f724adf (2019) (Aug. 2011).

66. Jewett, C. E. *et al.* Planar polarized Rab35 functions as an oscillatory ratchet during cell intercalation in the Drosophila epithelium. eng. *Nat Commun* **8,** 476. ISSN: 2041-1723 (2017).

67. Fernandez-Gonzalez, R., Simoes, S. d. M., Röper, J.-C., Eaton, S. & Zallen, J. A. Myosin II Dynamics Are Regulated by Tension in Intercalating Cells. en. *Developmental Cell* **17,** 736–743. ISSN: 15345807. https://linkinghub.elsevier.com/retrieve/pii/S1534580709003852 (2019) (Nov. 2009).

68. Vasquez, C. G., Tworoger, M. & Martin, A. C. Dynamic myosin phosphorylation regulates contractile pulses and tissue integrity during epithelial morphogenesis. en. *Journal of Cell Biology* **206,** 435–450. ISSN: 1540-8140, 0021-9525. https://rupress.org/jcb/article/206/3/435/37782/Dynamic-myosin-phosphorylation-regulates (2020) (Aug. 2014).

69. Kasza, K. E., Farrell, D. L. & Zallen, J. A. Spatiotemporal control of epithelial remodeling by regulated myosin phosphorylation. en. *Proceedings of the National Academy of Sciences* **111,** 11732–11737. ISSN: 0027-8424, 1091-6490. http://www.pnas.org/cgi/doi/10.1073/pnas.1400520111 (2019) (Aug. 2014).

70. Curran, S. *et al.* Myosin II Controls Junction Fluctuations to Guide Epithelial Tissue Ordering. English. *Developmental Cell* **43,** 480–492.e6. ISSN: 1534-5807. https://www.cell.com/developmental-cell/abstract/S1534-5807(17)30771-2 (2020) (Nov. 2017).

71. Sawyer, J. K. *et al.* A contractile actomyosin network linked to adherens junctions by Canoe/afadin helps drive convergent extension. *MBoC* **22,** 2491–2508. ISSN: 1059-1524. https://www.molbiolcell.org/doi/full/10.1091/mbc.e11-05-0411 (2020) (May 2011).

72. Levayer, R. & Lecuit, T. Oscillation and Polarity of E-Cadherin Asymmetries Control Actomyosin Flow Patterns during Morphogenesis. en. *Developmental Cell* **26,**

162–175. ISSN: 15345807. https://linkinghub.elsevier.com/retrieve/pii/S1534580713003833 (2020) (July 2013).

73. Tamada, M., Farrell, D. L. & Zallen, J. A. Abl Regulates Planar Polarized Junctional Dynamics through β-Catenin Tyrosine Phosphorylation. en. *Developmental Cell* **22,** 309–319. ISSN: 1534-5807. http://www.sciencedirect.com/science/article/pii/S1534580712000068 (2020) (Feb. 2012).

74. Simões, S. d. M. *et al.* Rho-Kinase Directs Bazooka/Par-3 Planar Polarity during Drosophila Axis Elongation. en. *Developmental Cell* **19,** 377–388. ISSN: 15345807. https://linkinghub.elsevier.com/retrieve/pii/S1534580710003862 (2020) (Sept. 2010).

75. Levayer, R., Pelissier-Monier, A. & Lecuit, T. Spatial regulation of Dia and Myosin-II by RhoGEF2 controls initiation of E-cadherin endocytosis during epithelial morphogenesis. en. *Nature Cell Biology* **13,** 529–540. ISSN: 1476-4679. https://www.nature.com/articles/ncb2224 (2019) (May 2011).

76. Roh-Johnson, M. *et al.* Triggering a Cell Shape Change by Exploiting Preexisting Actomyosin Contractions. en. *Science* **335.** Publisher: American Association for the Advancement of Science Section: Report, 1232–1235. ISSN: 0036-8075, 1095-9203. https://science.sciencemag.org/content/335/6073/1232 (2020) (Mar. 2012).

77. Choi, W. *et al.* Remodeling the zonula adherens in response to tension and the role of afadin in this response. en. *The Journal of Cell Biology* **213,** 243–260. ISSN: 0021-9525, 1540-8140. http://www.jcb.org/lookup/doi/10.1083/jcb.201506115 (2019) (Apr. 2016).

78. Vanderleest, T. E. *et al.* Vertex sliding drives intercalation by radial coupling of adhesion and actomyosin networks during Drosophila germband extension. *eLife* **7.** ISSN: 2050-084X. https://www.ncbi.nlm.nih.gov/pmc/articles/PMC6037471/ (2020).

79. Xie, Y., Miao, H. & Blankenship, J. T. Membrane trafficking in morphogenesis and planar polarity. en. *Traffic* **19,** 679–689. ISSN: 1600-0854. https://onlinelibrary.wiley.com/doi/abs/10.1111/tra.12580 (2019) (2018).

80. Levskaya, A., Weiner, O. D., Lim, W. A. & Voigt, C. A. Spatiotemporal control of cell signalling using a light-switchable protein interaction. en. *Nature* **461,** 997–1001. ISSN: 0028-0836, 1476-4687. http://www.nature.com/articles/nature08446 (2019) (Oct. 2009).

81. Li, G. & Marlin, M. C. en. in *Rab GTPases: Methods and Protocols* (ed Li, G.) 1–15 (Springer, New York, NY, 2015). ISBN: 978-1-4939-2569-8. https://doi.org/10.1007/978-1-4939-2569-8_1 (2020).

82. Kale, G. R. *et al.* Distinct contributions of tensile and shear stress on E-cadherin levels during morphogenesis. en. *Nature Communications* **9.** ISSN: 2041-1723. http://www.nature.com/articles/s41467-018-07448-8 (2019) (Dec. 2018).

83. Iyer, K. V., Piscitello-Gómez, R., Paijmans, J., Jülicher, F. & Eaton, S. Epithelial Viscoelasticity Is Regulated by Mechanosensitive E-cadherin Turnover. English. *Current Biology* **29,** 578–591.e5. ISSN: 0960-9822. https://www.cell.com/current-biology/abstract/S0960-9822(19)30023-5 (2020) (Feb. 2019).

84. De Beco, S., Gueudry, C., Amblard, F. & Coscoy, S. Endocytosis is required for E-cadherin redistribution at mature adherens junctions. en. *Proceedings of the National Academy of Sciences* **106,** 7010–7015. ISSN: 0027-8424, 1091-6490. http://www.pnas.org/cgi/doi/10.1073/pnas.0811253106 (2019) (Apr. 2009).

85. Beco, S. d., Perney, J.-B., Coscoy, S. & Amblard, F. Mechanosensitive Adaptation of E-Cadherin Turnover across adherens Junctions. en. *PLOS ONE* **10.** Publisher: Public Library of Science, e0128281. ISSN: 1932-6203. https://journals.plos.org/plosone/article?id=10.1371/journal.pone.0128281 (2020) (June 2015).

86. Sumi, A. *et al.* Adherens Junction Length during Tissue Contraction Is Controlled by the Mechanosensitive Activity of Actomyosin and Junctional Recycling. *Dev Cell* **47,** 453–463.e3. ISSN: 1534-5807. https://www.ncbi.nlm.nih.gov/pmc/articles/PMC6291457/ (2019) (Nov. 2018).

87. Marder, M. Soap-bubble growth. *Phys. Rev. A* **36,** 438–440. https://link.aps.org/doi/10.1103/PhysRevA.36.438 (2020) (July 1987).

88. Okuzono, T. & Kawasaki, K. Intermittent flow behavior of random foams: A computer experiment on foam rheology. *Phys. Rev. E* **51,** 1246–1253. https://link.aps.org/doi/10.1103/PhysRevE.51.1246 (2020) (Feb. 1995).

89. Chickarmane, V. *et al.* Computational Morphodynamics: A Modeling Framework to Understand Plant Growth. *Annual Review of Plant Biology* **61,** 65–87. https://doi.org/10.1146/annurev-arplant-042809-112213 (2020) (2010).

90. Farhadifar, R., Röper, J.-C., Aigouy, B., Eaton, S. & Jülicher, F. The Influence of Cell Mechanics, Cell-Cell Interactions, and Proliferation on Epithelial Packing. en. *Current Biology* **17,** 2095–2104. ISSN: 0960-9822. http://www.sciencedirect.com/science/article/pii/S0960982207023342 (2020) (Dec. 2007).

91. Okuda, S., Miura, T., Inoue, Y., Adachi, T. & Eiraku, M. Combining Turing and 3D vertex models reproduces autonomous multicellular morphogenesis with undulation, tubulation, and branching. en. *Scientific Reports* **8.** Number: 1 Publisher: Nature Publishing Group, 1–15. ISSN: 2045-2322. https://www.nature.com/articles/s41598-018-20678-6 (2020) (Feb. 2018).

92. Sahlin, P. & Jönsson, H. A Modeling Study on How Cell Division Affects Properties of Epithelial Tissues Under Isotropic Growth. en. *PLOS ONE* **5.** Publisher: Public Library of Science, e11750. ISSN: 1932-6203. https://journals.plos.org/plosone/article?id=10.1371/journal.pone.0011750 (2020) (July 2010).

93. Staple, D. B. *et al.* Mechanics and remodelling of cell packings in epithelia. en. *Eur. Phys. J. E* **33,** 117–127. ISSN: 1292-8941, 1292-895X. http://link.springer.com/10.1140/epje/i2010-10677-0 (2020) (Oct. 2010).

94. Staddon, M. F., Cavanaugh, K. E., Munro, E. M., Gardel, M. L. & Banerjee, S. Mechanosensitive Junction Remodeling Promotes Robust Epithelial Morphogenesis. English. *Biophysical Journal* **117,** 1739–1750. ISSN: 0006-3495. https://www.cell.com/biophysj/abstract/S0006-3495(19)30814-8 (2020) (Nov. 2019).

95. Tlili, S. *et al.* Shaping the zebrafish myotome by intertissue friction and active stress. en. *PNAS* **116.** Publisher: National Academy of Sciences Section: PNAS Plus, 25430–25439. ISSN: 0027-8424, 1091-6490. https://www.pnas.org/content/116/51/25430 (2020) (Dec. 2019).

96. Alt, S., Ganguly, P. & Salbreux, G. Vertex models: from cell mechanics to tissue morphogenesis. en. *Phil. Trans. R. Soc. B* **372,** 20150520. ISSN: 0962-8436, 1471-2970. https://royalsocietypublishing.org/doi/10.1098/rstb.2015.0520 (2020) (May 2017).

97. Loerke, D. & Blankenship, J. T. Viscoelastic voyages – Biophysical perspectives on cell intercalation during Drosophila gastrulation. en. *Seminars in Cell & Developmental Biology. REGENERATION OF VERTEBRATE ORGANS* **100,** 212–222. ISSN: 1084-9521. http://www.sciencedirect.com/science/article/pii/S1084952119300333 (2020) (Apr. 2020).

98. Bi, D., Lopez, J. H., Schwarz, J. M. & Manning, M. L. A density-independent rigidity transition in biological tissues. en. *Nature Physics* **11,** 1074–1079. ISSN: 1745-2473, 1745-2481. http://www.nature.com/articles/nphys3471 (2019) (Dec. 2015).

99. Merkel, M. & Manning, M. L. A geometrically controlled rigidity transition in a model for confluent 3D tissues. en. *New J. Phys.* **20,** 022002. ISSN: 1367-2630. https://doi.org/10.1088%2F1367-2630%2Faaaa13 (2020) (Feb. 2018).

100. Barriga, E. H. & Mayor, R. Adjustable viscoelasticity allows for efficient collective cell migration. en. *Seminars in Cell & Developmental Biology. SI: Viscoelasticity* **93,** 55–68. ISSN: 1084-9521. http://www.sciencedirect.com/science/article/pii/S1084952117305505 (2020) (Sept. 2019).

101. Petridou, N. I. & Heisenberg, C.-P. Tissue rheology in embryonic organization. en. *The EMBO Journal* **38.** ISSN: 1460-2075. https://www.embopress.org/doi/abs/10.15252/embj.2019102497 (2020) (Oct. 2019).

102. Clément, R., Dehapiot, B., Collinet, C., Lecuit, T. & Lenne, P.-F. Viscoelastic Dissipation Stabilizes Cell Shape Changes during Tissue Morphogenesis. en. *Current Biology* **27,** 3132–3142.e4. ISSN: 09609822. https://linkinghub.elsevier.com/retrieve/pii/S0960982217311697 (2019) (Oct. 2017).

103. Ferro, V., Chuai, M., McGloin, D. & Weijer, C. J. Measurement of junctional tension in epithelial cells at the onset of primitive streak formation in the chick embryo via non-destructive optical manipulation. en. *Development* **147.** ISSN: 0950-1991, 1477-9129. https://dev.biologists.org/content/147/3/dev175109 (2020) (Feb. 2020).

104. Bambardekar, K., Clément, R., Blanc, O., Chardès, C. & Lenne, P.-F. Direct laser manipulation reveals the mechanics of cell contacts in vivo. en. *PNAS* **112,** 1416–1421. ISSN: 0027-8424, 1091-6490. https://www.pnas.org/content/112/5/1416 (2020) (Feb. 2015).

105. Khalilgharibi, N. *et al.* Stress relaxation in epithelial monolayers is controlled by the actomyosin cortex. en. *Nature Physics* **15,** 839–847. ISSN: 1745-2473, 1745-2481. http://www.nature.com/articles/s41567-019-0516-6 (2019) (Aug. 2019).

106. Noll, N., Mani, M., Heemskerk, I., Streichan, S. J. & Shraiman, B. I. Active tension network model suggests an exotic mechanical state realized in epithelial tissues. en. *Nature Physics* **13,** 1221–1226. ISSN: 1745-2473, 1745-2481. http://www.nature.com/articles/nphys4219 (2019) (Dec. 2017).

107. Duda, M. *et al.* Polarization of Myosin II Refines Tissue Material Properties to Buffer Mechanical Stress. English. *Developmental Cell* **48,** 245–260.e7. ISSN: 1534-5807. https://www.cell.com/developmental-cell/abstract/S1534-5807(18)31088-8 (2020) (Jan. 2019).

108. Strickland, D. *et al.* TULIPs: tunable, light-controlled interacting protein tags for cell biology. en. *Nature Methods* **9,** 379–384. ISSN: 1548-7091, 1548-7105. http://www.nature.com/articles/nmeth.1904 (2019) (Apr. 2012).

109. Lessey, E. C., Guilluy, C. & Burridge, K. From Mechanical Force to RhoA Activation. en. *Biochemistry* **51,** 7420–7432. ISSN: 0006-2960, 1520-4995. http://pubs.acs.org/doi/10.1021/bi300758e (2019) (Sept. 2012).

110. Wagner, E. & Glotzer, M. Local RhoA activation induces cytokinetic furrows independent of spindle position and cell cycle stage. en. *The Journal of Cell Biology* **213,** 641–649. ISSN: 0021-9525, 1540-8140. http://www.jcb.org/lookup/doi/10.1083/jcb.201603025 (2019) (June 2016).

111. Meshik, X., O'Neill, P. R. & Gautam, N. Physical Plasma Membrane Perturbation Using Subcellular Optogenetics Drives Integrin-Activated Cell Migration. en. *ACS Synthetic Biology* **8,** 498–510. ISSN: 2161-5063, 2161-5063. http://pubs.acs.org/doi/10.1021/acssynbio.8b00356 (2019) (Mar. 2019).

112. O'Neill, P. R. *et al.* Membrane flow drives an adhesion-independent amoeboid cell migration mode. *Dev Cell* **46,** 9–22.e4. ISSN: 1534-5807. https://www.ncbi.nlm.nih.gov/pmc/articles/PMC6048972/ (2019) (July 2018).

113. Oakes, P. W. *et al.* Optogenetic control of RhoA reveals zyxin-mediated elasticity of stress fibres. en. *Nature Communications* **8,** 15817. ISSN: 2041-1723. http://www.nature.com/doifinder/10.1038/ncomms15817 (2019) (June 2017).

114. Cavanaugh, K. E., Staddon, M. F., Munro, E., Banerjee, S. & Gardel, M. L. RhoA Mediates Epithelial Cell Shape Changes via Mechanosensitive Endocytosis. English.

Developmental Cell **52,** 152–166.e5. ISSN: 1534-5807. https://www.cell.com/developmental-cell/abstract/S1534-5807(19)31023-8 (2020) (Jan. 2020).

115. Valon, L., Marín-Llauradó, A., Wyatt, T., Charras, G. & Trepat, X. Optogenetic control of cellular forces and mechanotransduction. en. *Nature Communications* **8.** ISSN: 2041-1723. http://www.nature.com/articles/ncomms14396 (2019) (Apr. 2017).

116. Izquierdo, E., Quinkler, T. & Renzis, S. D. Guided morphogenesis through optogenetic activation of Rho signalling during early Drosophila embryogenesis. en. *Nat Commun* **9,** 1–13. ISSN: 2041-1723. https://www.nature.com/articles/s41467-018-04754-z (2019) (June 2018).

117. Möglich, A. & Moffat, K. Engineered photoreceptors as novel optogenetic tools. en. *Photochem. Photobiol. Sci.* **9,** 1286–1300. ISSN: 1474-9092. https://pubs.rsc.org/en/content/articlelanding/2010/pp/c0pp00167h (2019) (Sept. 2010).

118. Halavaty, A. S. & Moffat, K. N- and C-Terminal Flanking Regions Modulate Light-Induced Signal Transduction in the LOV2 Domain of the Blue Light Sensor Phototropin 1 from Avena sativa, *Biochemistry* **46,** 14001–14009. ISSN: 0006-2960. https://doi.org/10.1021/bi701543e (2019) (Dec. 2007).

119. Harper, S. M., Neil, L. C. & Gardner, K. H. Structural Basis of a Phototropin Light Switch. en. *Science* **301,** 1541–1544. ISSN: 0036-8075, 1095-9203. https://science.sciencemag.org/content/301/5639/1541 (2019) (Sept. 2003).

120. Huang, J., Koide, A., Makabe, K. & Koide, S. Design of protein function leaps by directed domain interface evolution. en. *PNAS* **105,** 6578–6583. ISSN: 0027-8424, 1091-6490. https://www.pnas.org/content/105/18/6578 (2019) (May 2008).

121. Kennedy, M. J. *et al.* Rapid blue-light–mediated induction of protein interactions in living cells. en. *Nature Methods* **7,** 973–975. ISSN: 1548-7091, 1548-7105. http://www.nature.com/articles/nmeth.1524 (2019) (Dec. 2010).

122. Guntas, G. *et al.* Engineering an improved light-induced dimer (iLID) for controlling the localization and activity of signaling proteins. en. *Proceedings of the National Academy of Sciences* **112,** 112–117. ISSN: 0027-8424, 1091-6490. http://www.pnas.org/lookup/doi/10.1073/pnas.1417910112 (2019) (Jan. 2015).

123. Zimmerman, S. P. *et al.* Tuning the Binding Affinities and Reversion Kinetics of a Light Inducible Dimer Allows Control of Transmembrane Protein Localization. en. *Biochemistry* **55,** 5264–5271. ISSN: 0006-2960, 1520-4995. http://pubs.acs.org/doi/10.1021/acs.biochem.6b00529 (2019) (Sept. 2016).

124. Kawano, F., Suzuki, H., Furuya, A. & Sato, M. Engineered pairs of distinct photoswitches for optogenetic control of cellular proteins. en. *Nature Communications* **6.** ISSN: 2041-1723. http://www.nature.com/articles/ncomms7256 (2019) (May 2015).

125. Yazawa, M., Sadaghiani, A. M., Hsueh, B. & Dolmetsch, R. E. Induction of protein-protein interactions in live cells using light. en. *Nature Biotechnology* **27,** 941–945. ISSN: 1087-0156, 1546-1696. http://www.nature.com/articles/nbt.1569 (2019) (Oct. 2009).

126. Wang, H. & Hahn, K. M. LOVTRAP: A Versatile Method to Control Protein Function with Light. en. *Current Protocols in Cell Biology* **73,** 21.10.1–21.10.14. ISSN: 1934-2616. https://currentprotocols.onlinelibrary.wiley.com/doi/abs/10.1002/cpcb.12 (2019) (2016).

127. Dine, E., Gil, A. A., Uribe, G., Brangwynne, C. P. & Toettcher, J. E. Protein Phase Separation Provides Long-Term Memory of Transient Spatial Stimuli. English. *cels* **6,** 655–663.e5. ISSN: 2405-4712. https://www.cell.com/cell-systems/abstract/S2405-4712(18)30190-X (2019) (June 2018).

128. Kaberniuk, A. A., Shemetov, A. A. & Verkhusha, V. V. A bacterial phytochrome-based optogenetic system controllable with near-infrared light. en. *Nature Methods* **13,** 591–

597. ISSN: 1548-7091, 1548-7105. http://www.nature.com/articles/nmeth.3864 (2019) (July 2016).

129. Crefcoeur, R. P., Yin, R., Ulm, R. & Halazonetis, T. D. Ultraviolet-B-mediated induction of protein–protein interactions in mammalian cells. en. *Nature Communications* **4.** ISSN: 2041-1723. http://www.nature.com/articles/ncomms2800 (2019) (June 2013).

130. Schmidt, A. Guanine nucleotide exchange factors for Rho GTPases: turning on the switch. en. *Genes & Development* **16,** 1587–1609. ISSN: 08909369. http://www.genesdev.org/cgi/doi/10.1101/gad.1003302 (2019) (July 2002).

131. Jaiswal, M. *et al.* Mechanistic Insights into Specificity, Activity, and Regulatory Elements of the Regulator of G-protein Signaling (RGS)-containing Rho-specific Guanine Nucleotide Exchange Factors (GEFs) p115, PDZ-RhoGEF (PRG), and Leukemia-associated RhoGEF (LARG). en. *Journal of Biological Chemistry* **286,** 18202–18212. ISSN: 0021-9258, 1083-351X. http://www.jbc.org/lookup/doi/10.1074/jbc.M111.226431 (2019) (May 2011).

132. Chen, Z. *et al.* Activated RhoA Binds to the Pleckstrin Homology (PH) Domain of PDZ-RhoGEF, a Potential Site for Autoregulation. en. *J. Biol. Chem.* **285,** 21070–21081. ISSN: 0021-9258, 1083-351X. http://www.jbc.org/lookup/doi/10.1074/jbc.M110.122549 (2019) (July 2010).

133. Chen, Z., Guo, L., Sprang, S. R. & Sternweis, P. C. Modulation of a GEF switch: Autoinhibition of the intrinsic guanine nucleotide exchange activity of p115-RhoGEF. en. *Protein Science* **20,** 107–117. ISSN: 1469-896X. https://onlinelibrary.wiley.com/doi/abs/10.1002/pro.542 (2019) (2011).

134. Chen, X., Zaro, J. & Shen, W.-C. Fusion Protein Linkers: Property, Design and Functionality. *Adv Drug Deliv Rev* **65,** 1357–1369. ISSN: 0169-409X. https://www.ncbi.nlm.nih.gov/pmc/articles/PMC3726540/ (2019) (Oct. 2013).

135. Whitlow, M. *et al.* An improved linker for single-chain Fv with reduced aggregation and enhanced proteolytic stability. en. *Protein Eng Des Sel* **6,** 989–995. ISSN: 1741-0126. https://academic.oup.com/peds/article/6/8/989/1559790 (2019) (Nov. 1993).

136. Piekny, A. J. & Glotzer, M. Anillin Is a Scaffold Protein That Links RhoA, Actin, and Myosin during Cytokinesis. English. *Current Biology* **18,** 30–36. ISSN: 0960-9822. https://www.cell.com/current-biology/abstract/S0960-9822(07)02414-1 (2020) (Jan. 2008).

137. Heisenberg, C.-P. & Bellaïche, Y. Forces in Tissue Morphogenesis and Patterning. en. *Cell* **153,** 948–962. ISSN: 00928674. https://linkinghub.elsevier.com/retrieve/pii/S0092867413005734 (2019) (May 2013).

138. Siedlik, M. J. & Nelson, C. M. Regulation of tissue morphodynamics: an important role for actomyosin contractility. *Current Opinion in Genetics & Development. Developmental mechanisms, patterning and organogenesis* **32,** 80–85. ISSN: 0959-437X. http://www.sciencedirect.com/science/article/pii/S0959437X15000039 (2019) (June 2015).

139. Heer, N. C. & Martin, A. C. Tension, contraction and tissue morphogenesis. en. *Development* **144,** 4249–4260. ISSN: 0950-1991, 1477-9129. http://dev.biologists.org/content/144/23/4249 (2019) (Dec. 2017).

140. Martin, A. C., Gelbart, M., Fernandez-Gonzalez, R., Kaschube, M. & Wieschaus, E. F. Integration of contractile forces during tissue invagination. en. *The Journal of Cell Biology* **188,** 735–749. ISSN: 0021-9525, 1540-8140. http://www.jcb.org/lookup/doi/10.1083/jcb.200910099 (2019) (Mar. 2010).

141. Pinheiro, D. & Bellaïche, Y. Mechanical Force-Driven Adherens Junction Remodeling and Epithelial Dynamics. en. *Developmental Cell* **47,** 3–19. ISSN: 15345807. https://linkinghub.elsevier.com/retrieve/pii/S1534580718307433 (2019) (Oct. 2018).

142. Coravos, J. S., Mason, F. M. & Martin, A. C. Actomyosin Pulsing in Tissue Integrity Maintenance during Morphogenesis. *Trends in Cell Biology* **27,** 276–283. ISSN: 0962-8924. http://www.sciencedirect.com/science/article/pii/S0962892416302069 (2019) (Apr. 2017).

143. Martin, A. C., Kaschube, M. & Wieschaus, E. F. Pulsed contractions of an actin–myosin network drive apical constriction. en. *Nature* **457,** 495–499. ISSN: 0028-0836, 1476-4687. http://www.nature.com/doifinder/10.1038/nature07522 (2019) (Jan. 2009).

144. Gorfinkiel, N. & Blanchard, G. B. Dynamics of actomyosin contractile activity during epithelial morphogenesis. en. *Current Opinion in Cell Biology* **23,** 531–539. ISSN: 09550674. https://linkinghub.elsevier.com/retrieve/pii/S0955067411000834 (2019) (Oct. 2011).

145. Solon, J., Kaya-Çopur, A., Colombelli, J. & Brunner, D. Pulsed Forces Timed by a Ratchet-like Mechanism Drive Directed Tissue Movement during Dorsal Closure. English. *Cell* **137,** 1331–1342. ISSN: 0092-8674, 1097-4172. https://www.cell.com/cell/abstract/S0092-8674(09)00394-8 (2019) (June 2009).

146. Blanchard, G. B., Étienne, J. & Gorfinkiel, N. From pulsatile apicomedial contractility to effective epithelial mechanics. en. *Current Opinion in Genetics & Development* **51,** 78–87. ISSN: 0959437X. https://linkinghub.elsevier.com/retrieve/pii/S0959437X18300108 (2019) (Aug. 2018).

147. Maître, J.-L., Niwayama, R., Turlier, H., Nédélec, F. & Hiiragi, T. Pulsatile cell-autonomous contractility drives compaction in the mouse embryo. en. *Nature Cell Biology* **17,** 849–855. ISSN: 1465-7392, 1476-4679. http://www.nature.com/articles/ncb3185 (2019) (July 2015).

148. Mason, F. M., Xie, S., Vasquez, C. G., Tworoger, M. & Martin, A. C. RhoA GTPase inhibition organizes contraction during epithelial morphogenesis. en. *The Journal of*

Cell Biology **214,** 603–617. ISSN: 0021-9525, 1540-8140. http://www.jcb.org/lookup/doi/10.1083/jcb.201603077 (2019) (Aug. 2016).

149. Michaux, J. B., Robin, F. B., McFadden, W. M. & Munro, E. M. Excitable RhoA dynamics drive pulsed contractions in the early *C. elegans* embryo. en. *The Journal of Cell Biology* **217,** 4230–4252. ISSN: 0021-9525, 1540-8140. http://www.jcb.org/lookup/doi/10.1083/jcb.201806161 (2019) (Dec. 2018).

150. Roeth, J. F., Sawyer, J. K., Wilner, D. A. & Peifer, M. Rab11 Helps Maintain Apical Crumbs and Adherens Junctions in the Drosophila Embryonic Ectoderm. en. *PLoS ONE* **4** (ed Bergmann, A.) e7634. ISSN: 1932-6203. https://dx.plos.org/10.1371/journal.pone.0007634 (2019) (Oct. 2009).

151. Muñoz, J. J. & Albo, S. Physiology-based model of cell viscoelasticity. en. *Physical Review E* **88.** ISSN: 1539-3755, 1550-2376. https://link.aps.org/doi/10.1103/PhysRevE.88.012708 (2019) (July 2013).

152. Odell, G. M., Oster, G., Alberch, P. & Burnside, B. The mechanical basis of morphogenesis: I. Epithelial folding and invagination. *Developmental Biology* **85,** 446–462. ISSN: 0012-1606. http://www.sciencedirect.com/science/article/pii/0012160681902761 (2019) (July 1981).

153. Staddon, M. F., Cavanaugh, K. E., Munro, E. M., Gardel, M. L. & Banerjee, S. Mechanosensitive junction remodelling promotes robust epithelial morphogenesis. en. *bioRxiv.* http://biorxiv.org/lookup/doi/10.1101/648980 (2019) (May 2019).

154. Brouxhon, S. M. *et al.* Monoclonal Antibody against the Ectodomain of E-Cadherin (DECMA-1) Suppresses Breast Carcinogenesis: Involvement of the HER/PI3K/Akt/mTOR and IAP Pathways. *Clin Cancer Res* **19,** 3234–3246. ISSN: 1078-0432. https://www.ncbi.nlm.nih.gov/pmc/articles/PMC4014632/ (2019) (June 2013).

155. Macia, E. *et al.* Dynasore, a Cell-Permeable Inhibitor of Dynamin. en. *Developmental Cell* **10,** 839–850. ISSN: 15345807. https://linkinghub.elsevier.com/retrieve/pii/S1534580706001638 (2019) (June 2006).

156. Kim, T., Gardel, M. L. & Munro, E. Determinants of Fluidlike Behavior and Effective Viscosity in Cross-Linked Actin Networks. en. *Biophysical Journal* **106,** 526–534. ISSN: 00063495. https://linkinghub.elsevier.com/retrieve/pii/S0006349513058487 (2019) (Feb. 2014).

157. McFadden, W. M., McCall, P. M., Gardel, M. L. & Munro, E. M. Filament turnover tunes both force generation and dissipation to control long-range flows in a model actomyosin cortex. en. *PLOS Computational Biology* **13,** e1005811. ISSN: 1553-7358. https://journals.plos.org/ploscompbiol/article?id=10.1371/journal.pcbi.1005811 (2019) (Dec. 2017).

158. Wilson, C. A. *et al.* Myosin II contributes to cell-scale actin network treadmilling through network disassembly. en. *Nature* **465,** 373–377. ISSN: 0028-0836, 1476-4687. http://www.nature.com/articles/nature08994 (2019) (May 2010).

159. Mateus, A. M., Gorfinkiel, N., Schamberg, S. & Arias, A. M. Endocytic and Recycling Endosomes Modulate Cell Shape Changes and Tissue Behaviour during Morphogenesis in Drosophila. en. *PLOS ONE* **6,** e18729. ISSN: 1932-6203. https://journals.plos.org/plosone/article?id=10.1371/journal.pone.0018729 (2019) (Apr. 2011).

160. Xie, S. & Martin, A. C. Intracellular signalling and intercellular coupling coordinate heterogeneous contractile events to facilitate tissue folding. en. *Nature Communications* **6.** ISSN: 2041-1723. http://www.nature.com/articles/ncomms8161 (2019) (Nov. 2015).

161. Sun, Z. *et al.* Basolateral protrusion and apical contraction cooperatively drive Drosophila germ-band extension. en. *Nature Cell Biology* **19,** 375–383. ISSN: 1465-7392, 1476-4679. http://www.nature.com/articles/ncb3497 (2019) (Apr. 2017).

162. Brakke, K. A. The Surface Evolver. *Experimental Mathematics* **1,** 141–165. ISSN: 1058-6458. https://doi.org/10.1080/10586458.1992.10504253 (2019) (Jan. 1992).

163. Mason, F. M., Tworoger, M. & Martin, A. C. Apical domain polarization localizes actin–myosin activity to drive ratchet-like apical constriction. en. *Nature Cell Biology* **15,** 926–936. ISSN: 1476-4679. https://www.nature.com/articles/ncb2796 (2020) (Aug. 2013).

164. Lecuit, T. & Yap, A. S. E-cadherin junctions as active mechanical integrators in tissue dynamics. en. *Nature Cell Biology* **17,** 533–539. ISSN: 1465-7392, 1476-4679. http://www.nature.com/articles/ncb3136 (2019) (May 2015).

165. Wu, Y. *et al.* Cooperativity between *trans* and *cis* interactions in cadherin-mediated junction formation. en. *Proc Natl Acad Sci USA* **107,** 17592–17597. ISSN: 0027-8424, 1091-6490. http://www.pnas.org/lookup/doi/10.1073/pnas.1011247107 (2020) (Oct. 2010).

166. Pannekoek, W.-J., de Rooij, J. & Gloerich, M. Force transduction by cadherin adhesions in morphogenesis. en. *F1000Res* **8,** 1044. ISSN: 2046-1402. https://f1000research.com/articles/8-1044/v1 (2020) (July 2019).

167. Buckley, C. D. *et al.* The minimal cadherin-catenin complex binds to actin filaments under force. en. *Science* **346.** Publisher: American Association for the Advancement of Science Section: Research Article. ISSN: 0036-8075, 1095-9203. https://science.sciencemag.org/content/346/6209/1254211 (2020) (Oct. 2014).

168. Hong, S., Troyanovsky, R. B. & Troyanovsky, S. M. Binding to F-actin guides cadherin cluster assembly, stability, and movement. en. *The Journal of Cell Biology* **201,** 131–143. ISSN: 1540-8140, 0021-9525. https://rupress.org/jcb/article/201/1/131/37268/Binding-to-Factin-guides-cadherin-cluster-assembly (2020) (Apr. 2013).

169. Acharya, B. R. *et al.* Mammalian Diaphanous 1 Mediates a Pathway for E-cadherin to Stabilize Epithelial Barriers through Junctional Contractility. en. *Cell Reports* **18,** 2854–2867. ISSN: 22111247. https://linkinghub.elsevier.com/retrieve/pii/S221112471730298X (2020) (Mar. 2017).

170. Cavey, M., Rauzi, M., Lenne, P.-F. & Lecuit, T. A two-tiered mechanism for stabilization and immobilization of E-cadherin. en. *Nature* **453,** 751–756. ISSN: 1476-4687. https://www.nature.com/articles/nature06953 (2020) (June 2008).

171. Huebner, R. J. *et al. Cadherin clustering controls heterogeneous, asymmetric junction dynamics during vertebrate axis elongation* en. preprint (Cell Biology, Feb. 2020). http://biorxiv.org/lookup/doi/10.1101/2020.02.11.944033 (2020).

172. Stoops, S. L. *et al. Identification and Optimization of Small Molecules That Restore E-Cadherin Expression and Reduce Invasion in Colorectal Carcinoma Cells* EN. research-article. Archive Location: world Publisher: American Chemical Society. Feb. 2011. https://pubs.acs.org/doi/pdf/10.1021/cb100305h (2020).

173. Aratyn-Schaus, Y. & Gardel, M. L. Transient Frictional Slip between Integrin and the ECM in Focal Adhesions under Myosin II Tension. en. *Current Biology* **20,** 1145–1153. ISSN: 0960-9822. http://www.sciencedirect.com/science/article/pii/S0960982210006524 (2020) (July 2010).

174. Acharya, B. R. *et al.* A Mechanosensitive RhoA Pathway that Protects Epithelia against Acute Tensile Stress. en. *Developmental Cell* **47,** 439–452.e6. ISSN: 15345807. https://linkinghub.elsevier.com/retrieve/pii/S1534580718307767 (2020) (Nov. 2018).

175. Cavanaugh, K. E., Oakes, P. W. & Gardel, M. L. Optogenetic Control of RhoA to Probe Subcellular Mechanochemical Circuitry. en. *Current Protocols in Cell Biology* **86.** _eprint: https://currentprotocols.onlinelibrary.wiley.com/doi/pdf/10.1002/cpcb.102,

e102. ISSN: 1934-2616. https://currentprotocols.onlinelibrary.wiley.com/doi/abs/10.1002/cpcb.102 (2020) (2020).

176. Razzell, W., Wood, W. & Martin, P. Recapitulation of morphogenetic cell shape changes enables wound re-epithelialisation. en. *Development* **141,** 1814–1820. ISSN: 0950-1991, 1477-9129. https://dev.biologists.org/content/141/9/1814 (2020) (May 2014).

177. Jodoin, J. N. *et al.* Stable Force Balance between Epithelial Cells Arises from F-Actin Turnover. en. *Developmental Cell* **35,** 685–697. ISSN: 15345807. https://linkinghub.elsevier.com/retrieve/pii/S1534580715007534 (2019) (Dec. 2015).

178. Han, M. K. L. *et al.* αE-catenin-dependent mechanotransduction is essential for proper convergent extension in zebrafish. en. *Biology Open* **5.** Publisher: The Company of Biologists Ltd Section: Research Article, 1461–1472. ISSN: 2046-6390. https://bio.biologists.org/content/5/10/1461 (2020) (Oct. 2016).

179. Hotulainen, P. & Lappalainen, P. Stress fibers are generated by two distinct actin assembly mechanisms in motile cells. en. *J Cell Biol* **173.** Publisher: The Rockefeller University Press, 383–394. ISSN: 0021-9525. https://rupress.org/jcb/article/173/3/383/34265/Stress-fibers-are-generated-by-two-distinct-actin (2020) (May 2006).

180. Mayor, S., Parton, R. G. & Donaldson, J. G. Clathrin-Independent Pathways of Endocytosis. en. *Cold Spring Harbor Perspectives in Biology* **6,** a016758–a016758. ISSN: 1943-0264. http://cshperspectives.cshlp.org/lookup/doi/10.1101/cshperspect.a016758 (2019) (June 2014).

181. Ramachandran, R. Vesicle scission: Dynamin. en. *Seminars in Cell & Developmental Biology. GTPases in Intracellular Trafficking* **22,** 10–17. ISSN: 1084-9521. http://www.sciencedirect.com/science/article/pii/S1084952110001485 (2020) (Feb. 2011).

182. Cadwell, C. M., Su, W. & Kowalczyk, A. P. Cadherin tales: Regulation of cadherin function by endocytic membrane trafficking. en. *Traffic* **17,** 1262–1271. ISSN: 1600-0854. https://onlinelibrary.wiley.com/doi/abs/10.1111/tra.12448 (2020) (2016).

183. Krainer, E. C. *et al.* The multiplicity of human formins: Expression patterns in cells and tissues. en. *Cytoskeleton* **70,** 424–438. ISSN: 1949-3592. https://onlinelibrary.wiley.com/doi/abs/10.1002/cm.21113 (2020) (2013).

184. McCall, P. M., MacKintosh, F. C., Kovar, D. R. & Gardel, M. L. Cofilin drives rapid turnover and fluidization of entangled F-actin. en. *PNAS* **116.** Publisher: National Academy of Sciences Section: PNAS Plus, 12629–12637. ISSN: 0027-8424, 1091-6490. https://www.pnas.org/content/116/26/12629 (2020) (June 2019).

185. Ikawa, K. & Sugimura, K. AIP1 and cofilin ensure a resistance to tissue tension and promote directional cell rearrangement. en. *Nature Communications* **9.** Number: 1 Publisher: Nature Publishing Group, 1–14. ISSN: 2041-1723. https://www.nature.com/articles/s41467-018-05605-7 (2020) (Sept. 2018).

186. Malinova, T. S. & Huveneers, S. Sensing of Cytoskeletal Forces by Asymmetric Adherens Junctions. English. *Trends in Cell Biology* **28.** Publisher: Elsevier, 328–341. ISSN: 0962-8924, 1879-3088. https://www.cell.com/trends/cell-biology/abstract/S0962-8924(17)30206-4 (2020) (Apr. 2018).

187. Angulo-Urarte, A., van der Wal, T. & Huveneers, S. Cell-cell junctions as sensors and transducers of mechanical forces. en. *Biochimica et Biophysica Acta (BBA) - Biomembranes,* 183316. ISSN: 0005-2736. http://www.sciencedirect.com/science/article/pii/S0005273620301474 (2020) (Apr. 2020).

188. De Kreuk, B.-J. & Hordijk, P. L. Control of Rho GTPase function by BAR-domains. en. *Small GTPases* **3,** 45–52. ISSN: 2154-1248, 2154-1256. http://www.tandfonline.com/doi/abs/10.4161/sgtp.18960 (2020) (Jan. 2012).

189. Qualmann, B., Koch, D. & Kessels, M. M. Let's go bananas: revisiting the endocytic BAR code. *The EMBO Journal* **30.** Publisher: John Wiley & Sons, Ltd, 3501–3515. ISSN: 0261-4189. https://www.embopress.org/doi/10.1038/emboj.2011.266 (2020) (Aug. 2011).

190. Aspenström, P. BAR domain proteins regulate Rho GTPase signaling. *Small GTPases* **5.** Publisher: Taylor & Francis _eprint: https://doi.org/10.4161/sgtp.28580, e972854. ISSN: 2154-1248. https://doi.org/10.4161/sgtp.28580 (2020) (Apr. 2014).

191. Crawford, A. W. & Beckerle, M. C. Purification and characterization of zyxin, an 82,000-dalton component of adherens junctions. en. *J. Biol. Chem.* **266.** Publisher: American Society for Biochemistry and Molecular Biology, 5847–5853. ISSN: 0021-9258, 1083-351X. http://www.jbc.org/content/266/9/5847 (2020) (Mar. 1991).

192. Nguyen, T. N., Uemura, A., Shih, W. & Yamada, S. Zyxin-mediated Actin Assembly Is Required for Efficient Wound Closure. en. *J. Biol. Chem.* **285,** 35439–35445. ISSN: 0021-9258, 1083-351X. http://www.jbc.org/lookup/doi/10.1074/jbc.M110.119487 (2020) (Nov. 2010).

193. Higashi, T. & Miller, A. L. Tricellular junctions: how to build junctions at the TRICkiest points of epithelial cells. en. *MBoC* **28** (ed Bement, W.) 2023–2034. ISSN: 1059-1524, 1939-4586. https://www.molbiolcell.org/doi/10.1091/mbc.e16-10-0697 (2020) (July 2017).